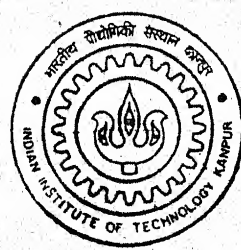


AN EXPERIMENTAL STUDY OF CONVECTIVE HEAT TRANSFER FROM FLAT AND RIBBED SURFACES

by

Sangram Kishore Swain

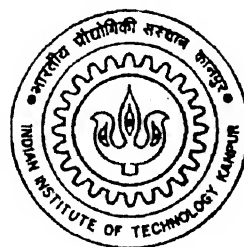
**TH
ME/2001/M
Sw14C**



**DEPARTMENT OF MECHANICAL ENGINEERING
Indian Institute of Technology, Kanpur
April, 2001**

AN EXPERIMENTAL STUDY OF CONVECTIVE HEAT TRANSFER FROM FLAT AND RIBBED SURFACES

by
Sangram Kishore Swain



**DEPARTMENT OF MECHANICAL ENGINEERING
INDIAN INSTITUTE OF TECHNOLOGY KANPUR**
April 2001

20 JUL 2001 / ME

पुरुषोत्तम काणीनाथ केलकर पुस्तकालय
भारतीय प्रौद्योगिकी संस्थान कानपुर
अवाप्ति क्र० A... 134278

TH

ME/2001/ M

Sw 14 e



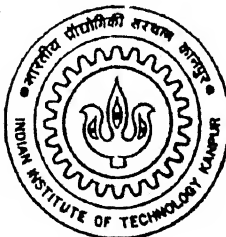
A134278

AN EXPERIMENTAL STUDY OF CONVECTIVE HEAT TRANSFER FROM FLAT AND RIBBED SURFACES

A Thesis Submitted
In Partial Fulfilment of the Requirements
for the Degree of
Master of Technology

by

Sangram Kishore Swain



to the
DEPARTMENT OF MECHANICAL ENGINEERING
INDIAN INSTITUTE OF TECHNOLOGY KANPUR
INDIA
April, 2001

CERTIFICATE

It is certified that the work contained in the thesis entitled "*An Experimental Study of Convective Heat Transfer From Flat and Ribbed Surfaces*," by **Mr. Sangram Kishore Swain**, has been carried out under our supervision and that this work has not been submitted elsewhere for a degree.



K. Muralidhar
Professor
Dept. of Mechanical Engineering
I.I.T. Kanpur 208016

(on leave)

P. K. Panigrahi
Asst. Professor
Dept. of Mechanical Engineering
I.I.T. Kanpur 208016

April, 2001

Abstract

Fluid flow passages roughened with repeated ribs are commonly employed for cooling gas turbine blades. The increased level of mixing induced by these ribs enhances the convective heat transfer in the blade cooling cavities. The present work is an experimental study to investigate the heat transfer and friction characteristics of flow in a rectangular channel with a solid rib placed on the lower wall. Heat transfer and fluid flow measurements have been presented for a smooth surface and one carrying a single rib. Liquid crystal thermography (LCT) has been employed to map the surface temperature profiles. The extra advantage of measuring the surface temperature by LCT compared to traditional method by thermocouples is clearly seen in the present work.

Experiments were performed on an aluminium plate of thickness 3 mm and dimensions 680 mm × 298 mm heated by a stainless steel foil, 0.045 mm thick. The rib used in this experiment had a square cross-section of 13 mm² area. It was placed at a distance of 130 mm from the leading edge of the plate. Fluid velocity was measured using a pitot static tube connected to a digital manometer. Fluid temperature was measured using thermocouples. The heat transfer and the fluid dynamic aspects of the ribbed surface have been compared with those for a flat plate.

The image processing system consisted of a high resolution RGB colour camera, a high speed PC and a 24-bit colour frame grabber board. The software used to analyse images was capable of acquiring, freezing, sequential grabbing of images with specific functions such as determination of red, green, blue values and also hue values. Liquid crystal used in the present experiment was in the form of a sheet with an activation of the red colour of this particular crystal beginning at 35°C and a bandwidth of 5°C.

The present study was directed towards achieving following objectives : (a) generate skin friction coefficient and heat transfer data pertinent to flow of air over a heated surface, (b) generate skin friction coefficient and heat transfer data pertinent to flow of air over a ribbed surface, (c) comparison of Nusselt number for smooth and ribbed surfaces, (d) describe the methodology associated with measuring temperature distribution on a test surface using liquid crystals and, (e) to estimates the temperature difference ahead and beyond the rib in a forced convection test under transient and steady conditions.

The main findings of present work are:

1. The ribbed surface produces flatter velocity profiles than a smooth surface. The flatter velocity profile and a higher turbulence intensity lead to a higher heat transfer enhancement.
2. There was significant increase in the average Nusselt number, boundary layer thickness and skin friction coefficient for the ribbed surface compared to a smooth surface.
3. It was possible to measure temperature distribution clearly on a heated test surface using liquid crystals.

Acknowledgement

I feel immense pleasure and satisfaction by working with Prof. P. K. Panigrahi and Prof. K. Muralidhar for their brilliant guidance throughout the period of my M.Tech thesis helped to surpass all the obstacles smoothly. Their company not only enrich my knowledge but also wider my ways of thinking. I am indebted to them for many fruitful discussions and perspicacious guidance.

I am thankful to Mr. Andallib Tariq for his constant encouragement, invaluable suggestions and generous help on different occasions during my thesis work.

Special thanks to Mr. Rajesh, Mr. Sambunath, Mr. Saroj for their co-operation in fabricating of my experimental set up and other accessories.

I would like to thank all the members of our Lab, especially Mr. Sunil, Ms. Tanuja, Tara, Atul, Dutta, Subrata and Anamika for their constant company in the laboratory.

My family members were a constant source of encouragement for me throughout this work. I am sincerely thankful for the patience they kept in last more than one and half year.

I am also thankful to my friends especially Vikas, Sanjay, Vishwadeep and Santosh for making my stay at IIT kanpur enjoyable. I should also express my special thanks to two of my closest friends Mr. Rabindranath Behera and Sanjay Ray for their constant encouragement during my stay at IIT kanpur.

I am very thankful to the All Mighty for giving me enough perseverance, patience and strength to rise after every debacle.

Sangram Kishore Swain

Contents

Certificate	i
Abstract	i
Acknowledgements	iii
Nomenclature	xii
1 Introduction	1
1.1 Literature Review	3
1.1.1 Heat Transfer Enhancement and Rib Turbulators	3
1.2 Objectives of the Present Work	6
2 Apparatus and Instrumentation	8
2.1 Wind Tunnel	8
2.2 Heating Section	9
2.3 Velocity and Temperature Measurement	10
2.4 Liquid Crystal Thermography	11
2.4.1 calibration	13

2.5 Rib Design	14
2.6 Uncertainty and measurement Errors	14
3 Data Reduction	17
3.1 Hydrodynamic Boundary-layer	18
3.2 Thermal Boundary-Layer	19
3.3 Liquid Crystal Thermography	23
3.3.1 Calibration Test	23
3.3.2 Transient Test	24
3.3.3 Steady State Test	24
4 Results and Discussion	26
4.1 Flow over a flat surface with Heat Transfer	26
4.1.1 Velocity Field	27
4.1.2 Thermal Field	27
4.2 Flow over a Ribbed flat surface with Heat Transfer	39
4.2.1 Velocity Field	40
4.2.2 Thermal Field	40
4.3 Comparison of Skin Friction coefficient with and without rib	52
4.4 Comparison Heat Transfer with and without the Rib	52
4.4.1 Local Nusselt Number	52
4.4.2 Average Heat Transfer Coefficient	58
4.5 Visualization of surface temperatures using liquid crystals	58

4.5.1	Transient test experiment analysis	58
4.5.2	Steady state Experiment	61
5	Conclusions and Scope for Future Work	68
5.1	Conclusions	68
5.2	Scope for future work	69
	Bibliography	70
	A Experimental Study of Natural Convection From Vertical and Horizontal Surfaces	73
	Appendix A	73

List of Figures

2.1	Heating section	10
2.2	Schematic drawing of flow system and instrumentation	11
2.3	Schematic view of imaging system	13
2.4	Complete View of the Experimental set up	16
2.5	Closer view of the test section	16
4.1	Velocity profiles in Flow over a Flat surface	28
4.2	Velocity profiles in Flow over a Flat surface	28
4.3	Velocity profiles in Flow over a Flat surface	29
4.4	Variation of the hydrodynamic boundary-layer thickness for flow over a flat surface	29
4.5	Variation of the hydrodynamic boundary-layer thickness for flow over a flat surface	30
4.6	Variation of the hydrodynamic boundary-layer thickness for flow over a flat surface	30
4.7	Skin friction coefficient as a function of Reynolds number for a flat surface	31
4.8	Skin friction coefficient as a function of Reynolds number for a flat surface	31

4.9 Skin friction coefficient as a function of Reynolds number for a flat surface	32
4.10 Temperature profiles in flow over a flat surface	32
4.11 Temperature profiles in flow over a flat surface	33
4.12 Temperature profiles in flow over a flat surface	33
4.13 Variation of the thermal boundary-layer thickness for flow over a flat surface	34
4.14 Variation of the thermal boundary-layer thickness for flow over a flat surface	34
4.15 Variation of the thermal boundary-layer thickness for flow over a flat surface	35
4.16 Local Nusselt number variation with Reynolds number for flow over a flat surface	35
4.17 Local Nusselt number variation with Reynolds number for flow over a flat surface	36
4.18 Local Nusselt number variation with Reynolds number for flow over a flat surface	36
4.19 Average Nusselt number variation with Reynolds number for a flow over a flat surface	37
4.20 Average Nusselt number variation with Reynolds number for a flow over a flat surface	37
4.21 Average Nusselt number variation with Reynolds number for a flow over a flat surface	38
4.22 Velocity profiles in flow over a flat surface with a rib	41
4.23 Velocity profiles in flow over a flat surface with a rib	41

4.24 Velocity profiles in flow over a flat surface with a rib	42
4.25 Variation of the hydrodynamic boundary-layer thickness for a flow over a flat surface with a rib	42
4.26 Variation of the hydrodynamic boundary-layer thickness for a flow over a flat surface with a rib	43
4.27 Variation of the hydrodynamic boundary-layer thickness for a flow over a flat surface with a rib	43
4.28 Skin friction coefficient as a function of Reynolds number for a flat surface with a rib	44
4.29 Skin friction coefficient as a function of Reynolds number for a flat surface with a rib	44
4.30 Skin friction coefficient as a function of Reynolds number for a flat surface with a rib	45
4.31 Temperature profiles in flow over a flat surface with a rib	45
4.32 Temperature profiles in flow over a flat surface with a rib	46
4.33 Temperature profiles in flow over a flat surface with a rib	46
4.34 Variation of thermal boundary-layer thickness for flow over a flat surface with a rib	47
4.35 Variation of thermal boundary-layer thickness for flow over a flat surface with a rib	47
4.36 Variation of thermal boundary-layer thickness for flow over a flat surface with a rib	48
4.37 Local Nusselt number variation with Reynolds number for a flow over a flat surface with a rib	48
4.38 Local Nusselt number variation with Reynolds number for a flow over a flat surface with a rib	49

4.39 Local Nusselt number variation with Reynolds number for a flow over a flat surface with a rib	49
4.40 Average Nusselt number variation with Reynolds number for a flow over a flat surface with a rib	50
4.41 Average Nusselt number variation with Reynolds number for a flow over a flat surface with a rib	50
4.42 Average Nusselt number variation with Reynolds number for a flow over a flat surface with a rib	51
4.43 Comparison of skin friction coefficient for flow over a flat surface with and without a rib	53
4.44 Comparison of skin friction coefficient for flow over a flat surface with and without a rib	53
4.45 Comparison of skin friction coefficient for flow over a flat surface with and without a rib	54
4.46 Comparison of local Nusselt number for flow over a flat surface with and without a rib	54
4.47 Comparison of local Nusselt number for flow over a flat surface with and without a rib	55
4.48 Comparison of local Nusselt number for flow over a flat surface with and without a rib	55
4.49 Comparison of Average Nusselt number for a flow over a flat surface with and without a rib	56
4.50 Comparison of Average Nusselt number for a flow over a flat surface with and without a rib	56
4.51 Comparison of Average Nusselt number for a flow over a flat surface with and without a rib	57

4.52 Calibration curve showing the relationship between the displayed hue and surface temperature.	59
4.53 Calibration curve showing the relationship between the displayed R, G, B and surface temperature.	59
4.54 Liquid crystal images showing the color changes during cooling of plate at 300 rpm during the Transient experiment.	62
4.55 Transient temperature contours at 300 rpm.	63
4.56 Liquid crystal images showing the color changes during cooling of plate at 500 rpm during the Transient experiment.	64
4.57 Transient temperature contours at 500 rpm.	65
4.58 Liquid crystal images showing the color changes at different heat flux at 500 rpm during the steady state experiment.	66
4.59 Steady state Temperature contours.	67
A.1 Heating section in natural convection	74

Nomenclature

A	Surface area, m^2
C_f	Skin friction coefficient
C_p	Specific heat, $J/kg\cdot K$
D_e	Hydraulic diameter of channel, m
h	Heat transfer coefficient, $W/m^2\cdot K$
H	Height of rib, mm
k	Thermal conductivity of air at average temperature, $W/m\cdot K$
k_b	Thermal conductivity of bakelite, $W/m\cdot K$
L	Length of heated section, m
Nu_L	Average Nusselt number
Nu_x	Local Nusselt number at location x, from one end
Pr	Prandtl number
q_w	Wall heat flux, W/m^2
Re_L	Average Reynolds number
Re_x	Local Reynolds number
t	Thickness of bakelite sheet, mm
T_w	Average wall temperature, $^\circ C$
$T_w(x)$	Local wall temperature, $^\circ C$
$T(x, y)$	Local air temperature, $^\circ C$
T_∞	Free stream temperature, $^\circ C$
u	Velocity of air within boundary-layer, m/s
U_∞	Free stream velocity, m/s
W	Width of rib, mm

Greek Symbols

- μ dynamic viscosity, kg/sec-m²
 ρ Density, kg/m³
 δ Hydrodynamic boundary layer thickness, mm
 δ_T Thermal boundary layer thickness, mm
 τ_w Wall shear stress, N/m²
 θ Non-dimensional temperature gradient
 ϵ Emissivity of aluminium plate
 σ Stefan-Boltzmann constant, 5.67×10^{-8}

Subscripts

- L Average value
 w Average wall condition
 x At axial location x
 ∞ Condition at boundary layer

Chapter 1

Introduction

Improvement of the heat transfer process is desired in heat exchangers to enable reduction in weight and size, to increase the heat transfer rate or to diminish the mean temperature difference between the fluids and thus to improve the overall process efficiency. In gas turbine cycles the turbine inlet temperature needs to be very high to improve the cycle efficiency. Often the temperature level is well above the maximum allowable material temperature. Efficient cooling of the first rows of guiding vanes and blades is therefore very important. However only a limited amount of the air flow is available for such cooling and therefore efficient heat transfer is required. Highly efficient cooling technologies such as film cooling, impingement cooling, and rib augmented cooling are employed in practice for the turbine blades. In general, film cooling is imposed on the external surface of the blades. Forced cooling is arranged inside the blades by means of cooling passages.

The basic idea of the heat transfer augmentation is to not only disturb the velocity and temperature profiles close to the wall but also to create a secondary flow that will exchange heat and momentum between the wall region and the core region. The methods being used for heat transfer enhancement are classified as active or passive. The active methods require external power such as surface vibration, electric or acoustic fields. The passive methods use surface modification on specific types of surface geometries and in some cases fluid additives are used to accomplish the enhancement. The rib turbulators are the principal means to enhance heat transfer for internal cooling. These ribs increase the heat transfer in the channel flows by increasing the heat transfer area (fin effect) and by disturbing

the laminar sublayer (roughness effect). The flow passages (which may be of various geometries, for example tubular or rectangular) or surfaces of devices such as heat exchangers, advanced gas-cooled reactor fuel elements, and electronic cooling devices are usually roughened or dimpled to improve the convective heat transfer. The roughness break up the viscous sublayer and promotes local wall turbulence. This, in turn increases the heat transfer from both the rough and smooth surfaces, but as it also increase the pressure drop it is of interest to find out a roughness geometry that will yield a given heat transfer augmentation with minimum pressure increase.

Liquid crystal thermography (LCT) is a temperature measurement technique which provides temperature field information over a heated surface. It is contrary to the traditional temperature measurement technique like thermocouples where point temperature information can be obtained. Liquid crystal thermography has recently become widely used due to its highly accurate full-field, high-resolution results as well as its simplicity and cost efficiency. Thermochromic liquid crystal exhibit wavelength-dependent reflectivity that changes with temperature. They are particularly suitable for the measurement of surface temperature over a complete area and have been used by many workers from different research groups to measure heat transfer coefficients. The crystals are supplied in a robust encapsulated form and are glued to the surface to form a layer between 10 and 20 μm thick. This temperature-sensitive coating is typically illuminated from a diffuse source and the reflected light monitored with a color CCD camera. Mapping temperature and heat transfer distribution using liquid crystals have become a common practice for surface heat transfer measurement.

The study of flow past surface mounted ribs using liquid crystal thermography has been the focus of numerous investigations. These studies have been motivated by the desire to understand the fundamental physics of such flows due to their numerous practical applications, such as the internal coolant channels of gas turbine blades, internally ribbed heat exchangers and in electronic cooling.

1.1 Literature Review

Various cooling methods have been developed over the years in an evolutionary manner with the objective to achieve maximum internal heat transfer coefficient while minimizing the coolant flow rate in the channel. Heat transfer coefficients in the cooling passage can be increased by roughening the walls of the passage . A variety of investigations concerning rib-roughened walls in square and rectangular duct exist. However, depending on the application, the design of the ribs will be different. In radiator tubes or ducts the manufacturing process will result in ribs with radius of curvature of the same order of magnitude as the rib height. For internal cooling ducts of the gas turbine blades and wall cooling ducts of a combustor, the ribs may have sharp corners, i.e the cross section of the ribs will be like a square or a rectangle. If the ribs are perpendicular to the main flow, the shape of the ribs will have a significant influence on the pressure drop and heat transfer, but if the ribs are inclined and a secondary flow is setup, the actual rib shape might be less important.

1.1.1 Heat Transfer Enhancement and Rib Turbulators

Geometric parameters such as channel aspect ratio (AR), rib height-to-passage hydraulic diameter (e/D_h) or blockage ratio, rib angle of attack(α), the manner in which the ribs are positioned relative to one another (for example in-line, staggered, and criss cross) rib pitch-to-height ratio (s/e) and rib shape (round verses sharp corners, fillets, rib aspect ratio (AR_t), and skewness toward the flow direction) have pronounced effects on both local and overall heat transfer coefficients. Some of these effects have been studied by many investigators.

Burggraf (1970) reported the results of turbulent airflow in a square duct with transverse *solid type ribs* on two opposite walls for Reynolds number ranging from 13,000 to 130,000. The wall temperature distributions were measured by thermocouples. With a hydrodynamically fully developed condition at the heated duct entrance, the average Nusselt number of the ribbed side wall and friction factor were approximately 2.38 and 8.6 times the corresponding values for fully developed smooth duct flows, respectively. The average Nusselt number of the ribbed side wall was 19 percent greater than for the duct with four smooth walls.

Solntsev et al. (1973) conducted an experimental investigation on heat transfer in the vicinity of sudden two- and three-dimensional steps of *circular* and *square* cross-sectional areas mounted on a flat surface in an open channel. They reported enhancements in heat transfer coefficient for a range of Reynolds number between 10^4 to 10^5 .

Han et al. (1978, 84, 85) investigated systematically the effects of the rib pitch, rib height, rib spacing, and the rib angle of attack on the average heat transfer and the average pressure drop for the fully developed turbulent flow in a uniformly heated, straight, square channel with two opposite rib-roughened walls. They found that a *symmetrical rib* arrangement gave the same results as a *staggered rib* arrangement and that the rib shape influenced the friction factor but had only a modest effect on the heat transfer coefficient. Metzger et al. (1988) used a *thermal transient technique* to examine the contribution of the rib heat transfer to the overall heat transfer of a rib- roughened walls with variations in rib angle of attack and pitch. *Square ribs* representing a blockage ratio of 0.14 were mounted on only one wider side of a 0.154 aspect ratio rectangular channel. The main conclusions were that heat transfer on the rib surface significantly contributed to the overall rib- roughened wall heat transfer and this contribution mainly depends on the rib pitch to height spacing with very little effect from the rib angle.

Internal coolant passages in a turbine blade are serpentine with several sharp 180° turns connecting straight sections. Boyle (1984), Han et al. (1988, 91), Chandra et al. (1988), Chyu(1991) presented heat transfer results for smooth and ribbed *multi-pass channels*. Boyle (1984) used heaters and thermocouples to measure heat transfer whereas all the other studies for two- or three-pass channels used a heat/mass transfer analogy to measure local heat transfer distribution. They reported that the local Sherwood numbers on ribbed walls were 1.5 to 6.5 times those for a fully developed flow in a smooth square channel. They also reported that a 60° angled rib produces higher enhancement compared to 45° and 90° ribs.

Hung and Lin (1992) positioned a two dimensional turbulence promoter on the vertical wall opposite a heated wall containing an array of two-dimensional *rectangular rib* elements and found that it improved the heat transfer character-

istics in the duct and reduced the occurrence of hot spots.

Acharya et al. (1993) performed numerical as well experimental investigations to obtain periodic fully developed flow and heat transfer results for a ribbed duct, using the nonlinear and standard $K - \epsilon$ turbulence models.

Zhang et al. (1994) reported the effect of compound turbulators on friction factors and heat transfer coefficients in rectangular channels with two opposite *ribbed-grooved* walls for a Reynolds number range of 10,000 to 50,000. They proposed that grooved placed between adjacent ribs could improve the overall heat transfer by creation of vortices, which would increase the exchange between the fluid and the wall. An investigation for a rectangular duct with aspect ratio 10, two ribbed walls with $e/D_h = 0.028$ and $p/e = 10$ was carried out. Grooves were created midway between two adjacent ribs. The results show that the heat transfer performance of the rib-groove roughened duct is much better than the rib roughened duct.

Hwang and Liou (1994) focused on the heat transfer enhancement in a channel containing perforated ribs. The parameters investigated were rib open-area ratio ($\beta = 0$ to 44 percent), rib pitch-to-height ratio ($Pi/H = 5$ to 10), and rib height-to-channel hydraulic diameter ratio ($H/De = 0.081$ to 0.162). An important finding they reported was that the ribs with $\beta = 44$ percent gave the best thermal performance among the rib open area ratios investigated. In addition, the permeable ribbed geometry provides a higher thermal performance than the solid-type ribbed one.

Kukreja et al. (1996, 98) have performed the investigation using *liquid crystal thermometry*. The detailed local heat transfer distributions have been determined for turbulent flow through a long, straight, square test channel model with ribs of various configurations, including perforated ribs, on two opposite walls. Angled and V-shaped solid ribs enhance more heat transfer than transverse solid ribs, and further V-shaped ribs have been recommended for internal cooling of gas turbine blades. Perforated ribs enhance heat transfer to a lesser degree than solid ribs. Thus increasing the size or the number of holes, or total hole area, lowers the overall heat transfer.

Ekkad and Han (1997) presented detailed Nusselt number distributions in

the 180° turn region of a two pass smooth square channel and studied the effect of various rib turbulators on a two-pass square channel with one ribbed wall, using a transient heat transfer technique with a liquid crystal coating on the test surfaces. They studied channels with 90° parallel, 60° parallel, $60^\circ V$, and 60° broken V -rib configurations. From their results, it is possible to identify the flow separation, reattachment and secondary flow phenomena in the rib turbulated channels from the detailed heat transfer distributions. Later, Ekkad et al. (1998) compared the previous results (Ekkad and Han, 1997) with detailed heat transfer distribution data in a two-pass square channels with rib turbulators and *bleed holes*. Regional- averaged heat transfer results indicate that a surface with bleed holes provides similar heat transfer enhancement as that for a surface without bleed holes although (20-25) percentage of the inlet mass flow exits through the bleed holes.

Mochizuki et al. (1999) have carried out detailed measurement of heat transfer and fluid flow in turbulent flow through smooth and rib-roughened two straight, rectangular channels with a 180° sharp bend. For monitoring detailed distribution of local heat transfer coefficients over the four wall surfaces of the entire channel, more than 450 thermocouples have been used. Ribs have been attached to two opposite walls with an angle of 90° or 60° to the flow. Flow visualization tests have been performed which reveal the generation of secondary flows.

Taslim et al. (1996) used liquid crystal thermography to determine the local Nusselt numbers in a square duct with *angled*, *V-shaped* and *discrete ribs* on two opposite walls. Only one wall was heated with a constant heat flux, while the other walls were adiabatic. Their results indicated that the heat transfer was highest for V-shaped ribs pointing downstream, contrary to the results of Han et al. (1991).

1.2 Objectives of the Present Work

The present study is concerned with heat transfer enhancement from a flat surface using a solid rib and measurement of surface temperature by use of liquid crystal thermography for low heating level. The heating section is made of an aluminium

plate of dimension 680 mm×298 mm×3 mm in order to achieve a uniform wall temperature boundary condition. The study is carried out with three different heating levels and five motor speed.

The present experimental investigation is directed towards achieving the following objectives: (a) to generate friction and heat transfer data pertinent to heating of air in a rectangular smooth channel with lower wall subjected to uniform wall temperature, (b) to generate friction and heat transfer data pertinent to heating of air in the same channel with a square rib-roughness mounted at a distance of 130mm from the leading edge of the lower wall subjected to uniform wall temperature, (c) comparison of Nusselt number in smooth and ribbed channels, (d) describe in detail the methodology associated with measuring the band of colour on a test surface under forced convection conditions and, (e) to find out difference in temperature distribution ahead of and beyond the rib in a forced convection test.

Velocity measurements have been carried out using a pitot static tube connected to a digital manometer. Temperature in the thermal boundary-layer have been measured using a K-type thermocouple connected to a digital multimeter. Wall temperature distributions have recorded with liquid crystal sheets connected to a CCD camera.

Chapter 2

Apparatus and Instrumentation

The present study reports heat transfer measurements from heated surfaces exposed to a flow field. The experimental facility comprises of the wind tunnel, the heating section, traverse mechanism and the imaging system. Though set up looks simple in appearance, each and every part is fabricated with care and designed with various factors taken into account. For example, producing uniform low turbulence requires that the contraction cone should be smooth with a proper profile.

2.1 Wind Tunnel

The wind tunnel is of the open loop type which operates with the fan in the suction mode. The ambient air flow is sucked from the temperature controlled room into the test section through a flow straightener and five screens in the settling chamber and a 3:1 contraction cone. This air flows through the bell shaped contraction cone, the heated section, the unheated length of the duct and is then exhausted by a centrifugal fan that is run by a 3 phase motor. Speed control is accomplished using a frequency converter. The settling chamber is 1950 mm long and has a rectangular cross section of 500 mm by 1000 mm. The test channel is 3300 mm long with an aspect ratio of 29.8:16, (160 mm × 298 mm in the vertical plane). The test channel is made of perspex sheet of 12 mm thickness. Velocities in the range 1-4 m/s are presently realizable in the tunnel. The free stream turbulence was seen to be quite small, but remains as yet to be

quantified.

2.2 Heating Section

The heating section which is an assembly of an aluminium plate, bakelite sheets, and a stainless steel foil as shown schematically in Figure 2.1.

The heating section is situated just at the entrance of test duct. The test plate is 730 mm long and is located flush with the bottom wall. It serves as the heat transfer surface, both as a smooth and one roughened by a rib, while the top and two vertical walls are smooth and thermally insulated. Downstream of the test duct is an unheated section made of perspex with the same cross section. The heat transfer surface is constructed using a single aluminium plate (680 mm × 298 mm × 3 mm). There are six stainless steel foils of dimension 690 mm × 47 mm × 0.045 mm that are cemented on to the 25 mm thick bakelite sheet. These foils are electrically connected in series and finally connected to a variac for power supply. To prevent the aluminium plate from electrical contact the upper surface of the stainless steel foil is coated with varnish. A 2 mm mica sheet is placed between the bakelite and aluminium plate for better insulation. The surface of aluminium plate is highly polished to minimize emissivity, and hence the radiative losses. In addition, to minimize the conductive heat losses, lower surface of the bakelite board is insulated using a 13 mm thick of bakelite with a 2 mm thick air gap between them.

The heat transfer surface is also instrumented with thirteen calibrated thermocouples of the chromel-alumel type. The thermocouples are located inside the heated surface with omegabond 101 epoxy. Twelve thermocouples are distributed along the centerline of the heated plate for wall temperature measurement. In order to check the spanwise temperature uniformity, surface temperature along the lateral of the heated plate is also instrumented with one thermocouple. To maintain a smooth flow surface, the thermocouple beads are attached to the underside of the Aluminium plate fed through the opening made in the two bakelite sheets and mica. To measure the conduction losses, on the underside there are two thermocouple are mounted at the two sides of the upper bakelite sheet exactly on the same line. There are two more thermocouples are mounted at the two sides

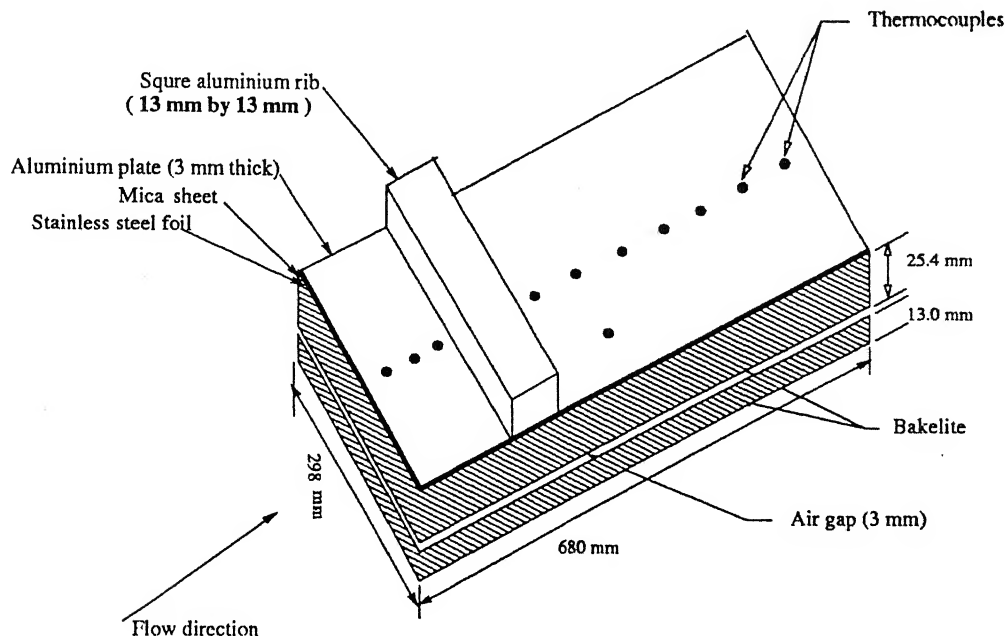


Figure 2.1: Heating section

of the lower bakelite sheet on the same line. This arrangement is repeated at a second location in the downstream.

2.3 Velocity and Temperature Measurement

For calculating the friction coefficient and Nusselt number, it is essential to measure velocity gradient and the temperature gradient in the flow field over the heated plate. For that reason, a slot of 12 mm has been cut along the longitudinal direction in perspex that forms the top wall of the duct. Five different T-keys were made to close the slot so that velocity and temperature measurement could be taken at four or five different locations above the heating plate. A micromanometer (FC012) with a pitot static tube as shown in Figure 2.2 has been employed to measure the distribution of velocity. The probe is mounted on a motor-driven linear translation stage and inserted from the top plate to traverse across the section to any desired location in the flow. The software is loaded in the PC to run the motor. The torque of motor is 4 Nm. One revolution of the motor is equivalent to 1 mm distance covered. Velocity distribution of air along the transverse direction is measured with 1 mm over the hydrodynamic boundary

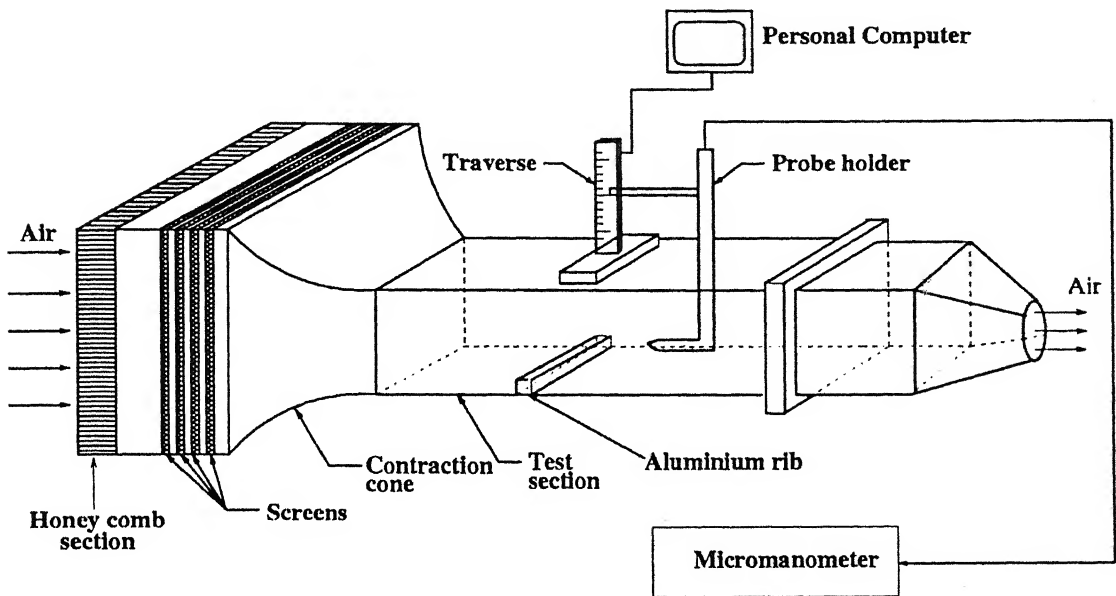


Figure 2.2: Schematic drawing of flow system and instrumentation

layer thickness. Similarly for measuring the temperature of air, a calibrated thermocouple is inserted through a hollow steel rod. This thermocouple is connected to a digital multimeter and an ice point to measure the temperature of the fluid above the heated plate. The steel rod is also mounted on the same motor driven linear translation stage and inserted from the top plate to traverse across the section to any desired location in the flow. The thermocouples inserted in the aluminium plate are connected to the digital multimeter and ice point to give the temperature at various locations of the plate.

2.4 Liquid Crystal Thermography

The liquid crystal technology is one of the important inventions of the twentieth century that has found many applications as a visualization tool today. Liquid crystals change their colour on applications of external stimulus, for example temperature and shear stress distributions and thus act as a measure of their change.

Liquid crystal is a unique substance, which exists between the solid and the isotropic-liquid phase of some organic compounds. It scatters incident light very

selectively. The theory behind its optical characteristics involves the behaviour of the molecular structure. Each liquid crystal compound possesses a helical structure with a characteristics pitch length. The helix pitch lengths are in the range of the wavelength of visible light. The pitch length can be altered by changing the external stimulus, typically, temperature and shear stress. since the fundamental chemical structure is unaffected by the external stimulus, a liquid crystal coating can respond repeatedly to the same physical changes.

The lowest temperature where liquid crystals scatters visible light is called the event temperature. At a temperature below the liquid crystal's event temperature, the liquid crystal will be in the solid state and will appear transparent. The clearing point temperature is the temperature at which the liquid crystal ceases to reflect visible light. When the temperature exceeds the clearing temperature point, the liquid crystal will enter the pure liquid state and appear transparent. The color output in liquid crystals is reversible and reproducible.

Liquid crystals are available in different bandwidths, which defines the temperature range in which it actively reflects visible light. Narrow-band crystals typically have bandwidths between 1°C and 2°C. They are used for accurate verification of surface temperature distribution of isothermal objects. The small range allows for highly accurate relative temperature measurements and simple imaging processing.

Wide-band crystals typically have bandwidths between 5°C and 20°C. They are useful when an object has large temperature variations. Practical applications of wide-band crystals include investigation of the surface temperature distribution on gas turbine blades or characterizing the temperature distribution on electronic components.

The perceived color of a liquid crystal begins red, continues to green, and finishes blue as the temperature increases. This is because the reflected color spectrum varies continuously from the longer wavelengths at red, to the shorter wavelengths towards blue. Liquid crystals materials are available in three forms: a pure coating, a sprayable liquid, and manufactured sheets (Farina). Pure liquid crystal materials can be directly used on small objects that require a high-level spatial resolution.

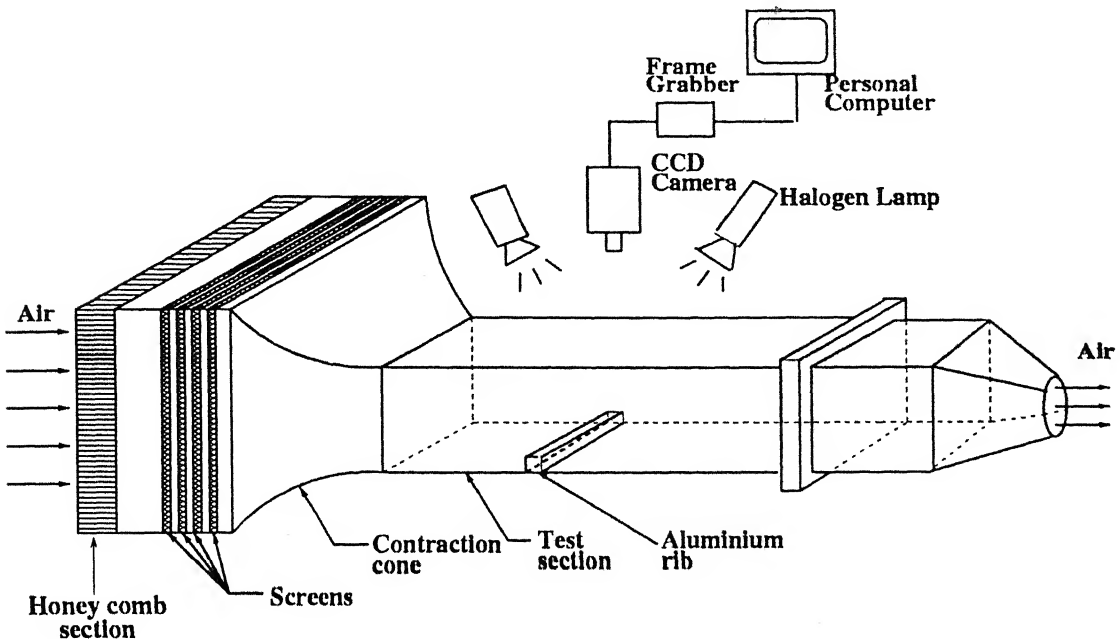


Figure 2.3: Schematic view of imaging system

2.4.1 calibration

The image processing system consists of a high resolution RGB colour camera, a high speed PC and a 24-bit colour frame grabber board as shown in figure 2.3. These systems store the appropriate intensities of red, green, and blue needed to produce a corresponding matched colour response at each point in an image. The frame grabber can be programmed for colour analysis using base level C-programs. However, several software programs are commercially available to analyse images. The software is capable of acquiring, freezing, sequential grabbing of images with specific functions such as determination of red, green, blue values and also the corresponding hue distribution. Hue, saturation, and intensity contain colour, colour purity, and relative brightness information respectively at each pixel.

Since the color response of liquid crystals can be affected by different environmental factors, the simplest way of producing a good calibration curve is to directly calibrate the crystals in place. This means the crystals are calibrated using the same methods used for controlling and measuring the temperature at or near the surface of interest. A consistent surface preparation and application technique is required to make liquid crystal performance repeatable and uniform.

The surface should be smooth and free of any dirt particles. The surface is coated with a thin layer of the liquid crystal with known band temperatures, behind a background of black paint layer. Liquid crystals are colourless under room temperature condition and this makes the test surface appear black initially. The liquid crystals used in present project are specified R35C5W. This means that the activation of the red color of this particular crystal begins at 35°C and the bandwidth is 5 degrees wide.

2.5 Rib Design

The role of a single rib in augmenting heat transfer from a flat surface has been examined in the present study. The rib serves two purposes in cooling passages. First it breaks the laminar sublayer and create a local wall turbulence. This in turn increases the level of mixing of the cooler core air with the warmer air closer to the channel wall, thereby enhancing the cooling capability of the passage. Secondly a rib increases the surface area which in turn enhances the heat transfer.

A variety of investigations concerning rib-roughened walls in square and rectangular duct exists. However depending on the application the design of the ribs can be different. The roughness increases the heat transfer coefficient but as it also increases the pressure drop, it is of interest to find a roughness geometry that will yield a given heat transfer augmentation with minimum increase in pressure drop.

A comparison of the rib geometry and the range of Reynolds numbers employed by various authors is summarized in Table 2.1

The complete view of the experimental set up with all the accessories are shown in Figure 2.4 and Figure 2.5 shows the closer view of the heating section used to study the enhancement by using a solid rib.

Table 2.1: Geometry of Ribs used by Previous Investigators

Authors;Year	Turbulator	W/H	H/ D_e	Re
Lockett and Collins	Ribs with sharp top corners	1.0	0.067	7400
Kukreja et al., 1993	V-shaped rib	1.0	0.0625	10,000-45000
Liou et al., 1990	Solid ribs	1.0	0.1	12,000-120,000
Liou and Hwang, 1992a	Solid ribs	1.0	0.063	5000-54,000
Liou and Hwang, 1993a	Solid ribs	1.0	0.067	12,600-54,000
Taslim et al., 1996	Angled, V-shaped ribs	1.0	0.083	5000-30,000
Olsson and Suden 1997a,b	Multiple V ribs	-	0.06	500-15,000
Present Work	single square rib	1.0	0.063	10,000-100,000

2.6 Uncertainty and measurement Errors

Errors in the experimental data are associated with measuring temperature by K-type thermocouples, fluctuating supply voltage at the variac and the focussed power source for lighting the liquid crystals. Errors related to K-type thermocouple effects have been found to be quite small. Most of the experiments were conducted several times to check temperature measurement. Still, the local Nusselt number and average Nusselt number were found to be in good agreement with theoretical correlations. The calibration process was repeated thrice. The result found to be repeatable. The image grabbed during the transient state test and the steady state test also showed good repeatability.

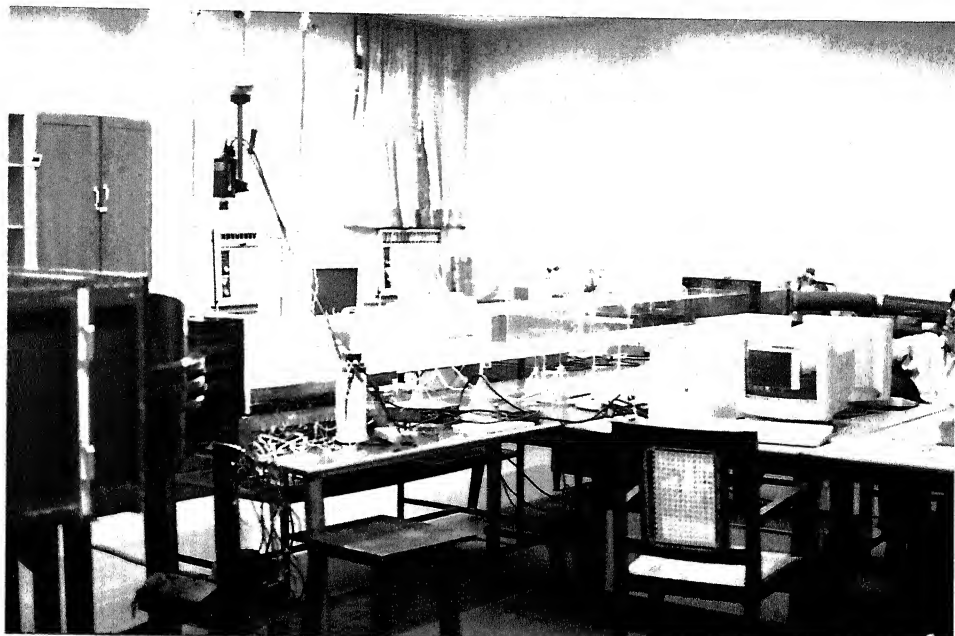


Figure 2.4: Complete View of the Experimental set up

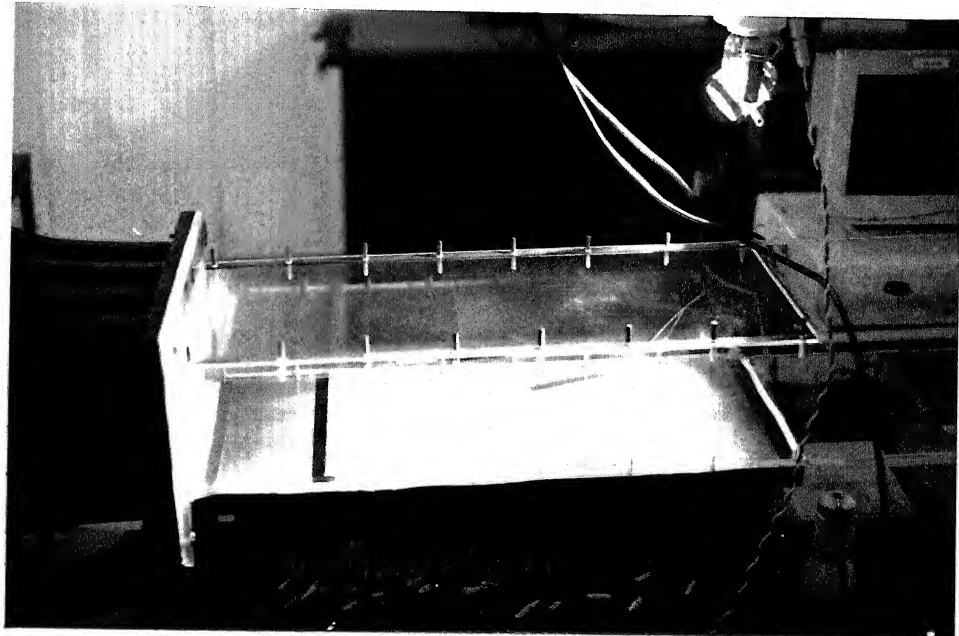


Figure 2.5: Closer view of the test section

2.6. UNCERTAINTY AND MEASUREMENT ERRORS

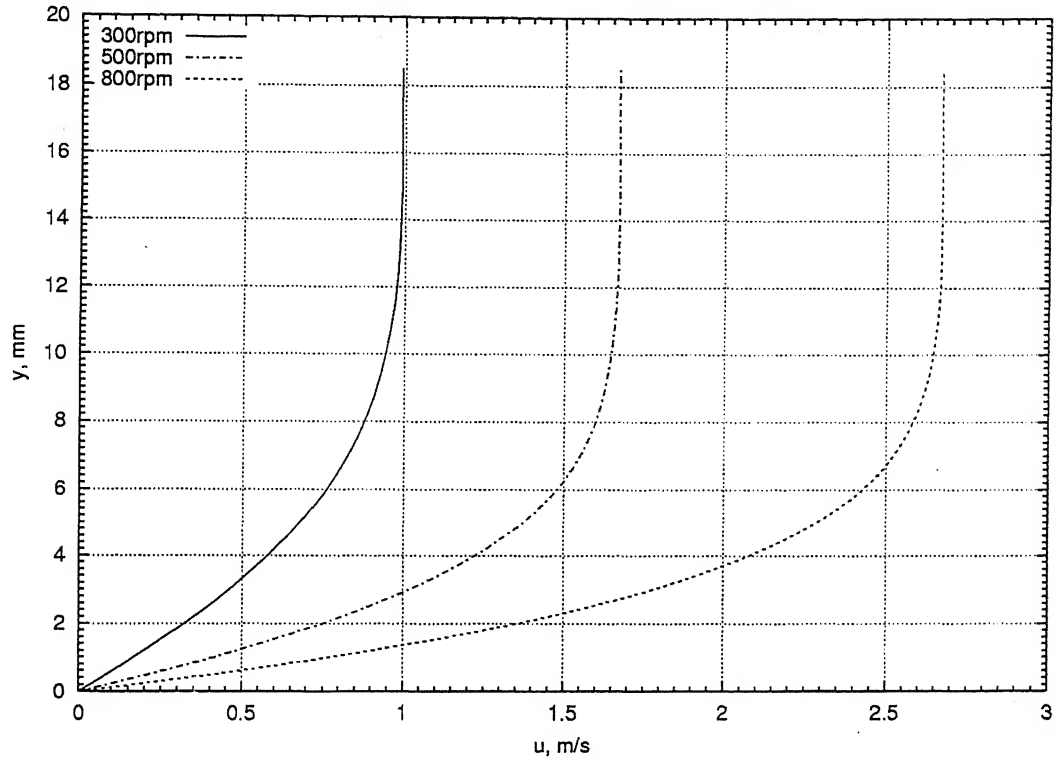


Figure 2.6: Velocity profile on a flat surface at a distance of 42 mm from the leading edge of the plate

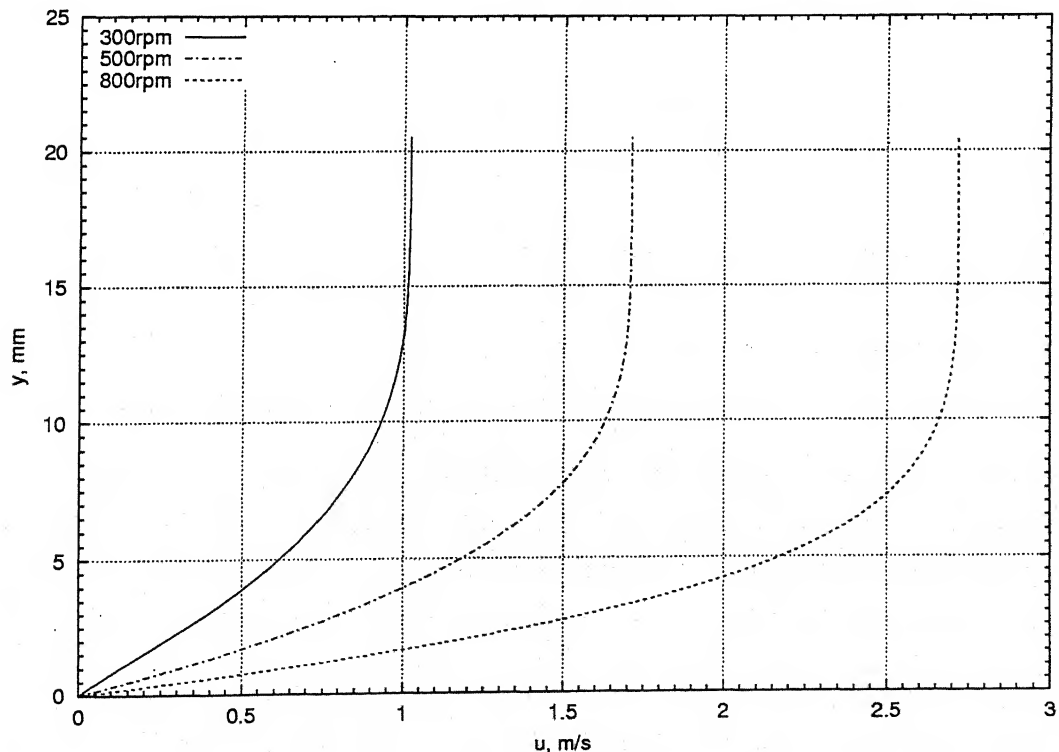


Figure 2.7: Velocity profile on a flat surface at a distance of 294 mm from the leading edge of the plate

Chapter 3

Data Reduction

The experiments with a smooth channel not containing the rib were conducted with three different heating levels and five motor speeds. Steady state was seen to be reached after seven or eight hours of continuous heating. After steady state was reached, the velocity distribution and the temperature profiles were measured at four locations. The temperature of the thirteen thermocouples inserted in the aluminium plate and four thermocouples which inserted in the bakelite sheet were measured in each experiment. The electrical voltage and current flowing through the foil was measured at the end of the experiment.

Similarly for the ribbed channel, experiments were conducted with three different heating levels and three motor speed. In this experiment steady state was reached slightly earlier than that of the smooth channel experiment. After steady state was reached, the velocity and temperature distributions at three locations were measured beyond rib. Temperature of the all thermocouples in the aluminium surface and the bakelite sheet were measured after steady state was reached.

The liquid crystals were calibrated under the no flow condition. The relationship between hue and temperature was thus obtained. Images were captured with two velocities and one heating level under transient conditions. Also one steady state image was captured for each of the three heating levels and a single velocity.

Quantities of interest to the present work are the velocity and temperature

profiles, skin friction coefficient and the local and the average Nusselt numbers.

3.1 Hydrodynamic Boundary-layer

The non-dimensional velocity distribution (u/U_∞) has been plotted against non-dimensional distance from the wall y/δ scaled by the boundary-layer thickness. The theoretical expression for non-dimensional velocity distribution in laminar flows can be obtained from the Blasius solution. The theoretical expression for the non-dimensional velocity distribution in turbulent flows is obtained from the law of the wall which is expressed as

$$u^+ = 2.44 \ln y^+ + 5.0 \quad (3.1)$$

where

$$u^+ = \frac{u/U_\infty}{\sqrt{\frac{C_f}{2}}} \quad (3.2)$$

and

$$y^+ = \frac{yU_\infty \sqrt{\frac{C_f}{2}}}{\nu} \quad (3.3)$$

The basic unknown in the above equation is C_f and can be calculated by using the boundary condition: $y = \delta$, $u = U_\infty$. Hence

$$\frac{u}{U_\infty} = \sqrt{\frac{\tau_w}{\rho U_\infty^2}} (2.44 \ln \frac{y}{\delta} \sqrt{\frac{\tau_w \delta^2}{\rho \nu^2}} + 5.0) \quad (3.4)$$

With C_f (or τ_w) determined from Equation 3.4 it is possible to get the plot of (u/U_∞) against (y/δ) for turbulent flow.

The non dimensional boundary layer thickness (δ/x) has been plotted against the local Reynolds number in the present work. The theoretical expression for (δ/x) as a function of local Reynolds number for laminar flow is given as

$$\frac{\delta}{x} = 5.0 \text{Re}_x^{-\frac{1}{2}} \quad (3.5)$$

The theoretical expression for (δ/x) as a function of local Reynolds number for turbulent flow is given as

$$\frac{\delta}{x} = 0.37 \text{Re}_x^{-\frac{1}{5}} \quad (3.6)$$

The skin friction coefficient can be determined by measuring the velocity gradient in the near wall region of the channel. It can be expressed as

$$C_f = \frac{\mu(du/dy) |_{y=0}}{\frac{1}{2}\rho U_\infty^2} \quad (3.7)$$

where the wall velocity gradient is determined fitting a quadratic curve through the near-wall values of velocity. In Equation 3.1, μ and ρ are fluid properties determined at average temperature $(T_w + T_\infty)/2$. Further U_∞ is the free stream velocity.

The theoretical expression for the skin friction coefficient in laminar flow over flat plate is given by

$$C_f = 0.644 \text{Re}_x^{\frac{1}{2}} \quad (3.8)$$

when $\text{Re}_x < 5 \times 10^5$, x being measured from the leading edge of the aluminium plate. The theoretical expression for the skin friction coefficient in turbulent flow over a flat plate is given by

$$C_f = 0.0592 \text{Re}_x^{-\frac{1}{6}} \quad (3.9)$$

when $5 \times 10^5 < \text{Re}_x < 10^7$, assuming that the boundary-layer is fully turbulent from the leading edge.

3.2 Thermal Boundary-Layer

The non-dimensional temperature θ is defined as

$$\theta = \frac{T_w(x) - T(x,y)}{T_w(x) - T_\infty} \quad (3.10)$$

Here $T_w(x)$ is the temperature of the plate at that point where the temperature profile is measured. The local fluid temperature is indicated by $T(x,y)$. T_∞ is the

free stream temperature.

The theoretical non-dimensional temperature variation for laminar flow is obtained from Blausis solution. The theoretical non-dimensional temperature variation for turbulent flow is can be obtained from law of wall which is expressed as follows

$$t^+ = 2.075 \ln y^+ + 3.9 \quad (3.11)$$

where

$$t^+ = \frac{(T_w(x) - T(x, y)) \sqrt{\frac{\tau_w}{\rho}}}{q_w / \rho c_p} \quad (3.12)$$

Here τ_w , the wall shear stress is obtained as in section 3.1. In this equation only q_w is unknown. It can be obtained by applying the boundary condition, $y = \delta_T$, $T = T_\infty$. Thus

$$\frac{T_w(x) - T(x, y)}{T_w(x) - T_\infty} = \sqrt{\frac{q_w^2}{\tau \rho c_p^2 (T_w(x) - T_\infty)^2}} (2.075 \ln \frac{y}{\delta_T} \sqrt{\frac{\tau_w \delta_T^2}{\rho \nu^2}} + 3.9) \quad (3.13)$$

From above equation one can solve for q_w and subsequently plot $\theta(x, y)$ as a function of $\frac{y}{\delta_T}$.

In the present work, plot was also obtained between δ_T/x against Reynolds number. The theoretical expression for δ_T/x for laminar flow is given as:

$$\frac{\delta_T}{x} = 5.496 \text{Re}_x^{-\frac{1}{2}} \quad (3.14)$$

The theoretical expression for δ_T/x in turbulent flow is given as:

$$\frac{\delta_T}{x} = 0.4067 \text{Re}_x^{-\frac{1}{2}} \quad (3.15)$$

The local convective heat transfer coefficient of the heated surface is presented in terms of the local Nusselt number Nu_x defined as

$$\text{Nu}_x = \frac{-x}{T_w(x) - T_\infty} \frac{dT}{dy} \Big|_{y=0} \quad (3.16)$$

Here the air temperature gradient $\frac{dT}{dy} \Big|_{y=0}$ is determined by fitting quadratic function through the near wall values for temperature. The local wall temperature

$T_w(x)$ is read from the thermocouple output at that particular point. In Equation 3.10, T_∞ is free stream temperature.

The theoretical expression for the local Nusselt number for laminar flow is given by

$$\text{Nu}_x = 0.332 \text{Re}_x^{\frac{1}{2}} \text{Pr}^{\frac{1}{3}} \quad (3.17)$$

This is applicable for $\text{Re}_x < 5 \times 10^5$ and $0.6 < \text{Pr} < 50$. The theoretical expression for the local Nusselt number for turbulent flows is given by

$$\text{Nu}_x = 0.0296 \text{Re}_x^{-0.2} \quad (3.18)$$

when $5 \times 10^5 < \text{Re}_x < 10^7$

The properties of air were calculated at the film temperature

$$T_f = \frac{T_w(x) + T_\infty}{2}$$

The average heat transfer coefficient can be determined by applying the energy balance principle and the plate averaged Nusselt number can be evaluated by the following equation

$$\text{Nu}_L = \frac{q_{net}L}{A(T_w - T_\infty)k} \quad (3.19)$$

where q_{net} represents the net heat transfer to coolant and is calculated by subtracting the total heat loss from the electrical power dissipated by the heater. The electrical power generated from the heater is determined from the measured current and voltage through the foil. The total heat loss includes the conductive heat loss from rear side of the heated plate and the vertical adiabatic plates to the environment, and the radiative heat from loss the plate to its surroundings. Here T_w is an average of the thirteen thermocouples reading and T_∞ is the free stream temperature.

Sample Calculation

Measured data for 300 rpm and 587.49 W/m² power input are as follows

Temperature of plate, T_w	=	61.56°C
Ambient air temperature, T_∞	=	20°C
Voltage supplied to the foil, V	=	15.81 Volt
Current flows through the foil, I	=	7.53 amp
Length of the plate	=	0.68 m
Width of the plate	=	0.298 m
Thickness of lower bakelite(t)	=	0.013 m
Conductivity of bakelite(k_b)	=	0.23 W/m. $^\circ\text{C}$
Temperature of upper side of lower bakelite(T_1)	=	47°C
Temperature of lower side of lower bakelite(T_2)	=	38.5°C
Emissivity(ϵ) of aluminium plate	=	0.1
Stefan-Boltzmann constant(σ)	=	5.67×10^{-8}
Bottom side area(A) = 0.68×0.298	=	0.20264 m ²
Side area	=	0.08097 m ²
Effective area(A_f) = A + 0.5 × Side area	=	0.2836 m ²
Conductivity(k) of air at film temperature(T_f)	=	27.3148×10^{-3}

Power input	=	$V \times I$	=	119.04 W
Radiation loss	=	$\sigma\epsilon A(T_w^4 - T_\infty^4)$	=	5.925 W
Conduction loss	=	$\frac{k_b A_f (T_1 - T_2)}{t}$	=	42.649 W
Net power input	=	$q - (q_{loss} + q_{Rloss})$	=	70.466 W
Average temperature difference	=	$T_w - T_\infty$	=	41.56°C
Average heat transfer coefficient, h	=	$\frac{q_{net}}{A(T_w - T_\infty)}$	=	$8.3682 \text{ W/m}^2.\text{ }^\circ\text{C}$
Average Nusselt number, Nu_L	=	$\frac{hL}{k}$	=	208.327

The average Nusselt number can also be calculated from the average temperature gradient as follows:

$$Nu_L = \frac{L}{T_w - T_\infty} \left(\frac{dT}{dy} \right) \Big|_{(avg)y=0} \quad (3.20)$$

The theoretical expression for the average Nusselt number in laminar flow is given as:

$$Nu_L = 0.664 Re_L^{1/2} Pr^{1/3} \quad (3.21)$$

The theoretical expression for the average Nusselt number in turbulent flow is given as:

$$Nu_L = 0.037 Re_L^{0.8} Pr^{1/3} \quad (3.22)$$

3.3 Liquid Crystal Thermography

Thermocromic liquid crystals were spread uniformly on the test surface before the rib and after the rib. The liquid crystal experiment performed in three phases.

1. Calibration test to relate colour with temperature.
2. Transient test with two velocities to show the changes of colour before the rib and the after the rib.
3. Steady state test to show the changes of colour before the rib and the after the rib.

3.3.1 Calibration Test

Prior to the quantitative temperature measurement over the test surface, the method of colour expression was defined and the relationship between the colour and temperature of the liquid crystal assessed with a calibration test. Although the colours of the liquid crystals are observed by a RGB-data acquisition systems R-, G-, and B-data are not used to calibrate the sheet. Instead, the RGB colour space is transformed to the hue-lightness-saturation colour space, because the hue value is a monotonic function of the dominant wavelength reflected by the crystals and is therefore best suited for a unique colour-to temperature relation. A perfectly lighted surface showed uniform background intensity of the colour over the entire test surface. The background intensity determines the clarity of the picture seen by camera. If the background intensity is low, then the picture is too dark and the camera cannot capture the actual colour change. If the background intensity is too high, then the actual colour is lost in the white-light effect. Therefore accurate background intensity determined to provide uniform lighting to obtain accurate colour change information.

The test surface was heated to a temperature of nearly 42°C. The reading of one thermocouple was monitored continuously by a multimeter which can give a millivolt reading upto five digits after the decimal point. Then the power supply was cut off. The calibration test was done under the no flow condition. The plate started to cool and images were captured at every 0.2°C temperature interval.

Nearly fifty images were captured during this calibration test. Sixty by sixty pixels selected in the image around the location where the thermocouple was placed. Then these images were processed in the PC to get the RED, GREEN, BLUE and hue values separately for those particular pixels. The RED, GREEN, BLUE and Hue values were averaged to get a single RED, GREEN, BLUE and hue value appropriate for the temperature. With appropriate curve fitting a plot was obtained between hue and temperature. This is the calibration curve which was used in transient and steady state experiment to determine temperature distribution from a particular image.

3.3.2 Transient Test

The transient heat transfer method has been applied by the authors to many different blade cooling problems. This method offers the significant advantage of yielding local heat transfer coefficients over complete test surfaces in a single experiment. The technique involves heating of the test plate upto a certain temperature. The flow is then started. The lighting arrangement and camera position are kept identical to that of the calibration test. After the plate reaches a particular temperature, then the power supply is cut off. Due to forced convection the plate starts to cool. Images are then captured at 2 minute intervals. This experiment was carried out for two blower speeds of 300 and 500 rpm. Using the calibration curve, temperatures at different points were evaluated and the temperature contours were drawn.

3.3.3 Steady State Test

In the steady state experiment the heater was operated at a low power input to heat the foil very slowly to a temperature within the bandwidth of the liquid crystal. Simultaneously the blower was run at 500 rpm. The colour was seen to change very slowly from red to green to blue. When thermocouple output on the multimeter showed a constant reading over a long time, steady state was assumed to have been reached. At steady state the colour of the liquid crystal did not change with time. The lighting arrangement and camera position were kept the same as that of the calibration test. The steady state image was captured for

obtaining the temperature distribution over the plate. This test was repeated for three different electrical powers for a given speed of the blower.

Chapter 4

Results and Discussion

Measurements of velocity profile, skin friction coefficient, temperature profiles and the local Nusselt number are reported in the following sections. The influence of a two dimensional rib of square cross section on the wall parameters has been studied. Liquid crystal images of the heated surface assist in interpreting the influence of the rib in creating flow disturbances and promoting heat transfer.

4.1 Flow over a flat surface with Heat Transfer

The experiments have been performed in test facility carrying a heated surface but without a rib. The power supplied to the aluminium plate in three experiments are:

1. 319-353 $\frac{\text{W}}{\text{m}^2}$
2. 518-587 $\frac{\text{W}}{\text{m}^2}$
3. 777-927 $\frac{\text{W}}{\text{m}^2}$

The limits for each setting indicate the extreme heat flux levels that could have been reached owing to line voltage fluctuations. The free stream velocities produced in the test cell are:

1. 0.98 m/s

2. 1.25 m/s
3. 1.60 m/s
4. 1.90 m/s
5. 2.25 m/s

since the blower speed was held constant by a electronic frequency controller, fluctuations in the free stream velocity were small.

4.1.1 Velocity Field

Figures 4.1, 4.2 and 4.3 show a plot between the dimensionless transverse coordinate y/δ and the dimensionless local velocity u/U_∞ drawn in order to analyze the flow character. All the points are seen to be close to the the laminar profile. At a higher heating level the velocity is somewhat scattered compared to a lower heating level. This could be due to a buoyancy effect at higher temperature. Figures 4.4, 4.5 and 4.6 show a plot of the dimensionless boundary-layer thickness δ/x as a function of local Reynolds number Re_x . The skin friction coefficient, C_f , is plotted as a function of Reynolds number in the Figures 4.7, 4.8 and 4.9. Close to the inflow plane, the measured data shows (8-10)% deviation from the laminar correlation. But as the Reynolds number increases these deviations becomes small. The boundary-layer thickness is defined here on the basis of 99% of the free stream velocity. The growth of the boundary-layer is clearly seen in all the graphs.

4.1.2 Thermal Field

Figures 4.10, 4.11 and 4.12 show a plot between dimensionless transverse coordinate and dimensionless local temperature to characterize the heat transfer aspects of flow. In all the three cases the temperature profiles follow a similar trend. The temperature data appears to be scattered near the entry region of the test cell, but these stabilize towards the exit. An unexpected observation to be seen in the temperature profiles is that the measured data is closer to the

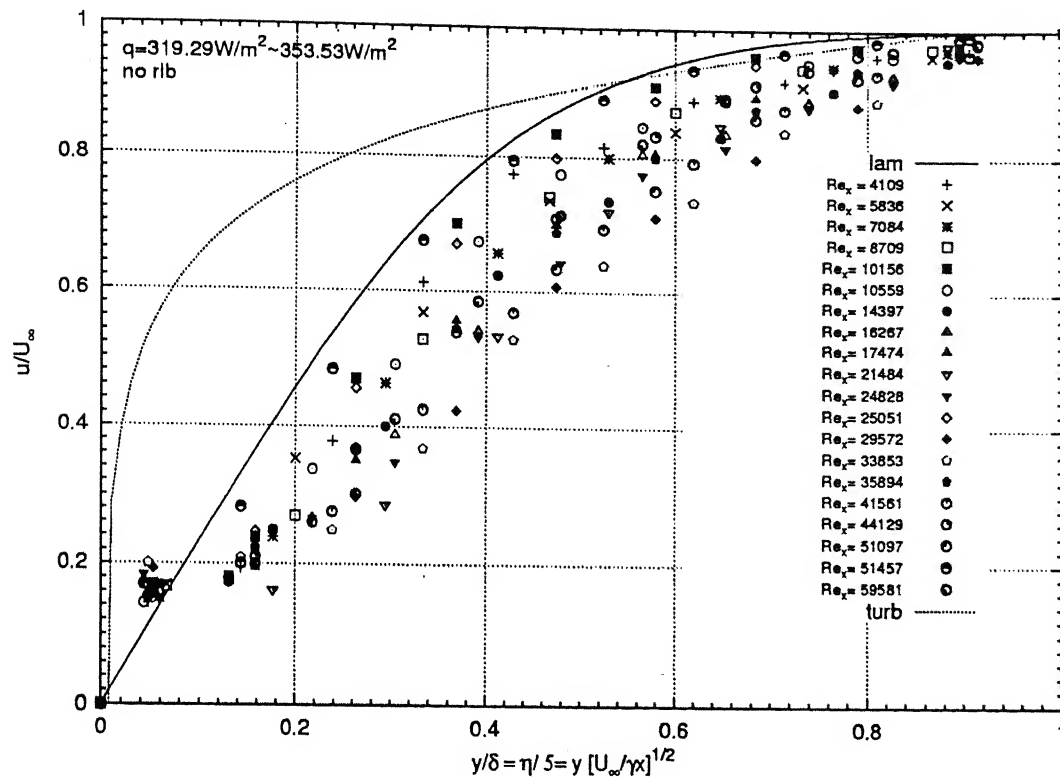


Figure 4.1: Velocity profiles in Flow over a Flat surface

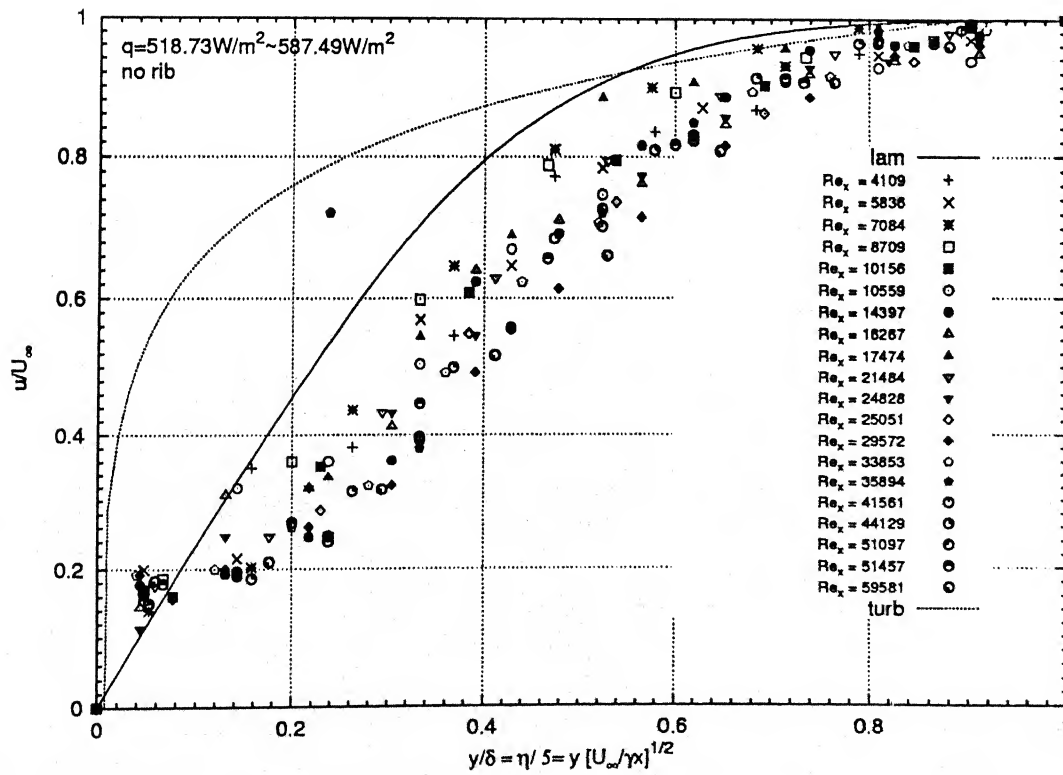


Figure 4.2: Velocity profiles in Flow over a Flat surface

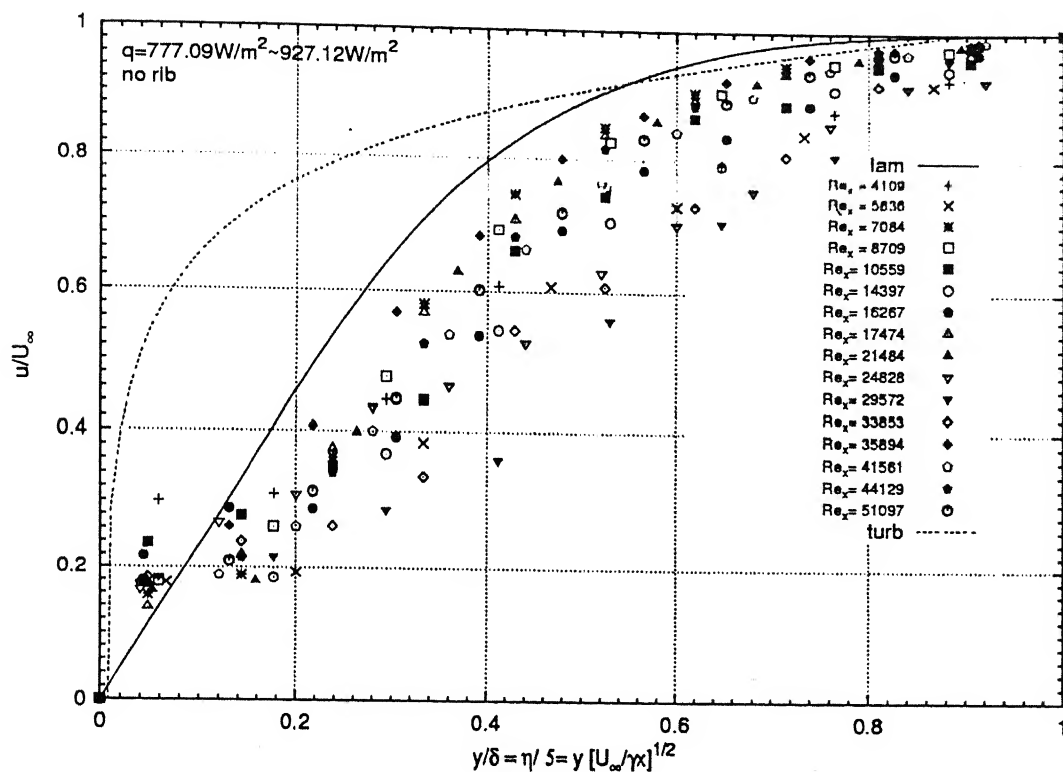


Figure 4.3: Velocity profiles in Flow over a Flat surface

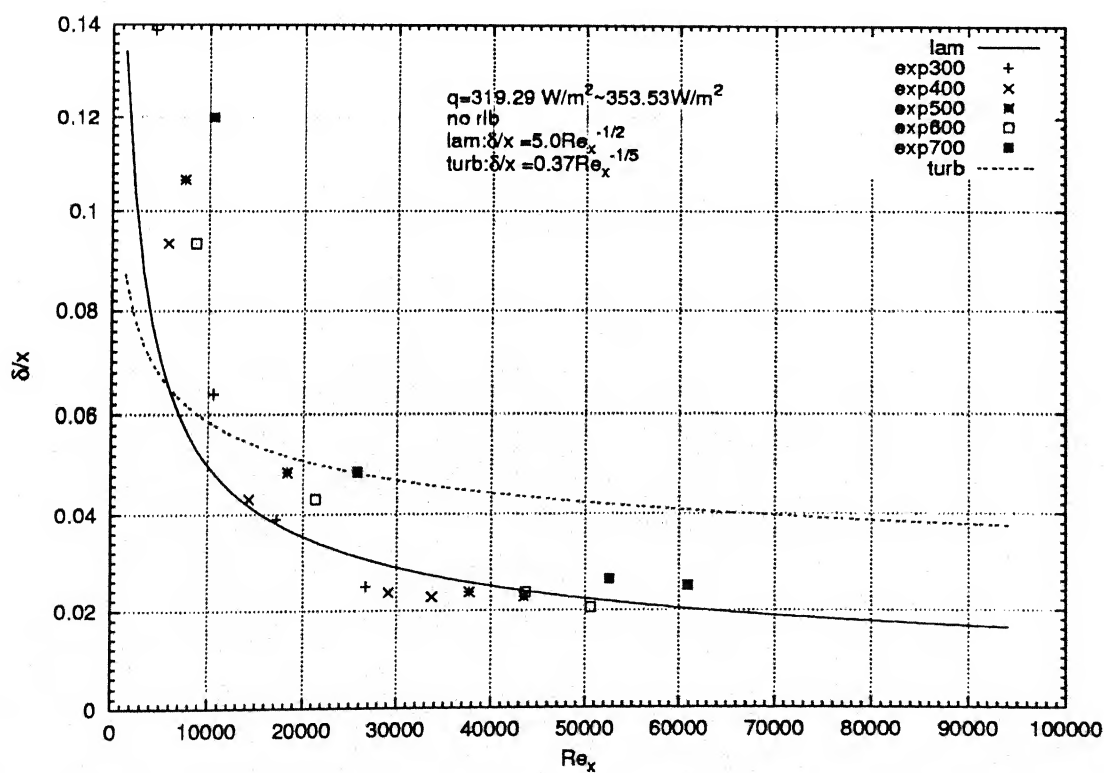


Figure 4.4: Variation of the hydrodynamic boundary-layer thickness for flow over a flat surface

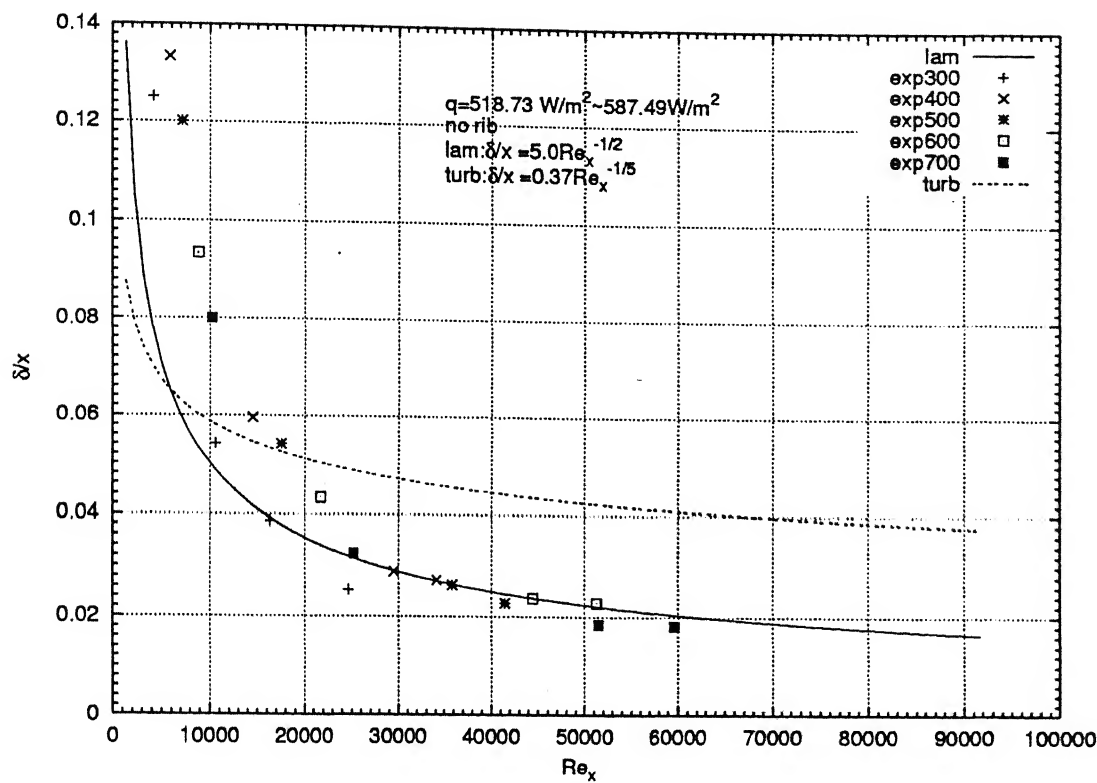


Figure 4.5: Variation of the hydrodynamic boundary-layer thickness for flow over a flat surface

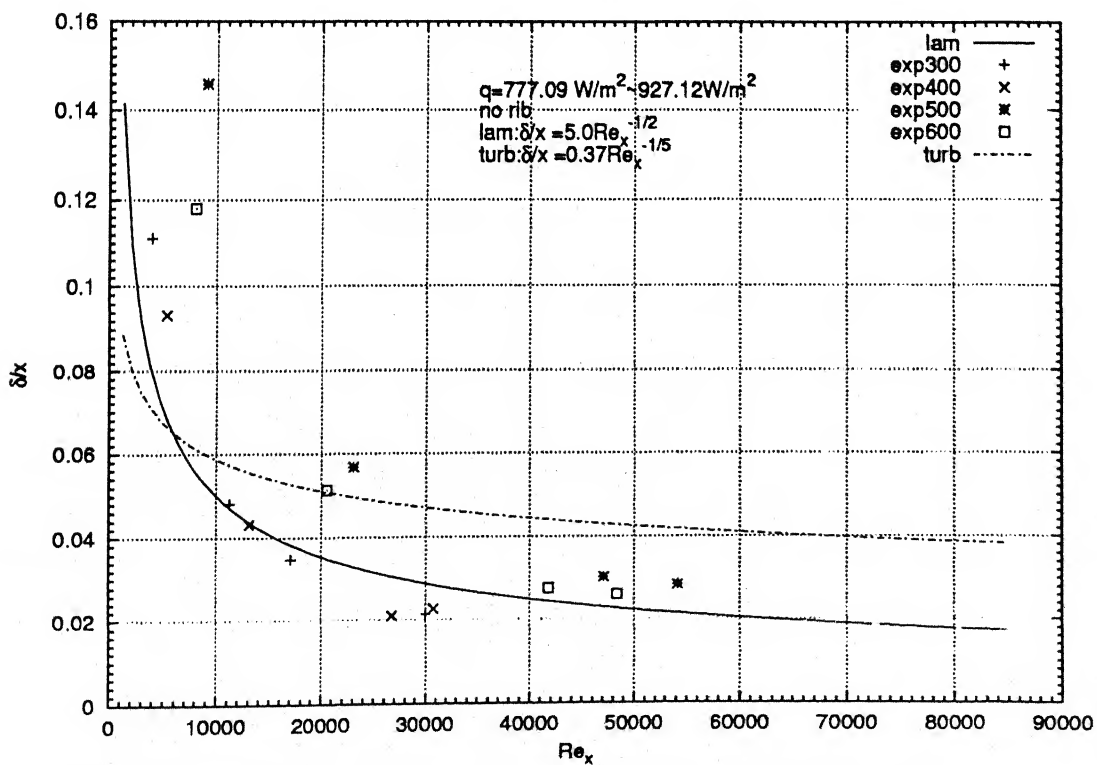


Figure 4.6: Variation of the hydrodynamic boundary-layer thickness for flow over a flat surface

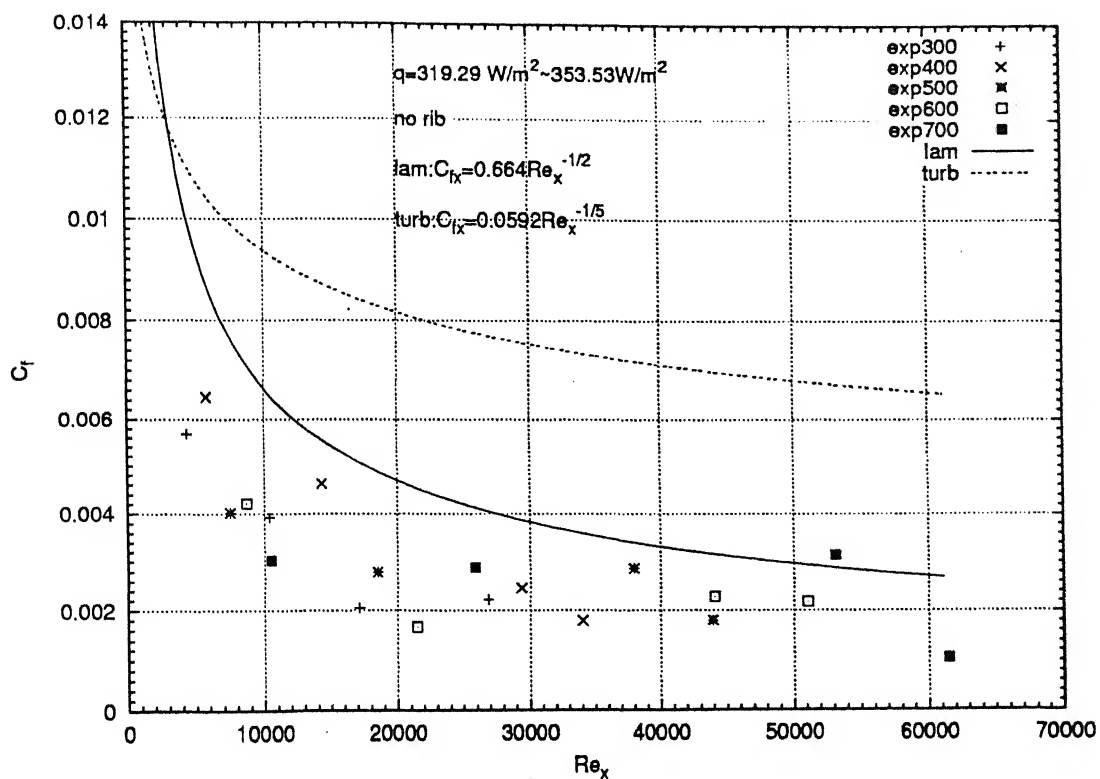


Figure 4.7: Skin friction coefficient as a function of Reynolds number for a flat surface

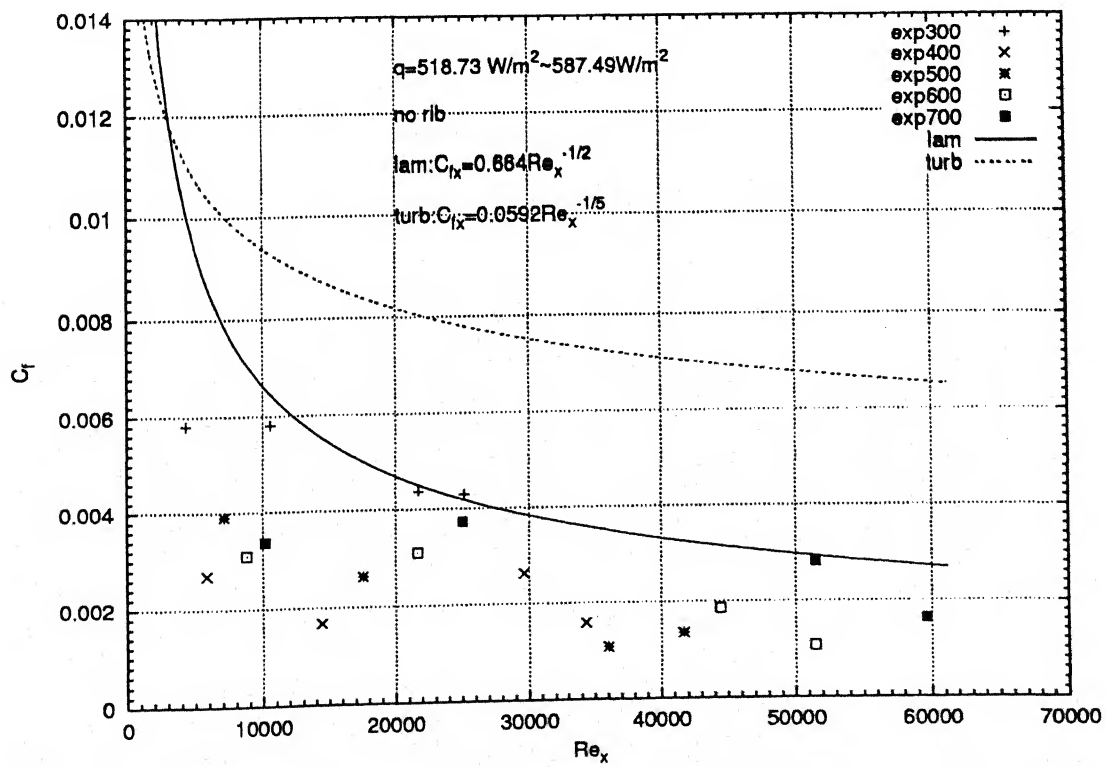


Figure 4.8: Skin friction coefficient as a function of Reynolds number for a flat surface

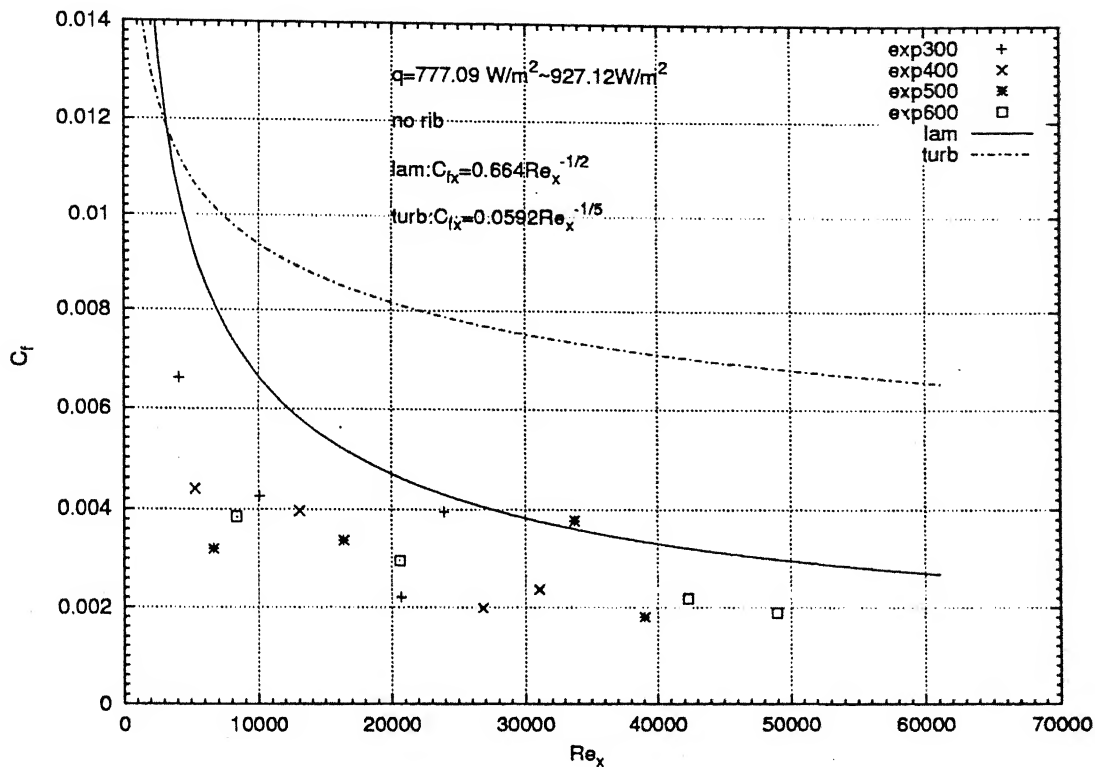


Figure 4.9: Skin friction coefficient as a function of Reynolds number for a flat surface

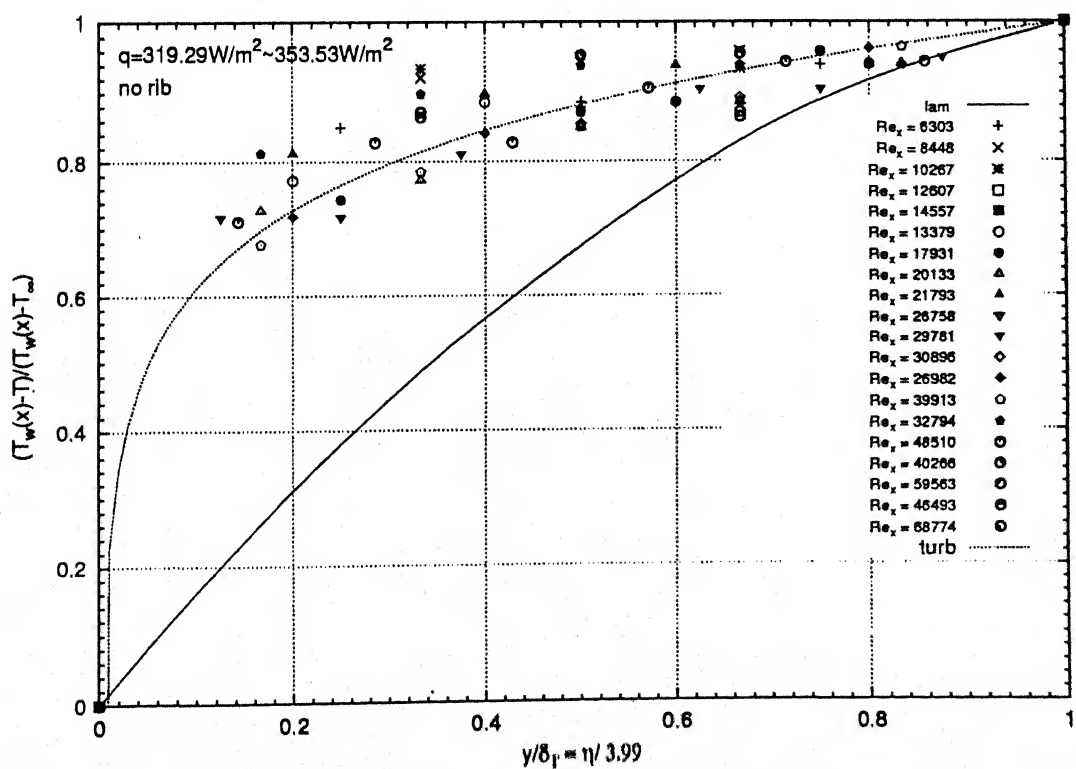


Figure 4.10: Temperature profiles in flow over a flat surface

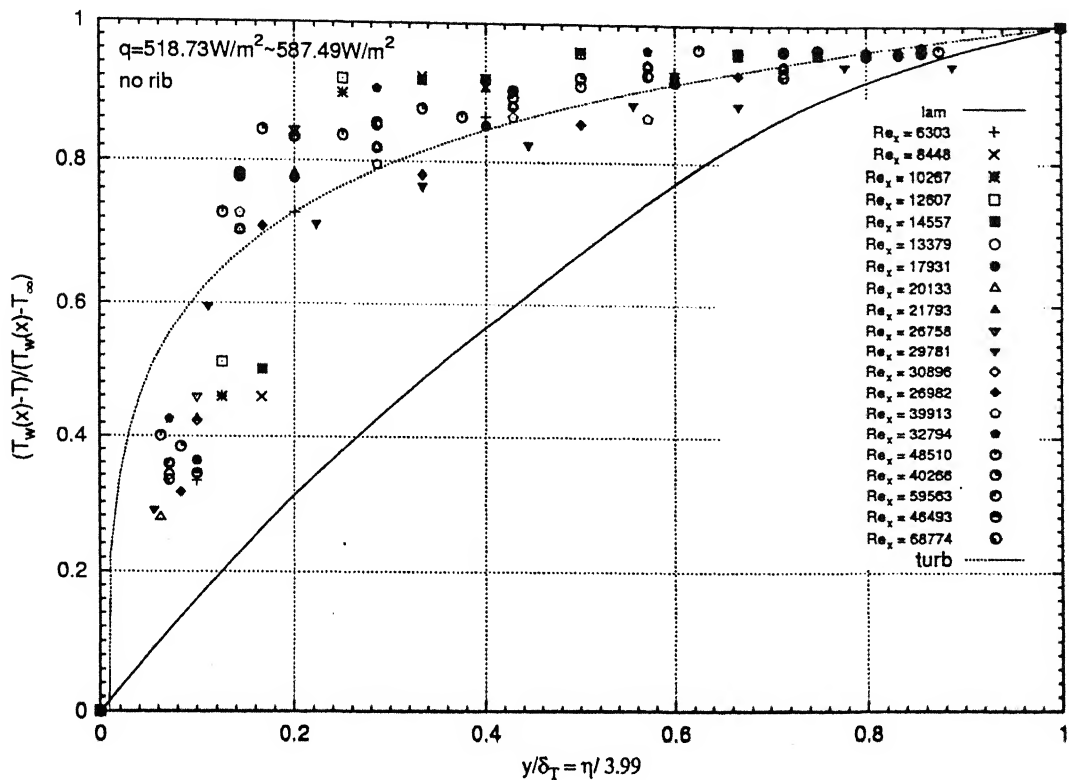


Figure 4.11: Temperature profiles in flow over a flat surface

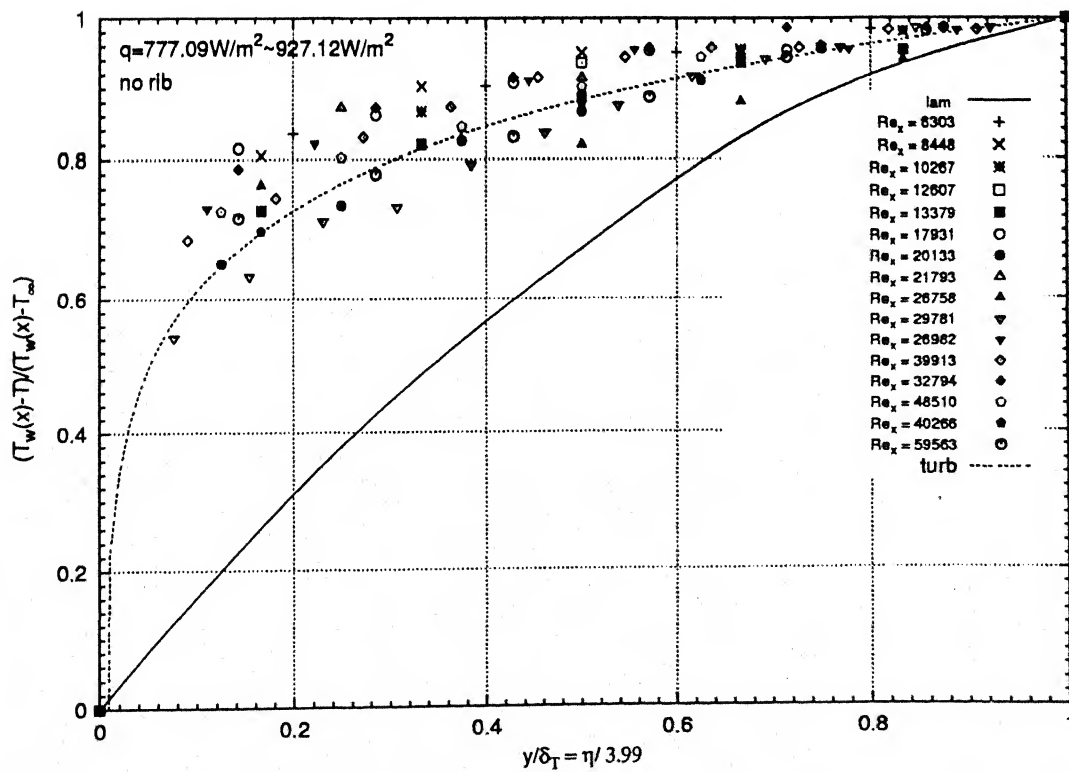


Figure 4.12: Temperature profiles in flow over a flat surface

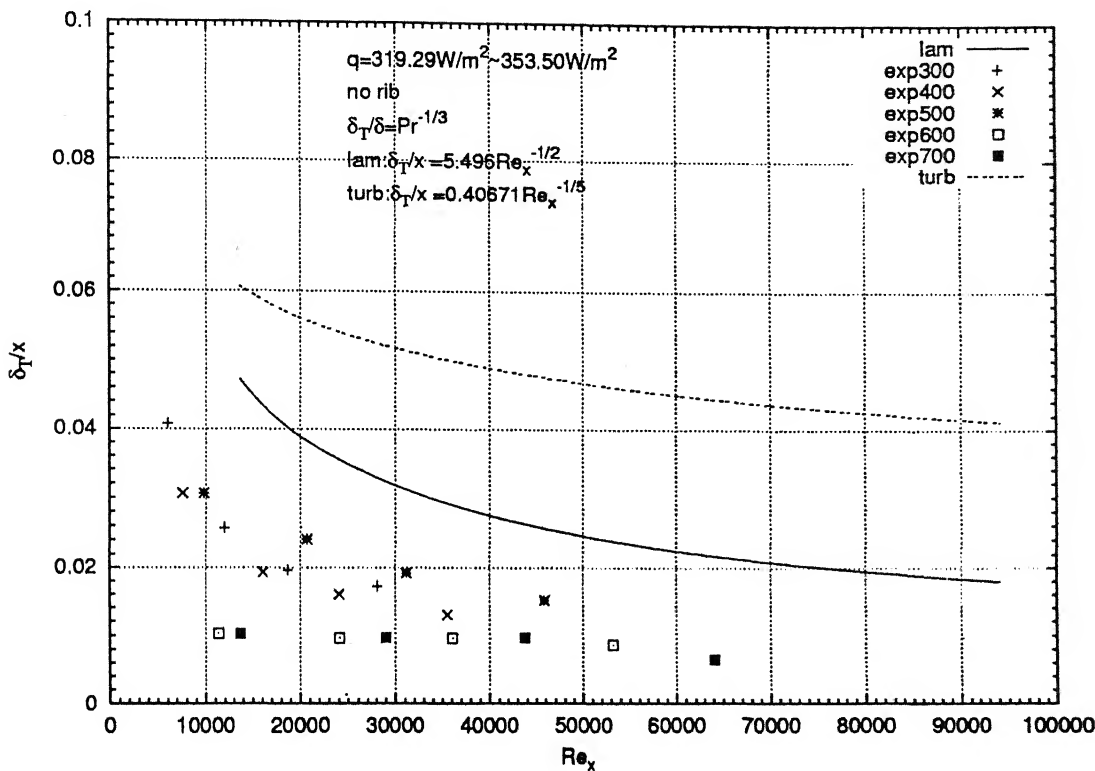


Figure 4.13: Variation of the thermal boundary-layer thickness for flow over a flat surface

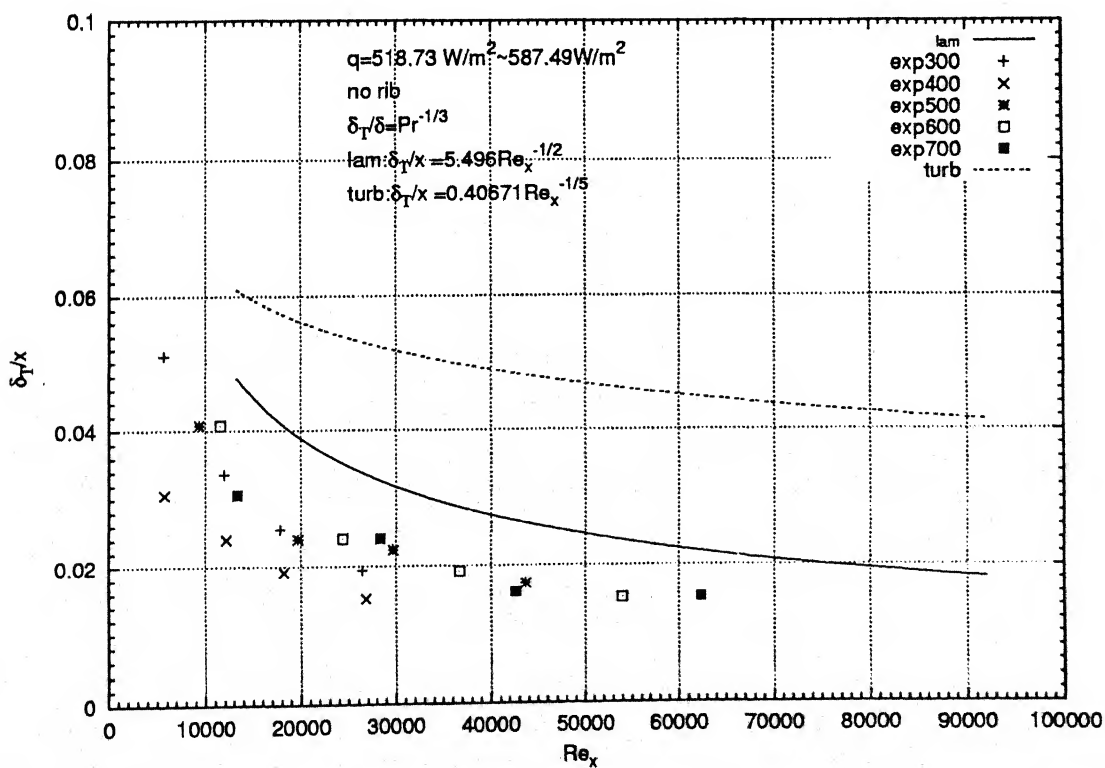


Figure 4.14: Variation of the thermal boundary-layer thickness for flow over a flat surface

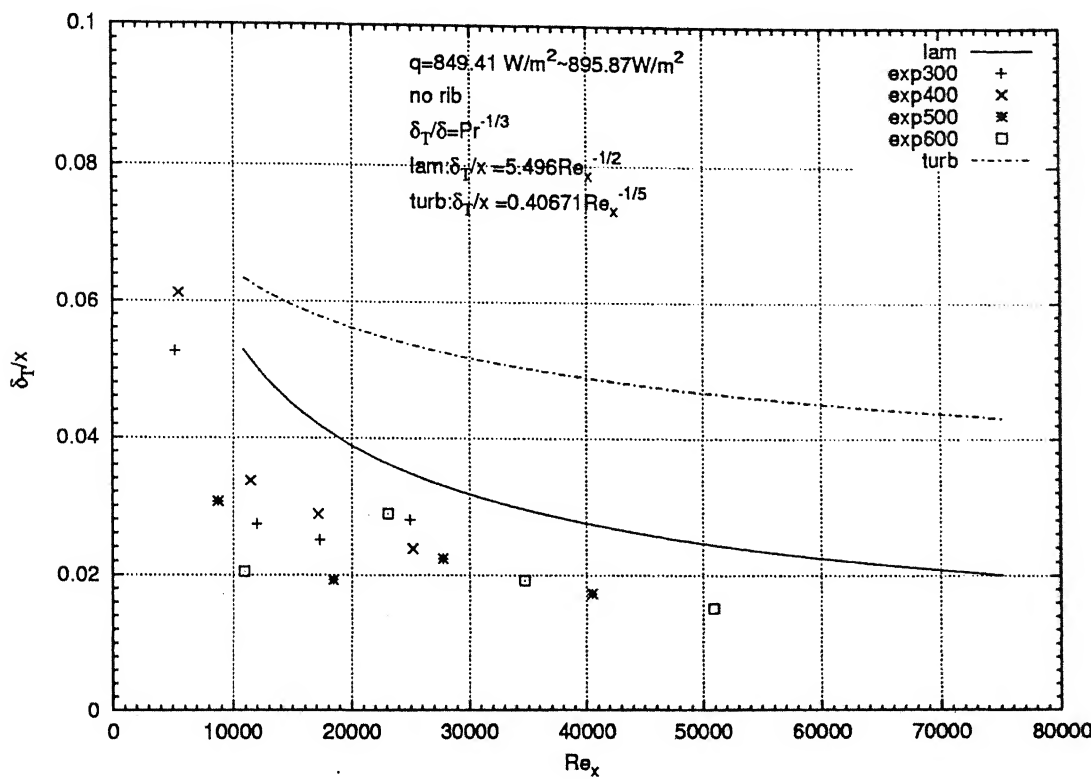


Figure 4.15: Variation of the thermal boundary-layer thickness for flow over a flat surface

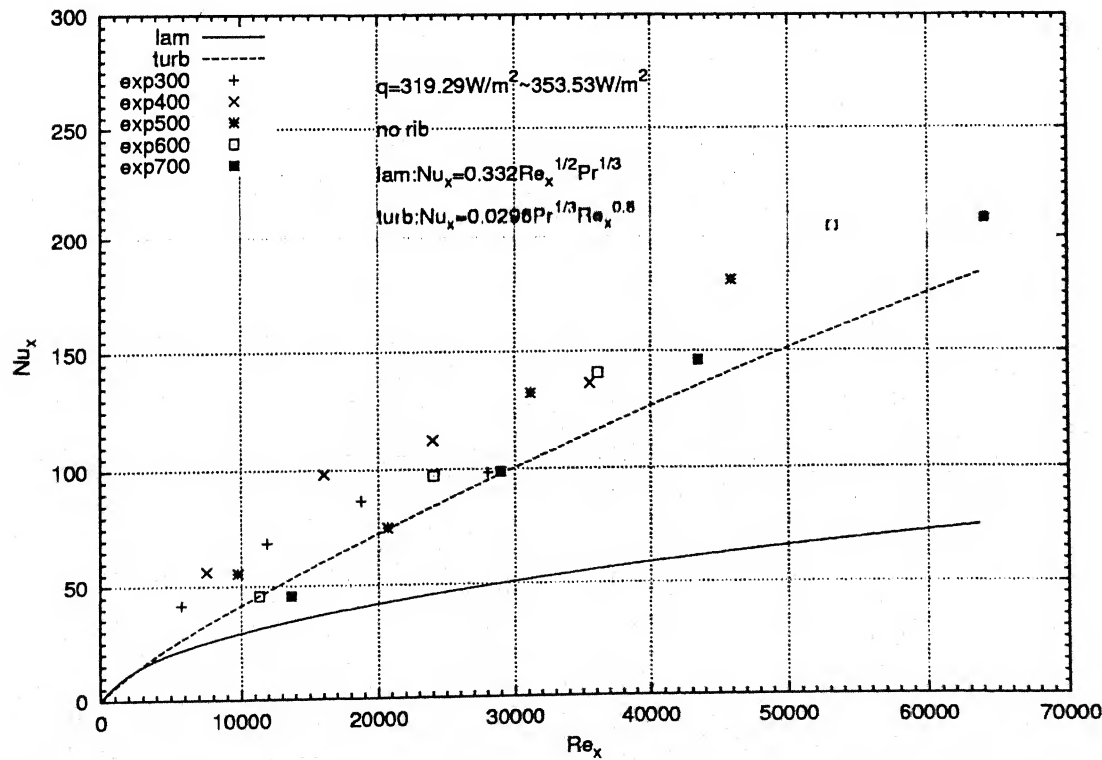


Figure 4.16: Local Nusselt number variation with Reynolds number for flow over a flat surface

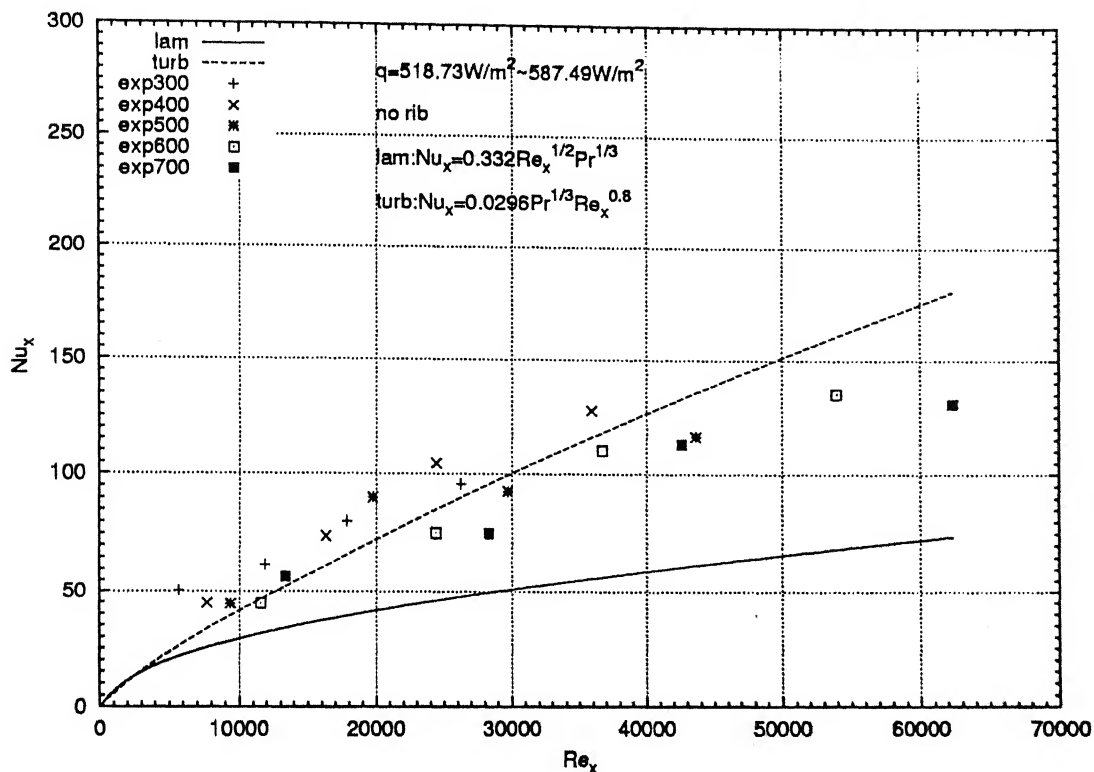


Figure 4.17: Local Nusselt number variation with Reynolds number for flow over a flat surface

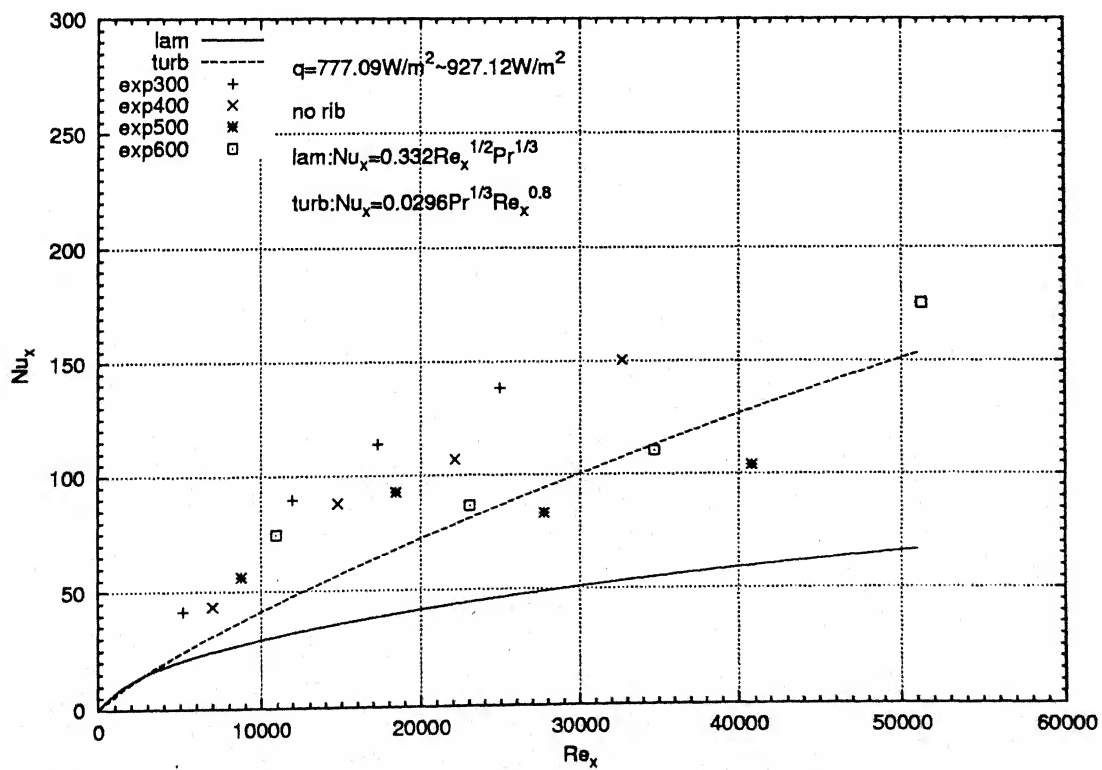


Figure 4.18: Local Nusselt number variation with Reynolds number for flow over a flat surface

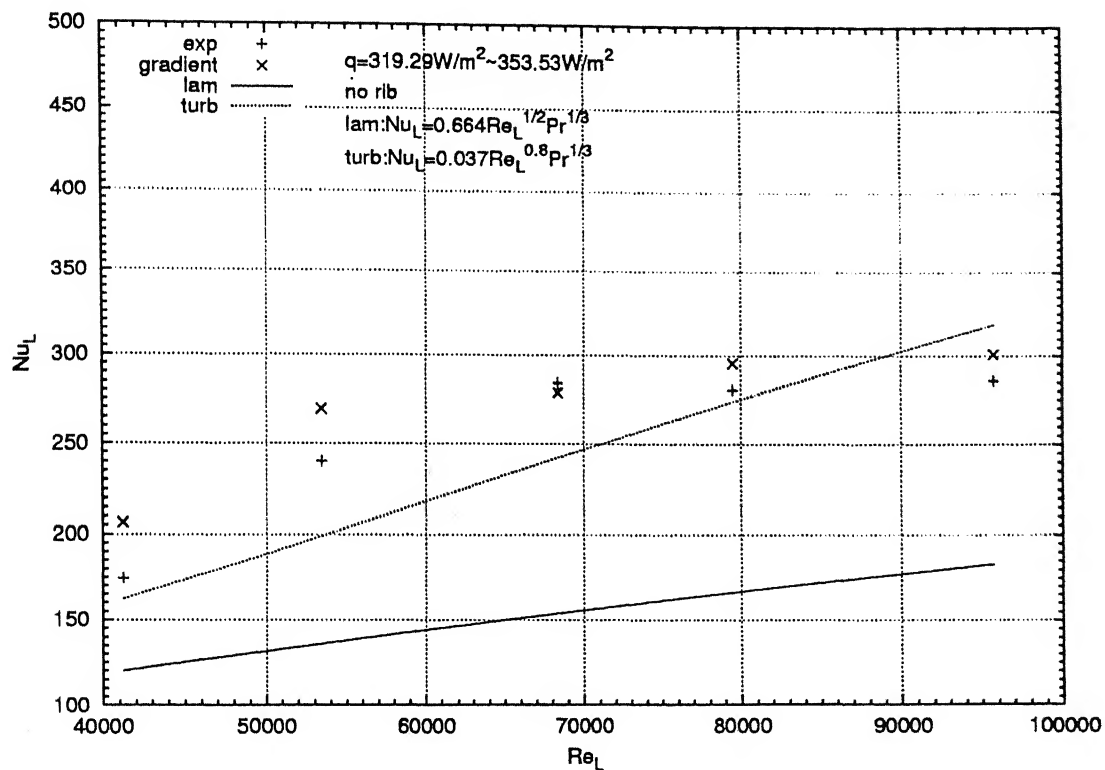


Figure 4.19: Average Nusselt number variation with Reynolds number for a flow over a flat surface

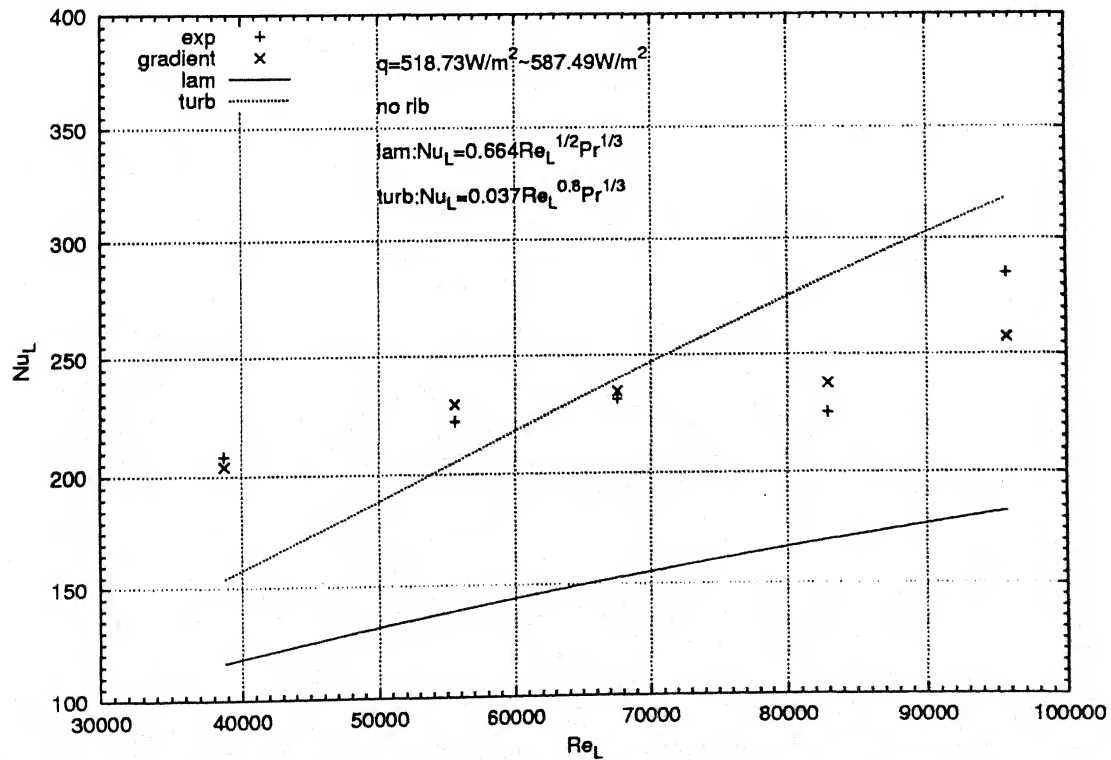


Figure 4.20: Average Nusselt number variation with Reynolds number for a flow over a flat surface

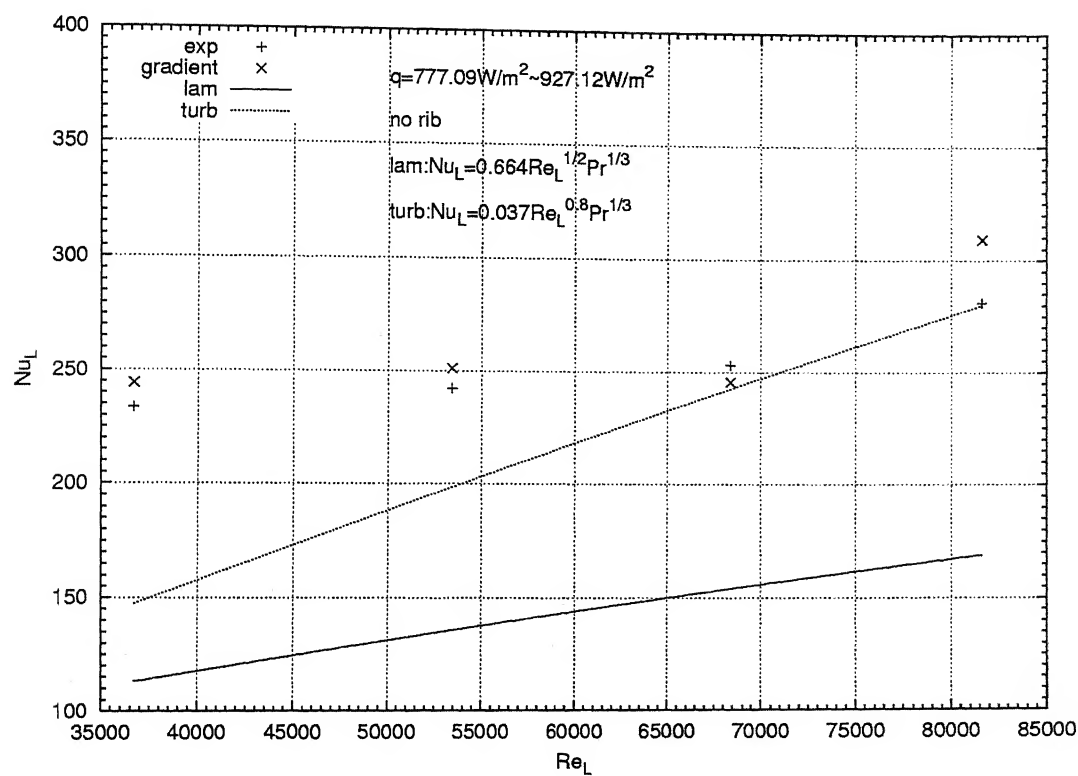


Figure 4.21: Average Nusselt number variation with Reynolds number for a flow over a flat surface

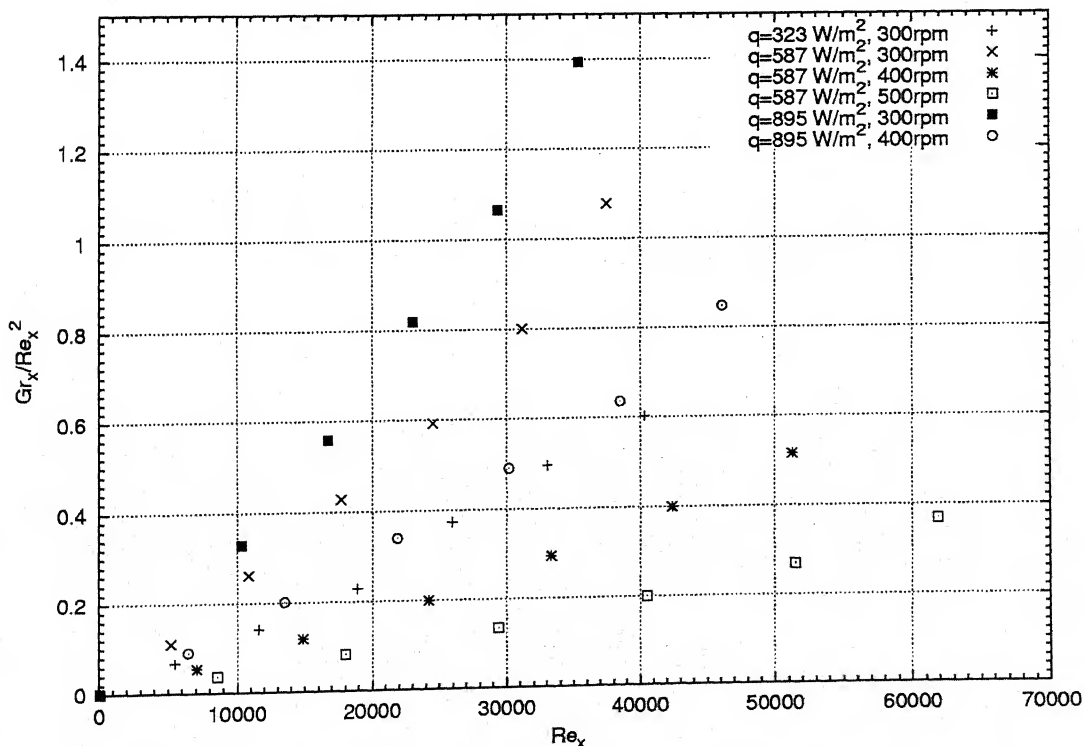


Figure 4.21(a): Variation of the Buoyancy parameter Gr/Re_x^2 with the local Reynolds number Re_x for various Heating Levels

turbulent profile, despite the time-averaged velocity profile being close to laminar. Figures 4.13, 4.14 and 4.15 show a plot between the dimensionless thermal boundary-layer thickness and the local Reynolds number. These figures show thermal boundary layer thickness is not large and falls within laminar region. The thermal boundary layer thickness is seen to be higher for a higher heating power. The measured data for δ_T follows the same trend as the laminar correlation. The plot between the local Nusselt number and the local Reynolds number is shown in Figures 4.16, 4.17 and 4.18. There is a good agreement between the measured data and turbulent correlation. This is understandable because the Nusselt number follows closely the local temperature profile. At a higher heating level and a higher Reynolds number there is a deviation between measured data and the turbulent correlation. The plot between average Nusselt number and Reynolds number is shown in Figures 4.19, 4.20 and 4.21. The average Nusselt number is also seen to fall in the turbulent region. The average Nusselt number exceeds the turbulent value at a high power input and a low Reynolds number, probably due to buoyancy effects as well as large variation in the fluid properties. The average Nusselt number determined by the gradient method and that based on the power input match with each other.

4.2 Flow over a Ribbed flat surface with Heat Transfer

The experiments have been performed in the test facility carrying a heated surface with a rib. The power supplied to the aluminium plate in the three experiments are:

1. 296-323 $\frac{\text{W}}{\text{m}^2}$
2. 614-628 $\frac{\text{W}}{\text{m}^2}$
3. 899-988 $\frac{\text{W}}{\text{m}^2}$

The free stream velocities produced in the test cell are:

1. 0.98 m/s

2. 1.60 m/s
3. 2.25 m/s

Velocity and temperature measurements are reported for locations beyond the rib.

4.2.1 Velocity Field

Figures 4.22, 4.23 and 4.24 show a plot between the dimensionless transverse coordinate y/δ and the dimensionless local velocity u/U_∞ drawn in order to analyze the flow character. As speed increases the flow becomes turbulent. Owing to the presence of rib flow separation and attachment occurs after the rib and makes the flow turbulent. Figures 4.25, 4.26 and 4.27 show that the boundary layer thickness is very high due to the obstruction of the rib to the flow. Therefore the boundary layer thickness rises up to 40 mm above the surface of the plate. Figures 4.28, 4.29 and 4.30 show that the skin friction coefficient does not vary systematically. The skin friction coefficient first increases with distance from the rib and then decreases at higher distances.

4.2.2 Thermal Field

Figures 4.31, 4.32 and 4.33 show temperature distribution in the fluid above the plate. Since the heat transfer is turbulent the measured data lies above the turbulent curve. The scatter of the measured data are very small at higher power supply. Figures 4.34, 4.35 and 4.36 show the relation between the non dimensional thermal boundary layer thickness and the Reynolds number. The graphs show at lower power supply the boundary layer thickness lies below the laminar region but at higher power supply the boundary layer thickness lies above the turbulent regime. Figures 4.37, 4.38 and 4.39 show the relation between the local Nusselt number and the local Reynolds number. The local Nusselt number continuously increases with an increase in the Reynolds number. All the measured value lies above the turbulent correlation curve. Figures 4.40, 4.41 and 4.42 show the relation between the average Nusselt number and the Reynolds number. The measured values once again lie above the turbulent correlation. The average

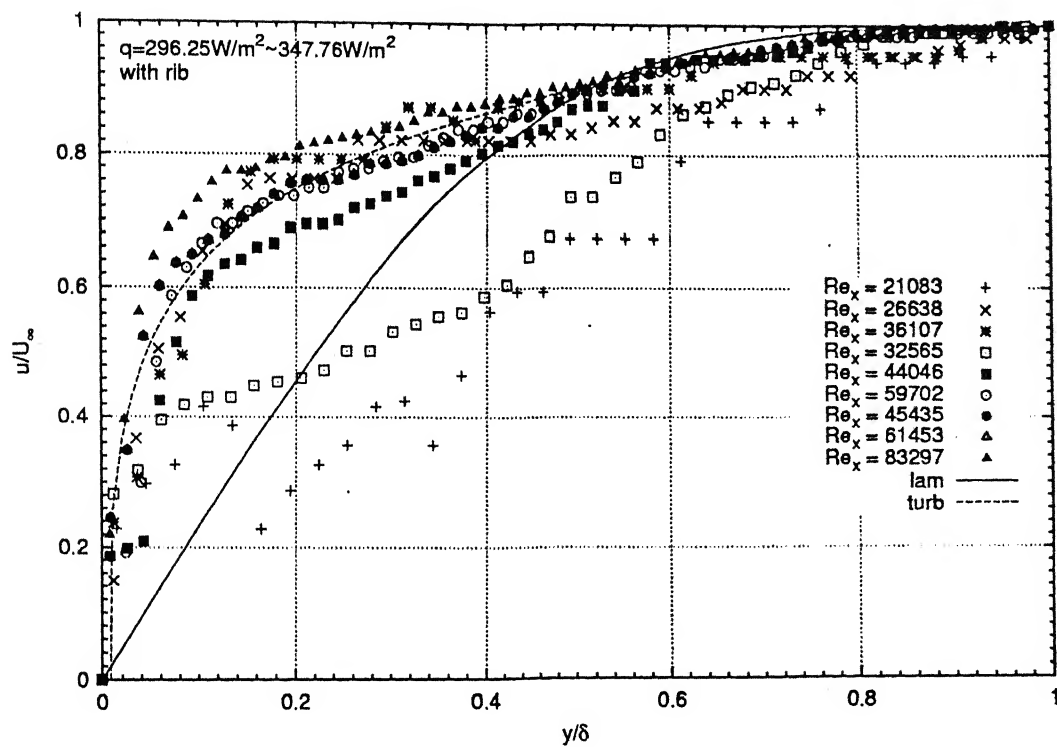


Figure 4.22: Velocity profiles in flow over a flat surface with a rib

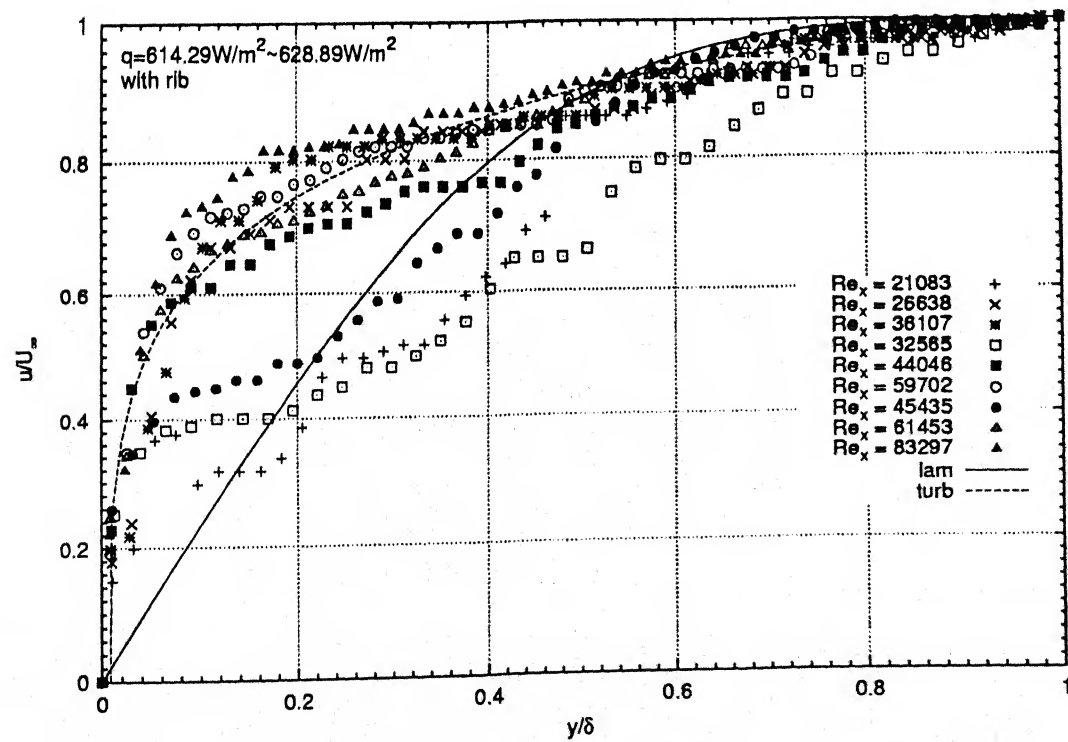


Figure 4.23: Velocity profiles in flow over a flat surface with a rib

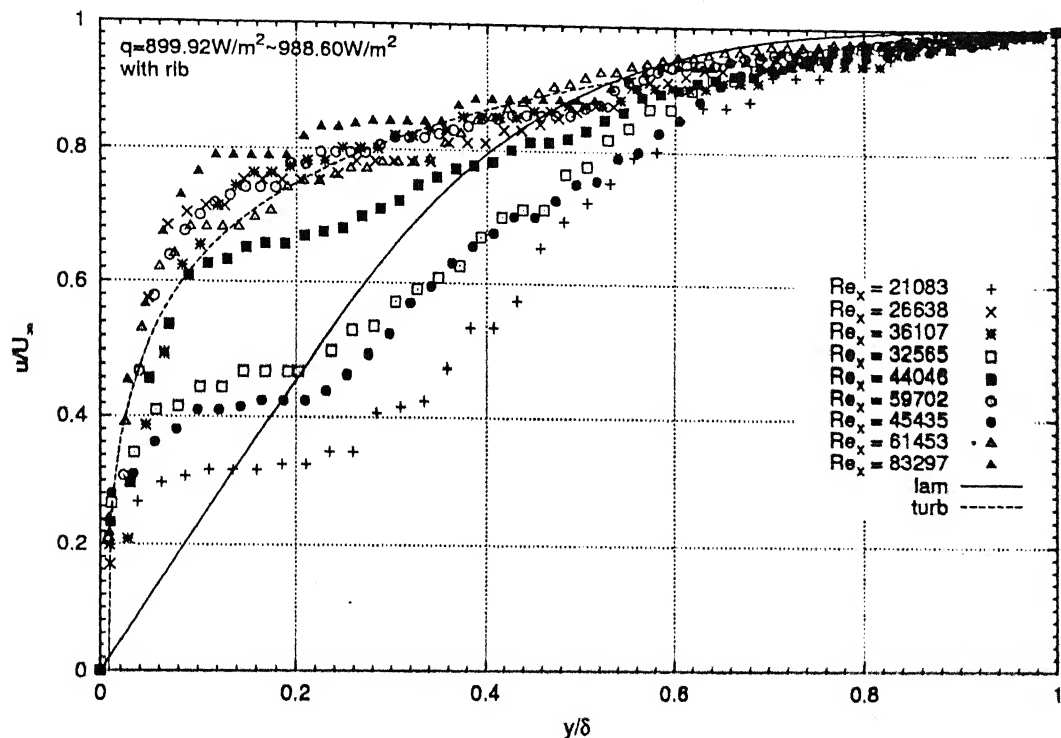


Figure 4.24: Velocity profiles in flow over a flat surface with a rib

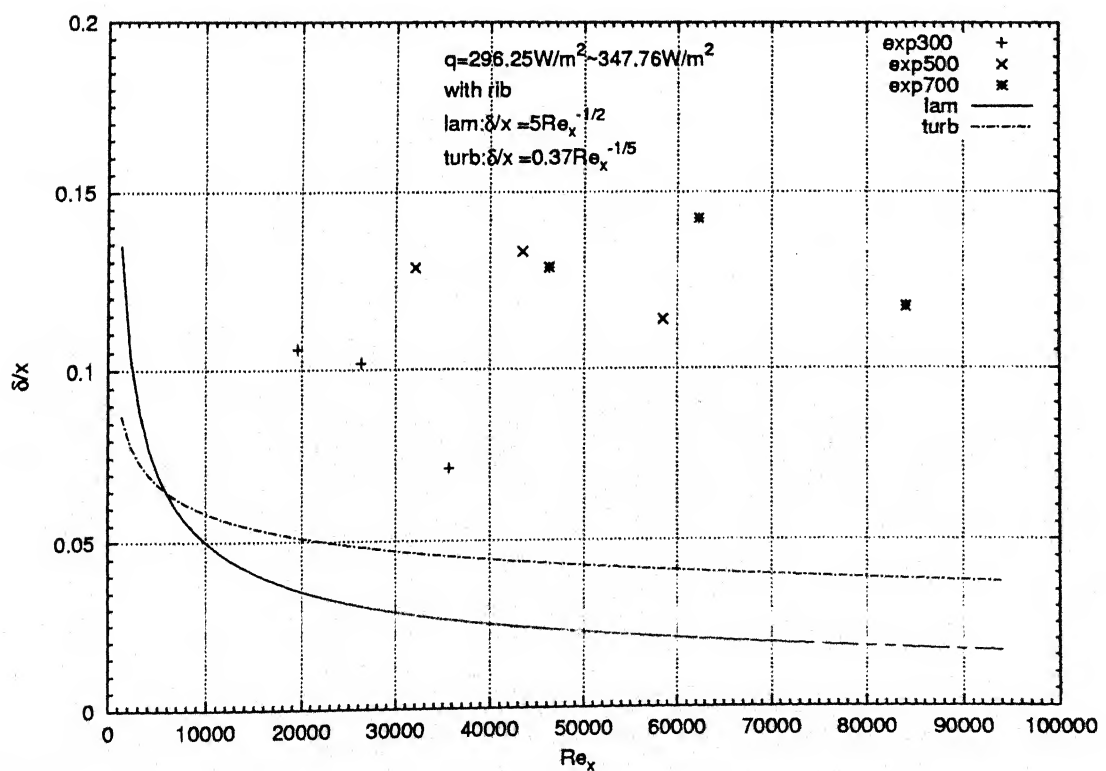


Figure 4.25: Variation of the hydrodynamic boundary-layer thickness for a flow over a flat surface with a rib

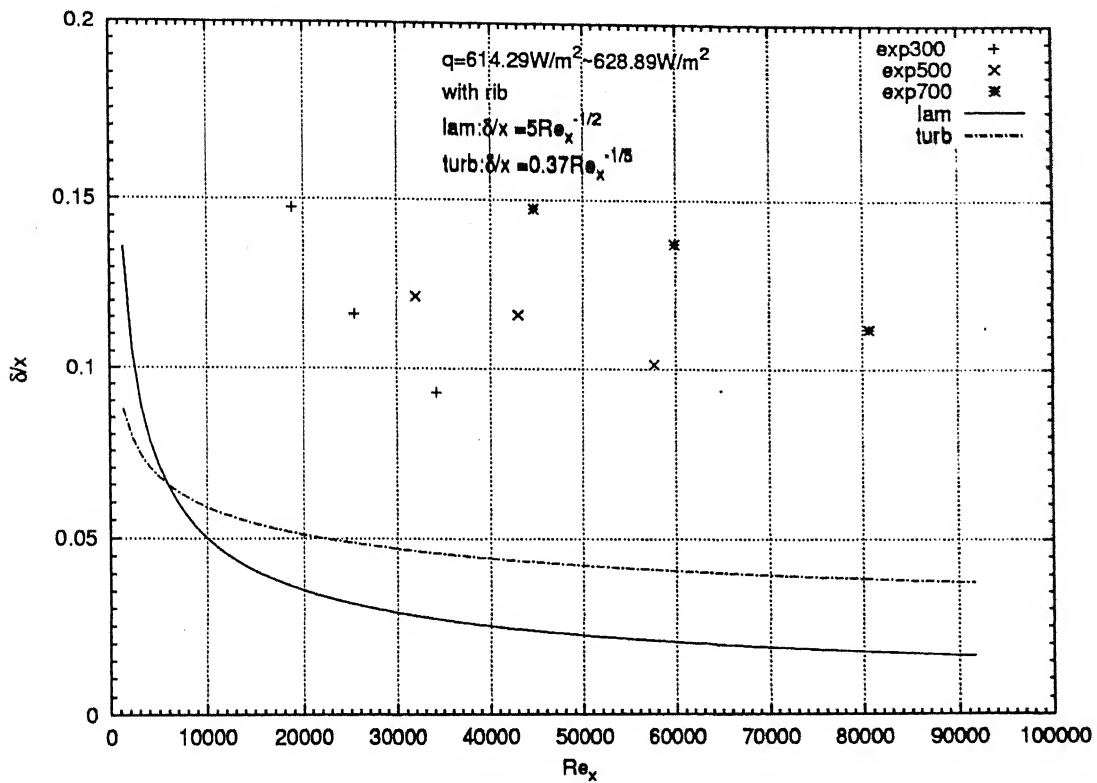


Figure 4.26: Variation of the hydrodynamic boundary-layer thickness for a flow over a flat surface with a rib

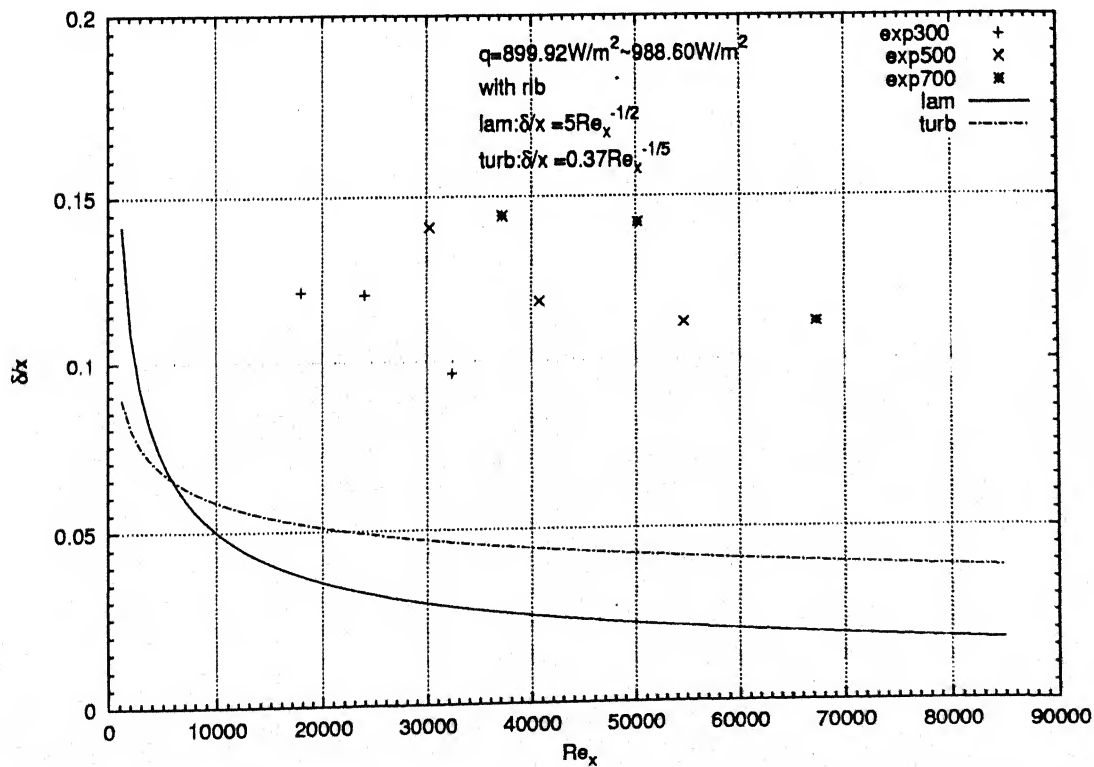


Figure 4.27: Variation of the hydrodynamic boundary-layer thickness for a flow over a flat surface with a rib

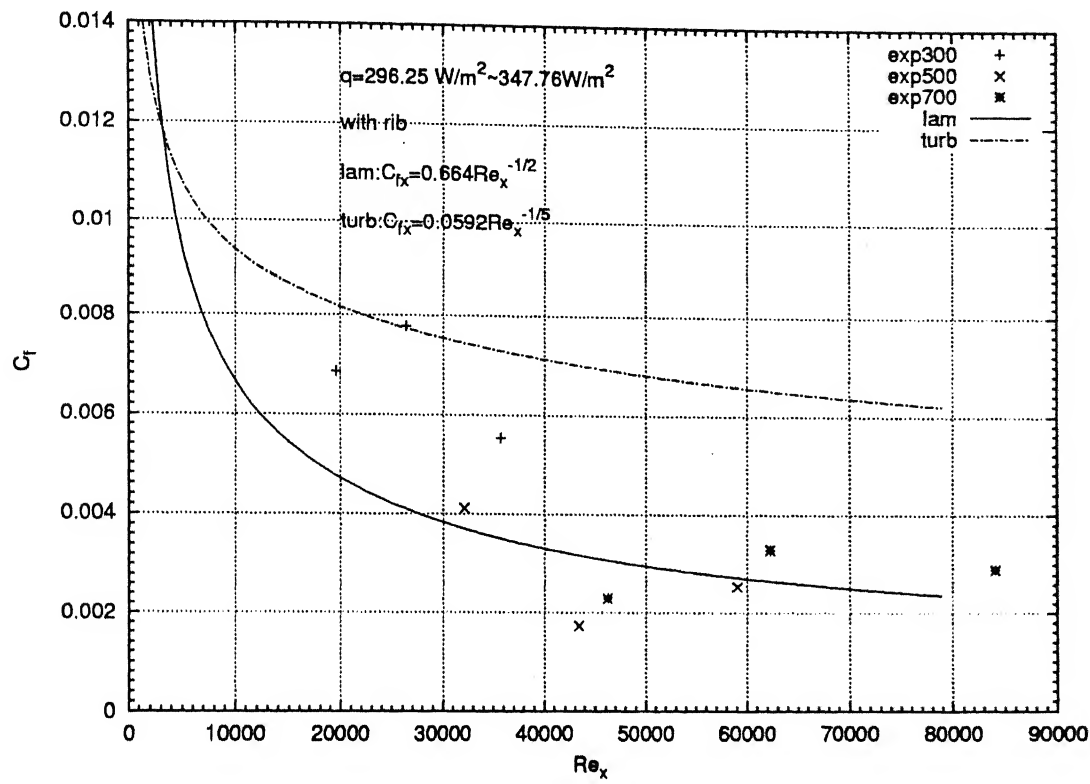


Figure 4.28: Skin friction coefficient as a function of Reynolds number for a flat surface with a rib

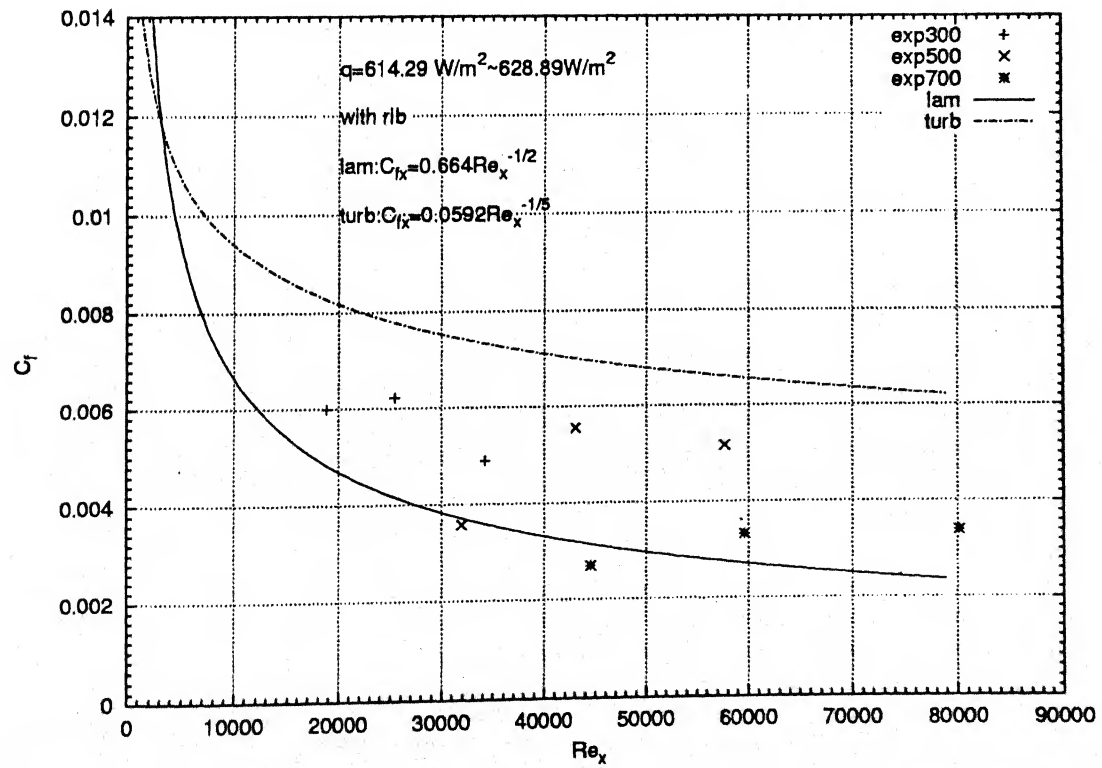


Figure 4.29: Skin friction coefficient as a function of Reynolds number for a flat surface with a rib

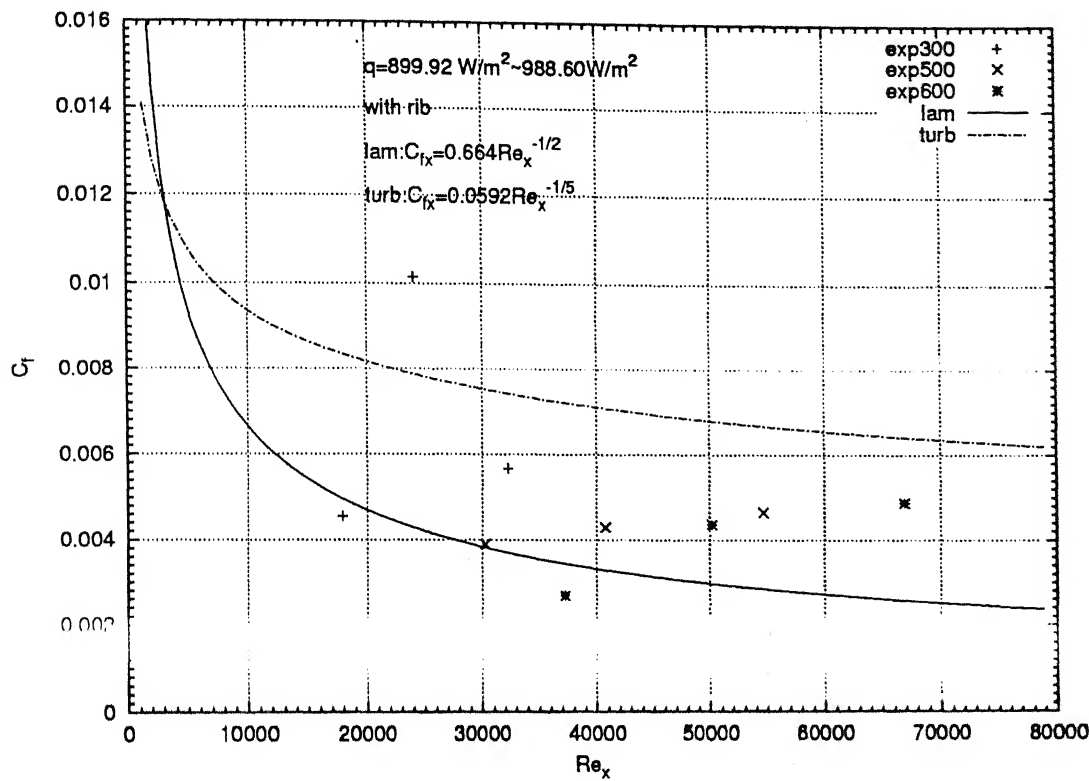


Figure 4.30: Skin friction coefficient as a function of Reynolds number for a flat surface with a rib

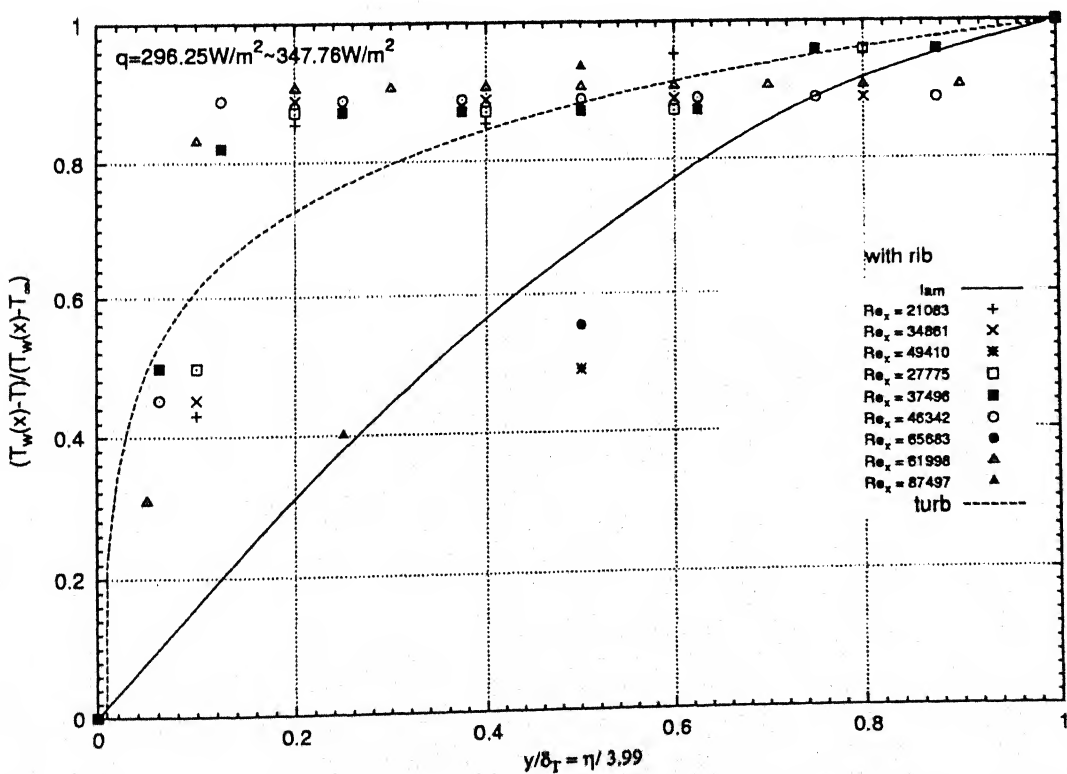


Figure 4.31: Temperature profiles in flow over a flat surface with a rib

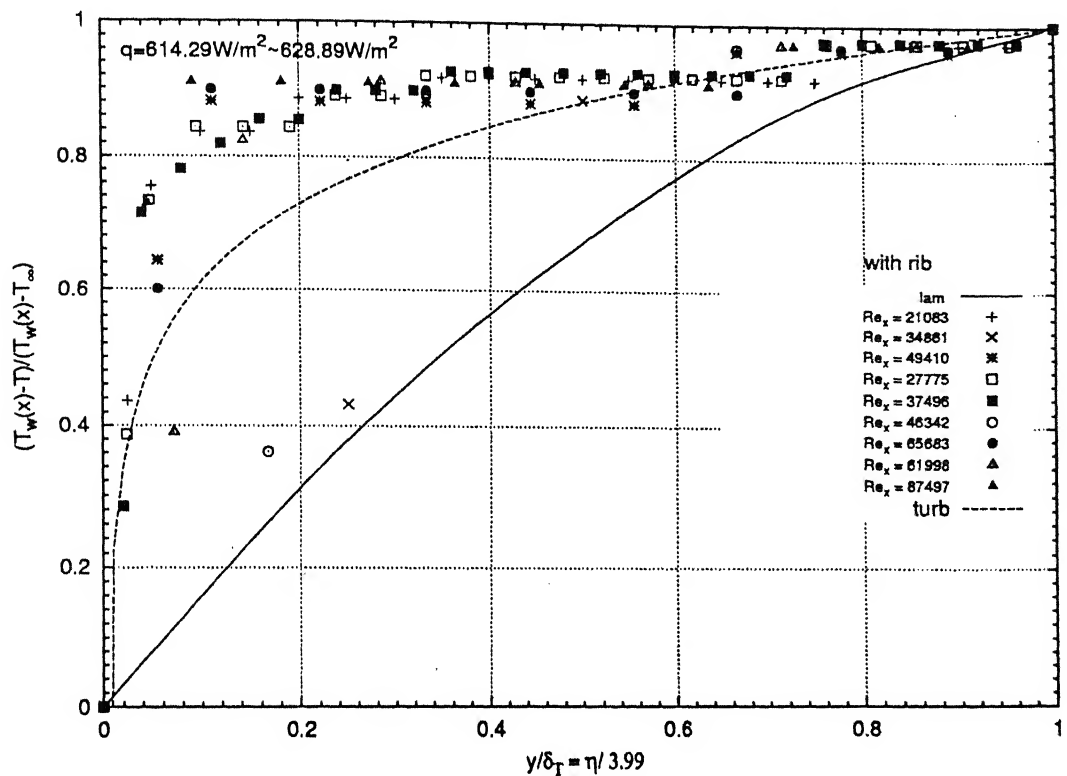


Figure 4.32: Temperature profiles in flow over a flat surface with a rib

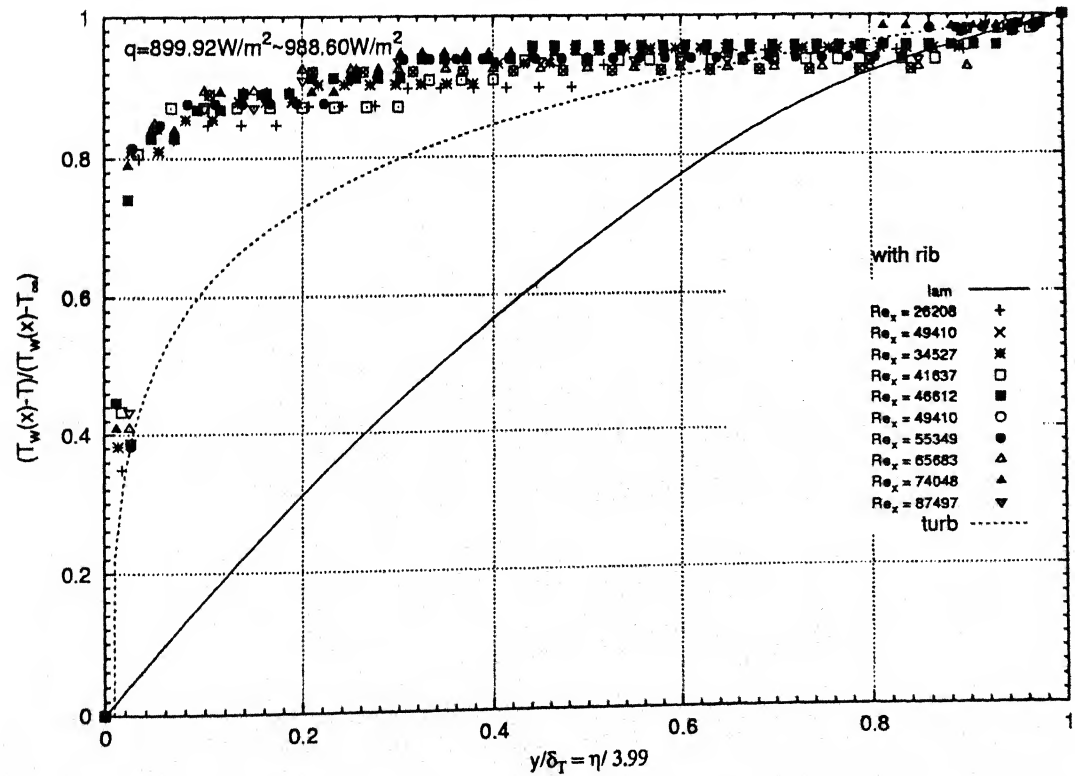


Figure 4.33: Temperature profiles in flow over a flat surface with a rib

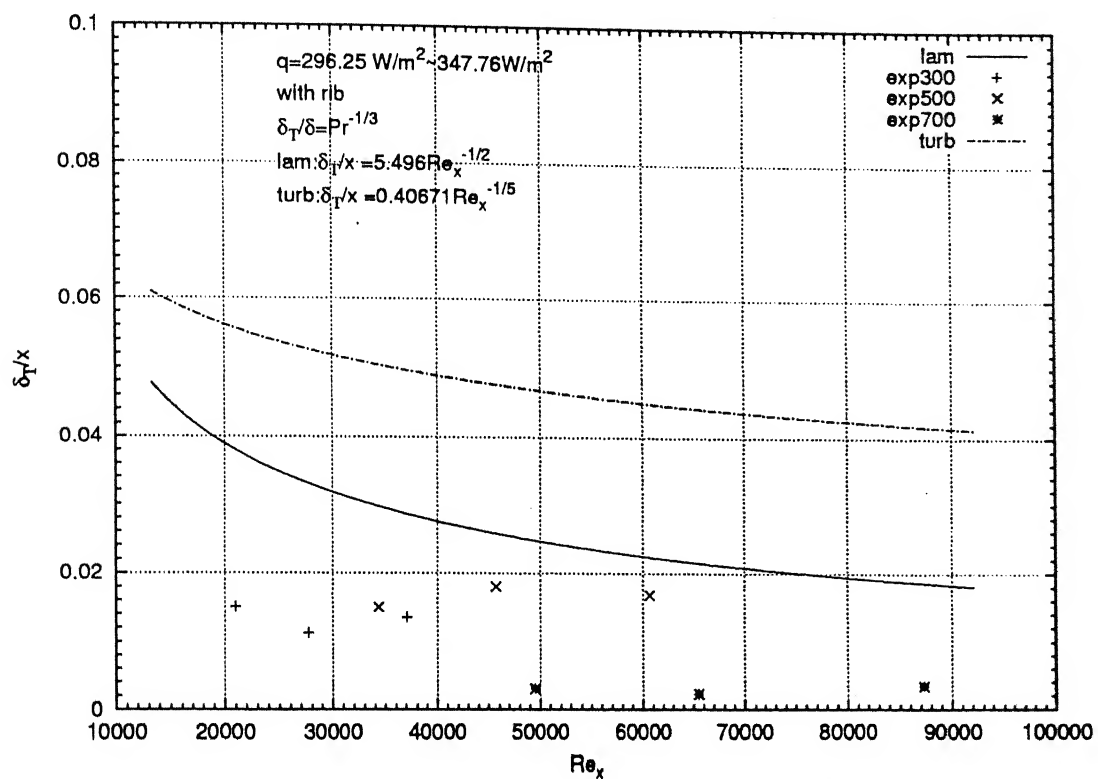


Figure 4.34: Variation of thermal boundary-layer thickness for flow over a flat surface with a rib

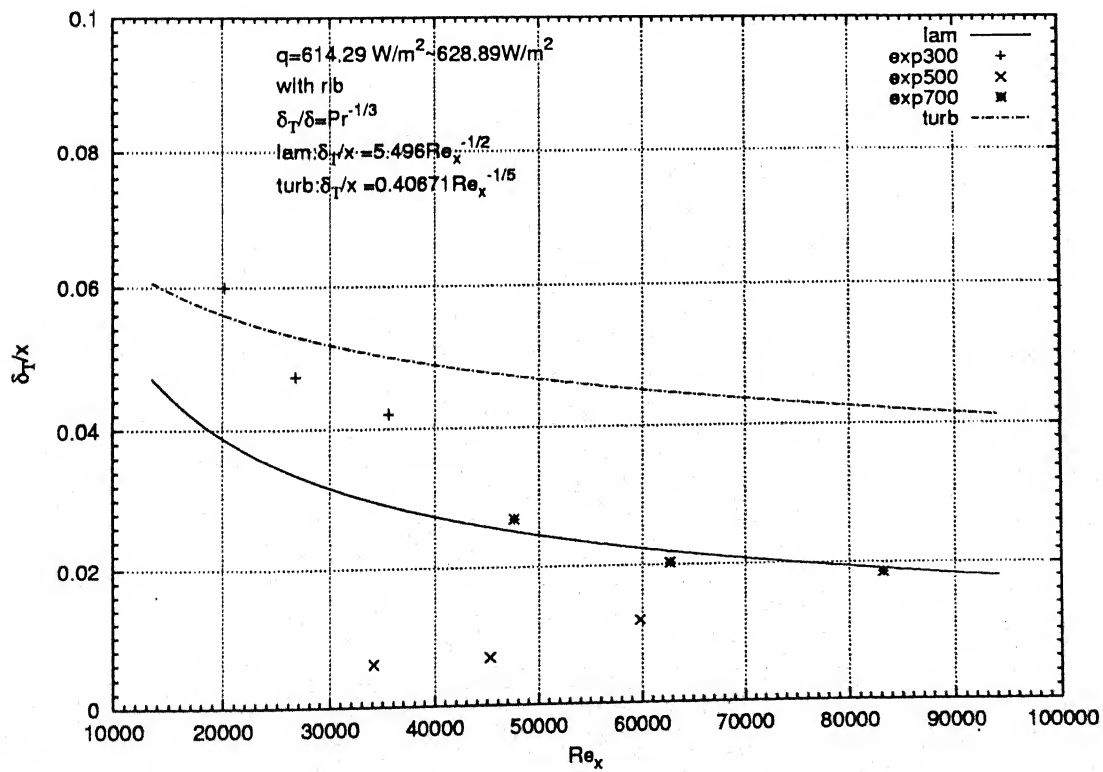


Figure 4.35: Variation of thermal boundary-layer thickness for flow over a flat surface with a rib

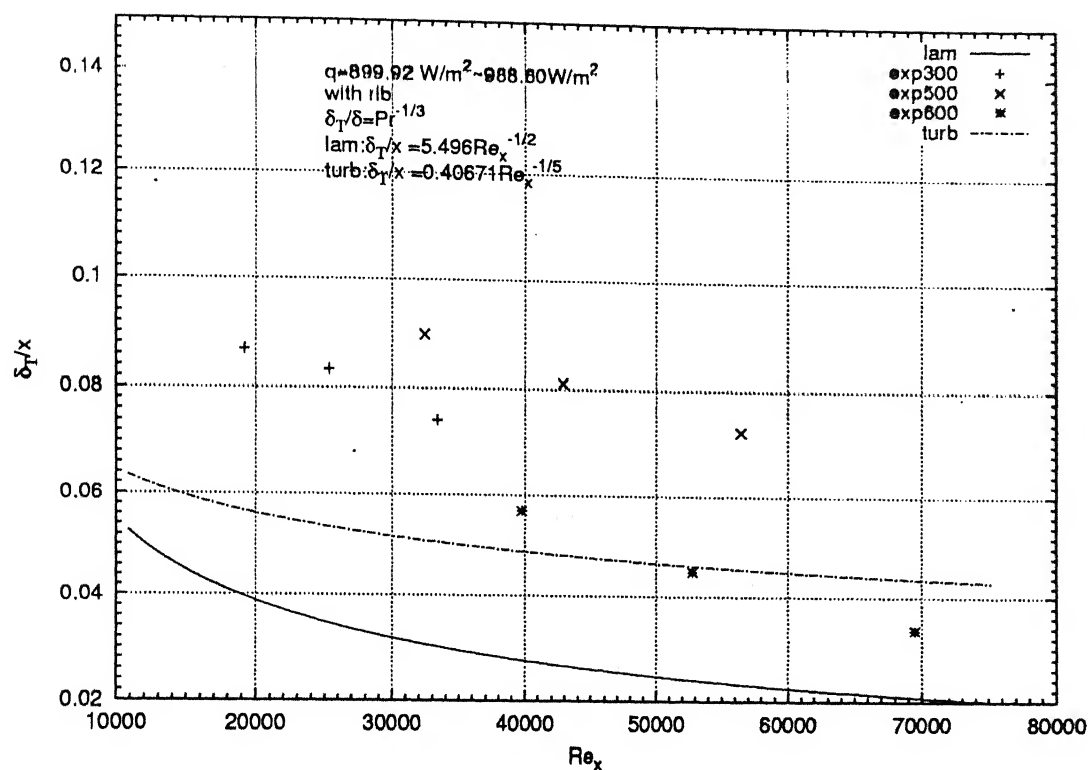


Figure 4.36: Variation of thermal boundary-layer thickness for flow over a flat surface with a rib

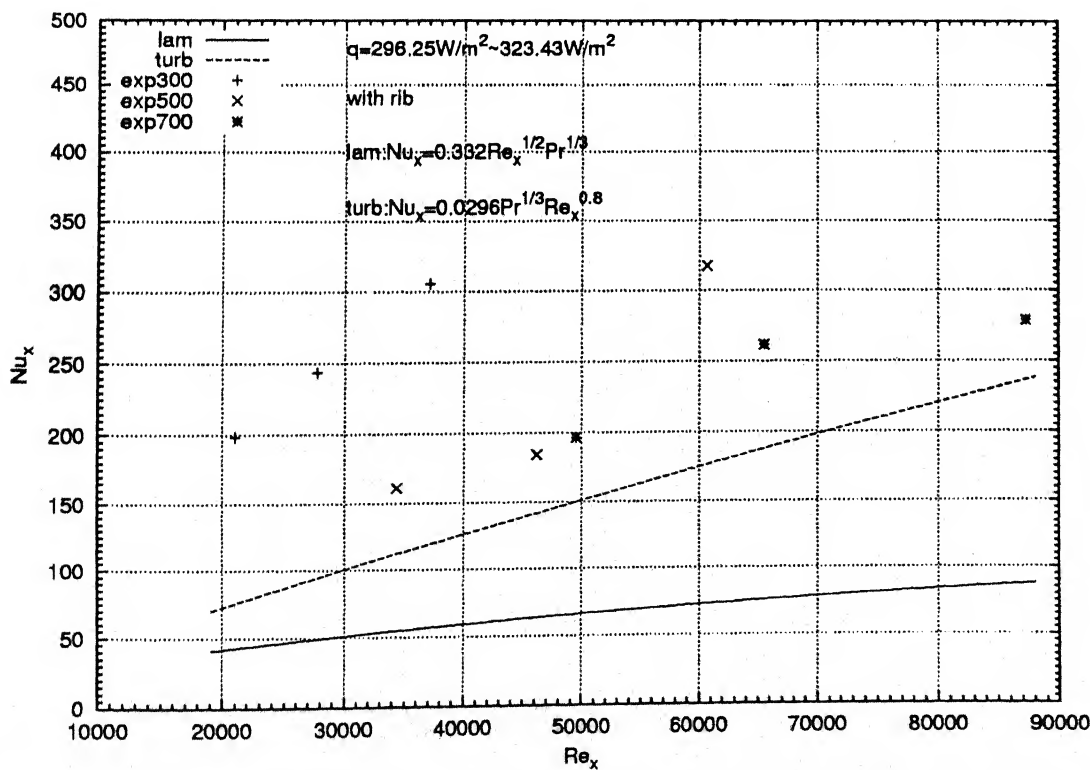


Figure 4.37: Local Nusselt number variation with Reynolds number for a flow over a flat surface with a rib

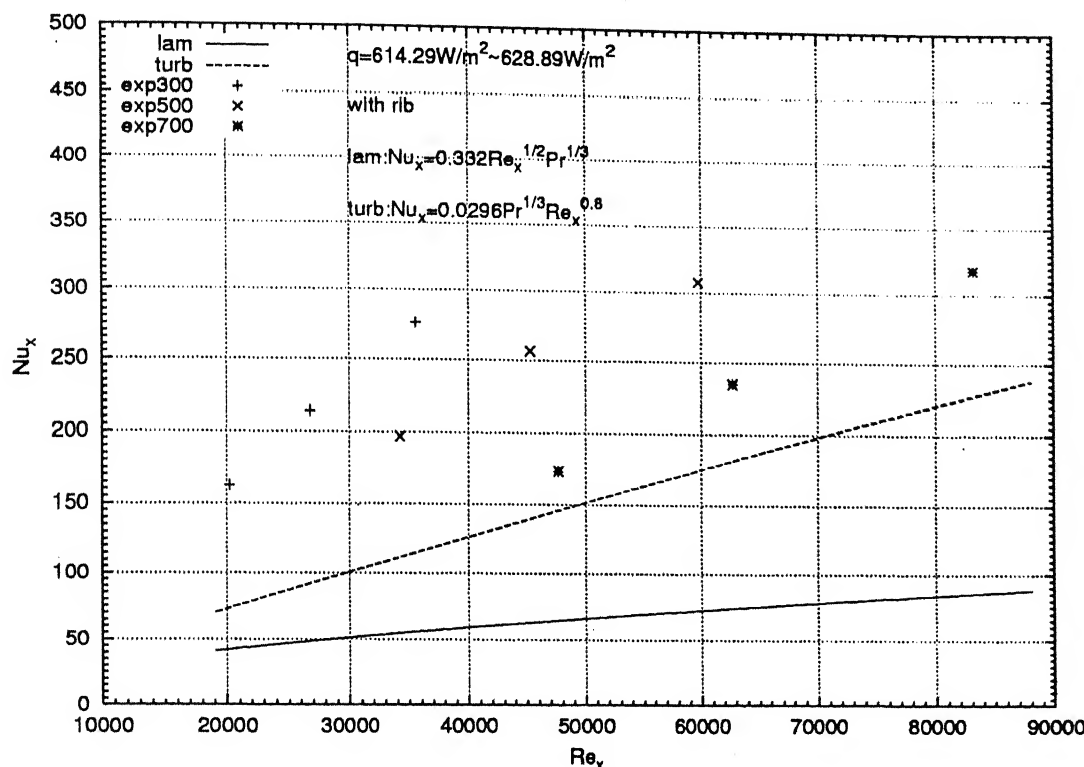


Figure 4.38: Local Nusselt number variation with Reynolds number for a flow over a flat surface with a rib

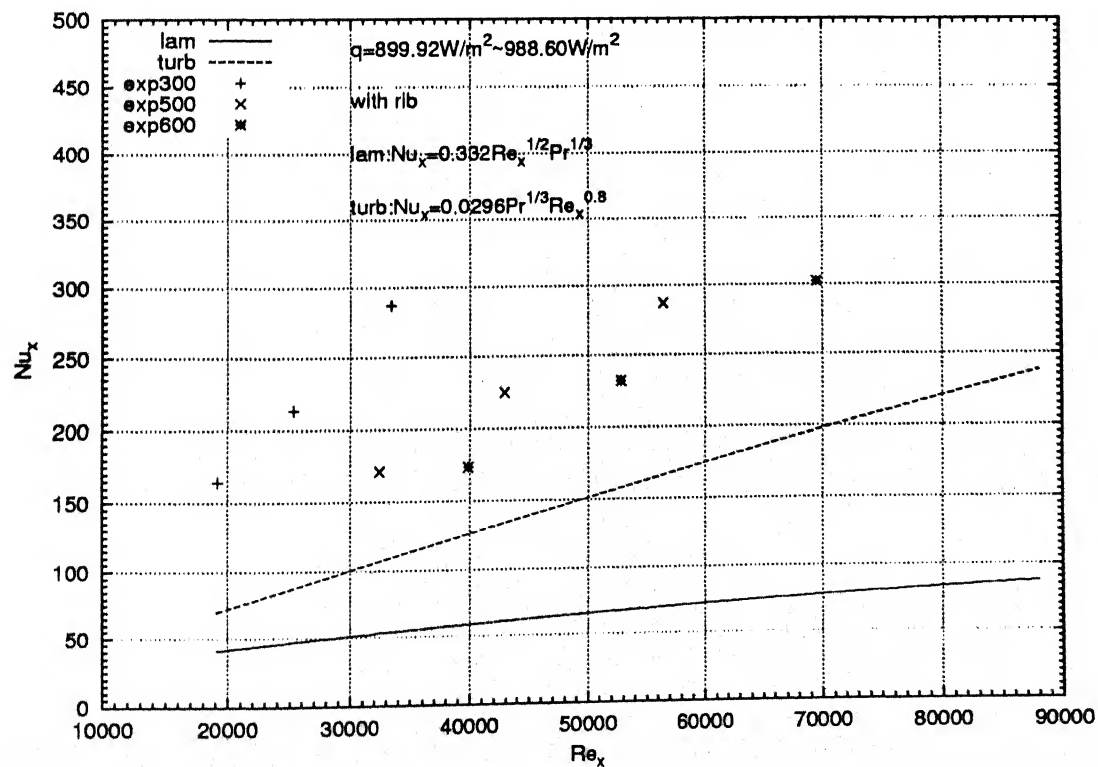


Figure 4.39: Local Nusselt number variation with Reynolds number for a flow over a flat surface with a rib

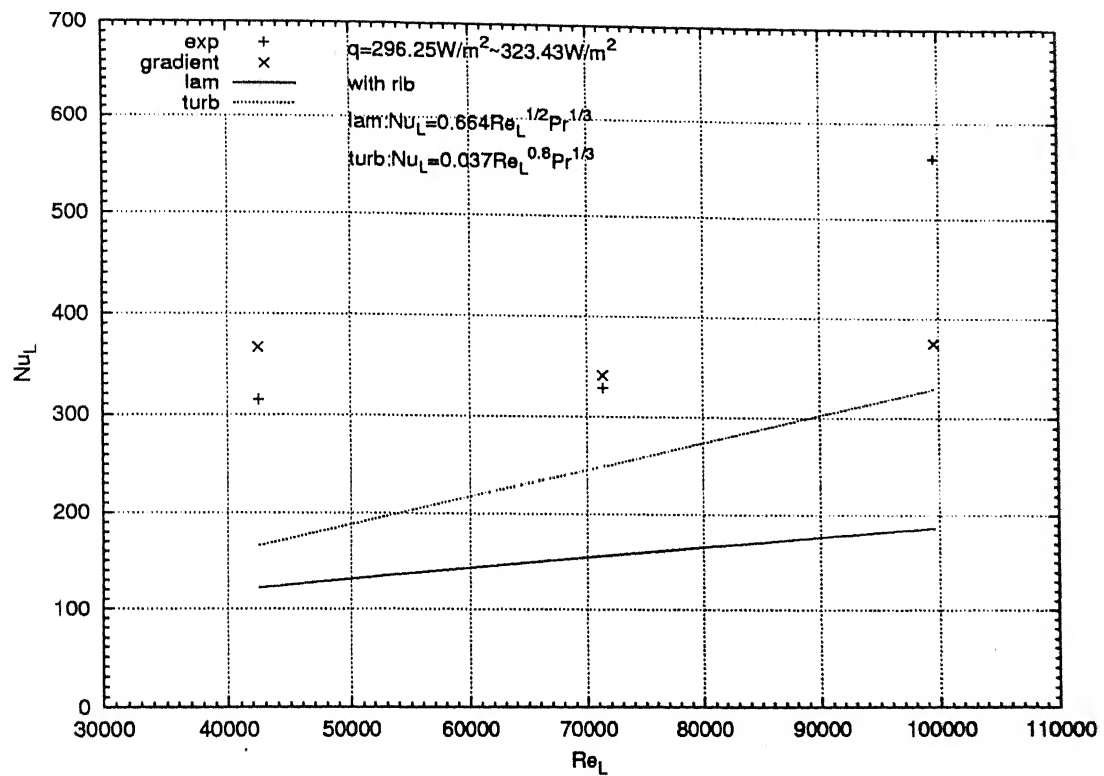


Figure 4.40: Average Nusselt number variation with Reynolds number for a flow over a flat surface with a rib

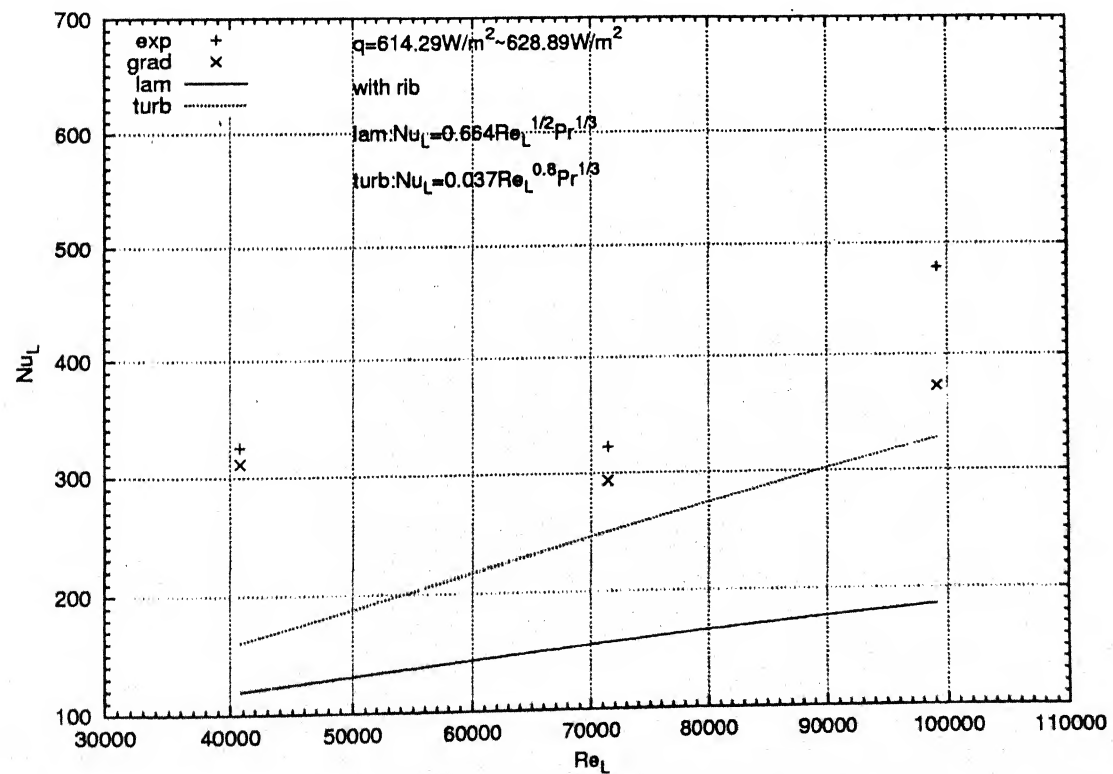


Figure 4.41: Average Nusselt number variation with Reynolds number for a flow over a flat surface with a rib

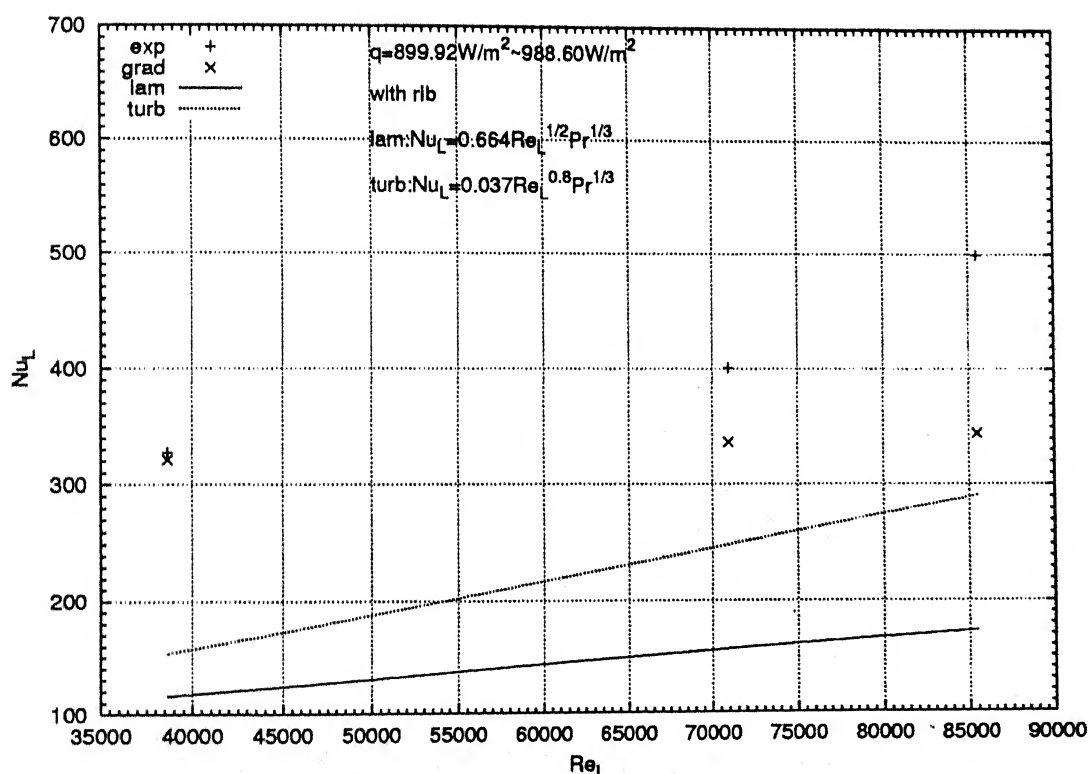


Figure 4.42: Average Nusselt number variation with Reynolds number for a flow over a flat surface with a rib

पुस्तकालय केन्द्र पुस्तकालय
भारतीय प्रौद्योगिकी संशोधन कानपुर
अवास्था क्र. 134278.....

the surface and free stream temperatures and by gradient method agree well with each other. The higher Nusselt numbers seen in the experiment are a clear indication of the heat transfer enhancement caused by the rib.

4.3 Comparison of Skin Friction coefficient with and without rib

Figures 4.43, 4.44 and 4.45 show the comparison of average skin friction coefficient from smooth channel measurement with measurement taken in a ribbed channel study. Except for a few scattered points, the dominant trend in skin friction coefficient is a reduction with an increase in Reynolds number. For the unribbed channel, the distribution of skin friction coefficient in this study coincides well with the theoretical laminar expression. At low Reynolds numbers, the skin friction coefficient of ribbed channel is considerable higher than that smooth channel but at a higher Reynolds number the skin friction coefficient of the ribbed channel comes closer to the smooth channel. This is because the rib affects the friction factor only for a short distance from the rib. The figures show that skin friction coefficient for the ribbed channel increases first and then decreases with increase of Reynolds number. This is due to the disturbance created by the rib which increases the skin friction coefficient first, but in the downstream, this effect is small.

4.4 Comparison Heat Transfer with and without the Rib

4.4.1 Local Nusselt Number

Figures 4.46, 4.47 and 4.48 show a comparison of the local Nusselt number for a smooth surface with a ribbed surface. The figures show that at low Reynolds number the local Nusselt number of ribbed channel is significantly higher than that of smooth channel. At a higher Reynolds number this difference is smaller. In all the three figures, the local Nusselt number of the ribbed channel increases

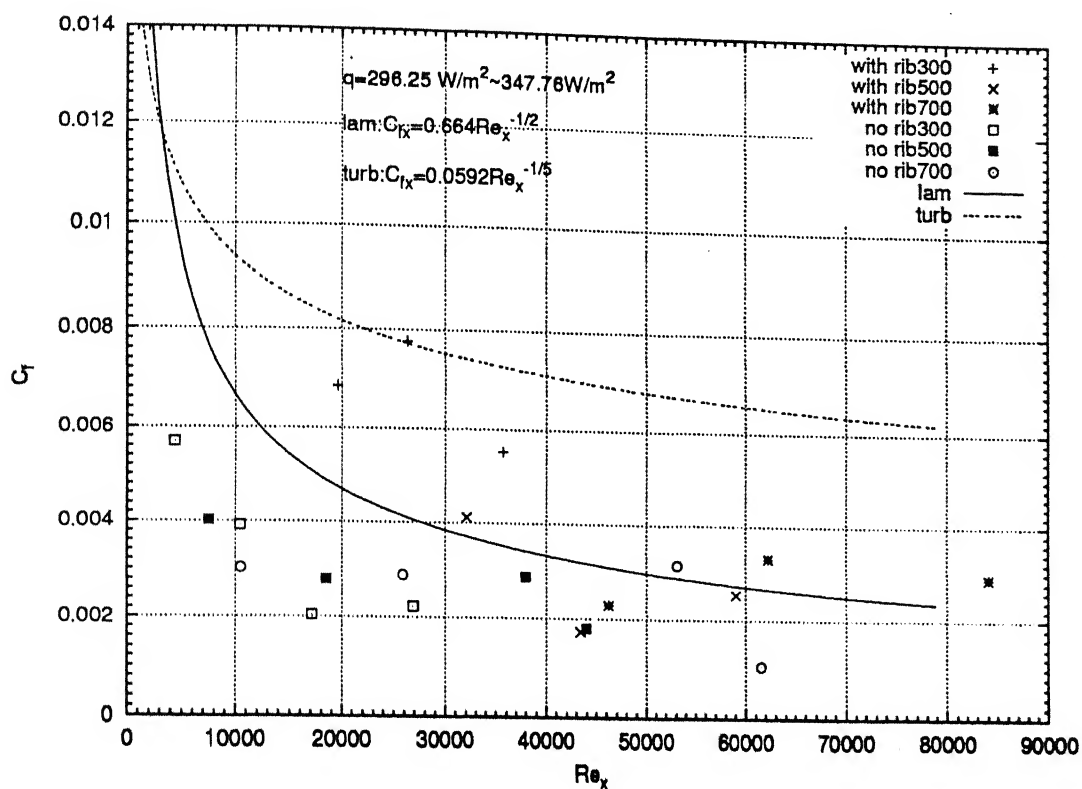


Figure 4.43: Comparison of skin friction coefficient for flow over a flat surface with and without a rib

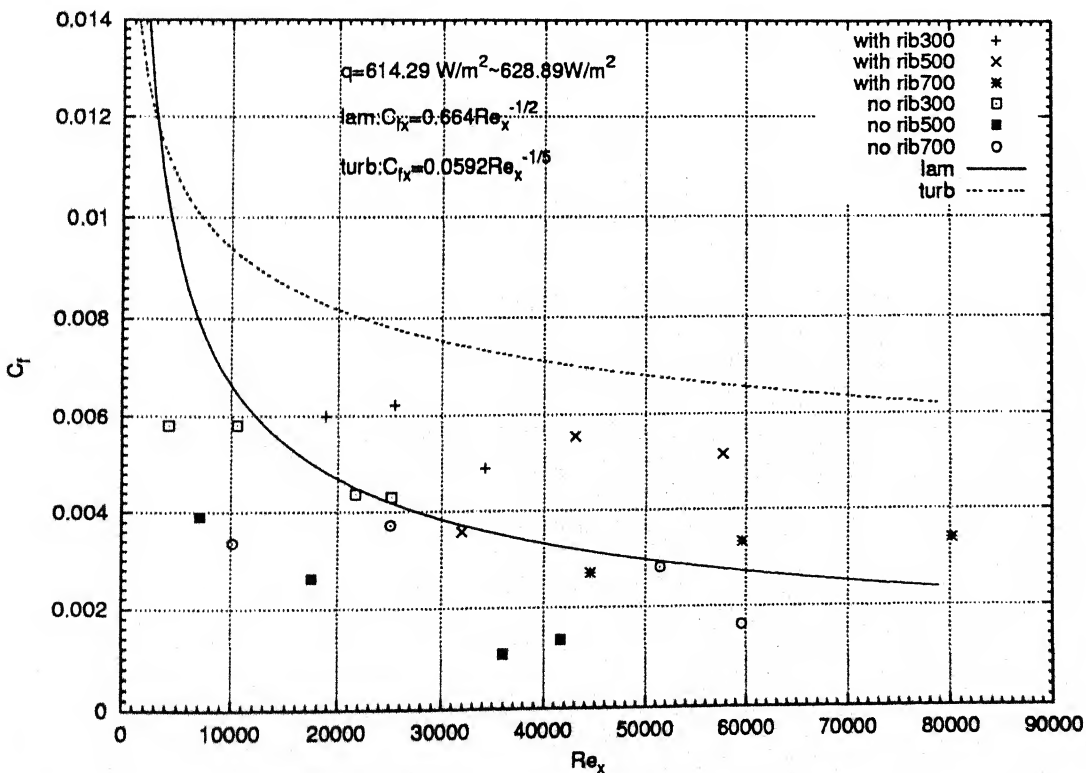


Figure 4.44: Comparison of skin friction coefficient for flow over a flat surface with and without a rib

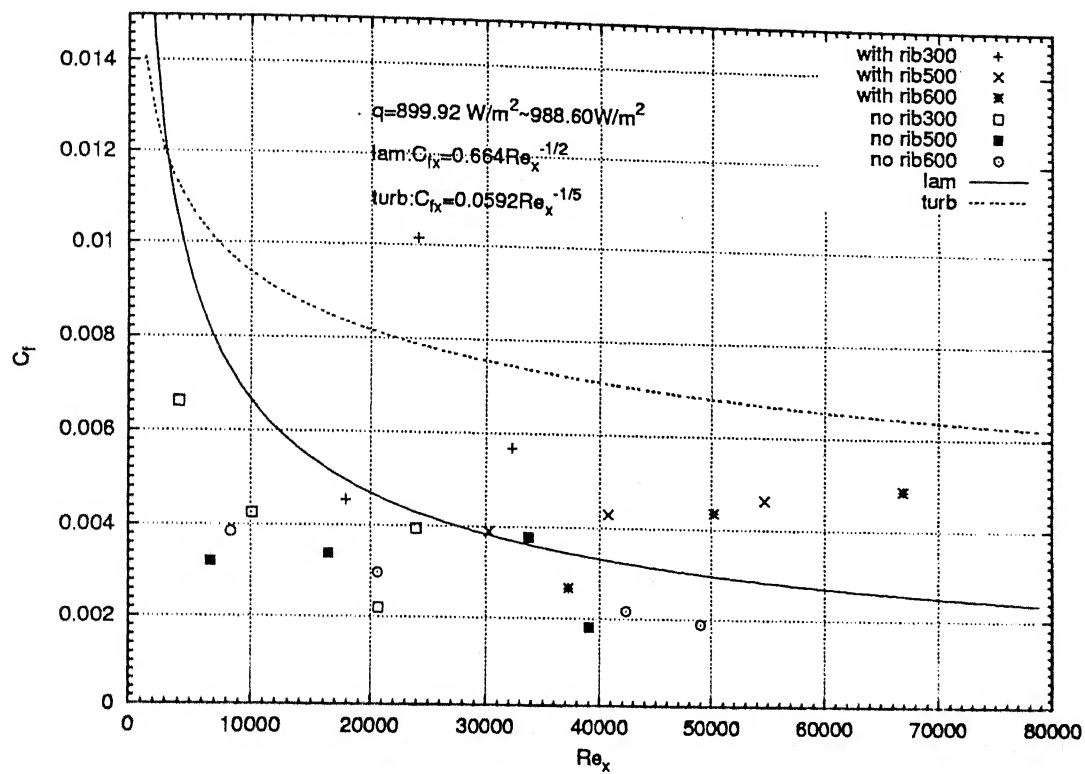


Figure 4.45: Comparison of skin friction coefficient for flow over a flat surface with and without a rib

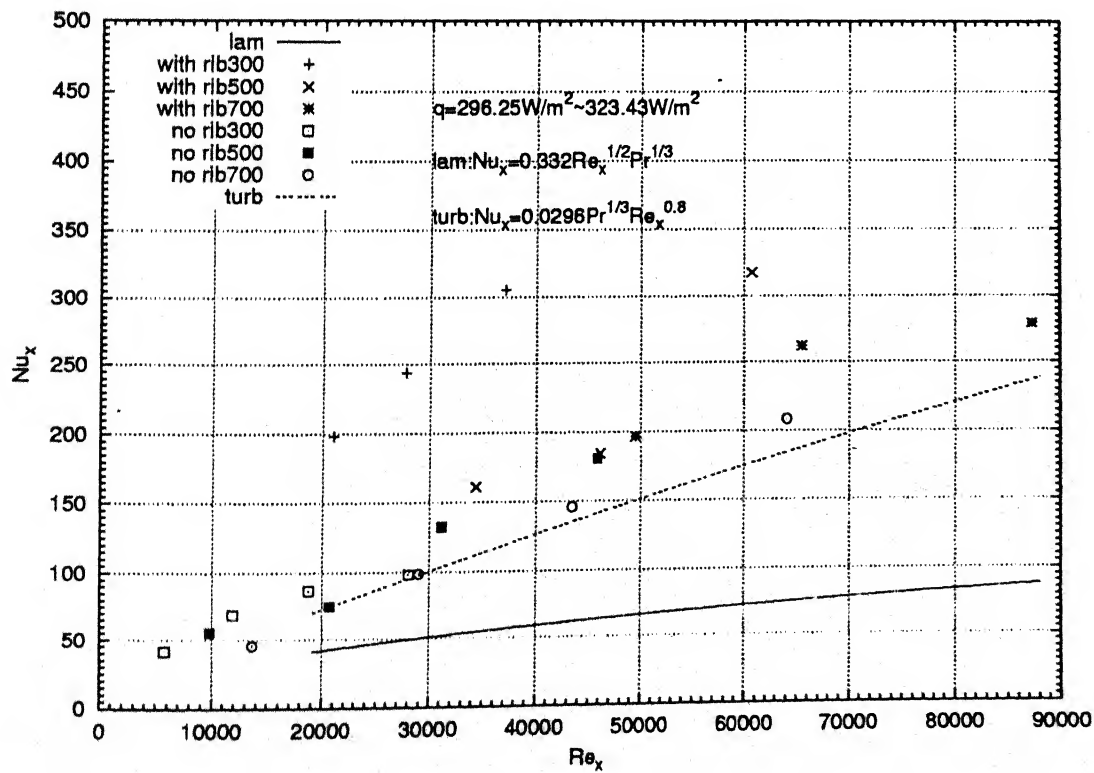


Figure 4.46: Comparison of local Nusselt number for flow over a flat surface with and without a rib

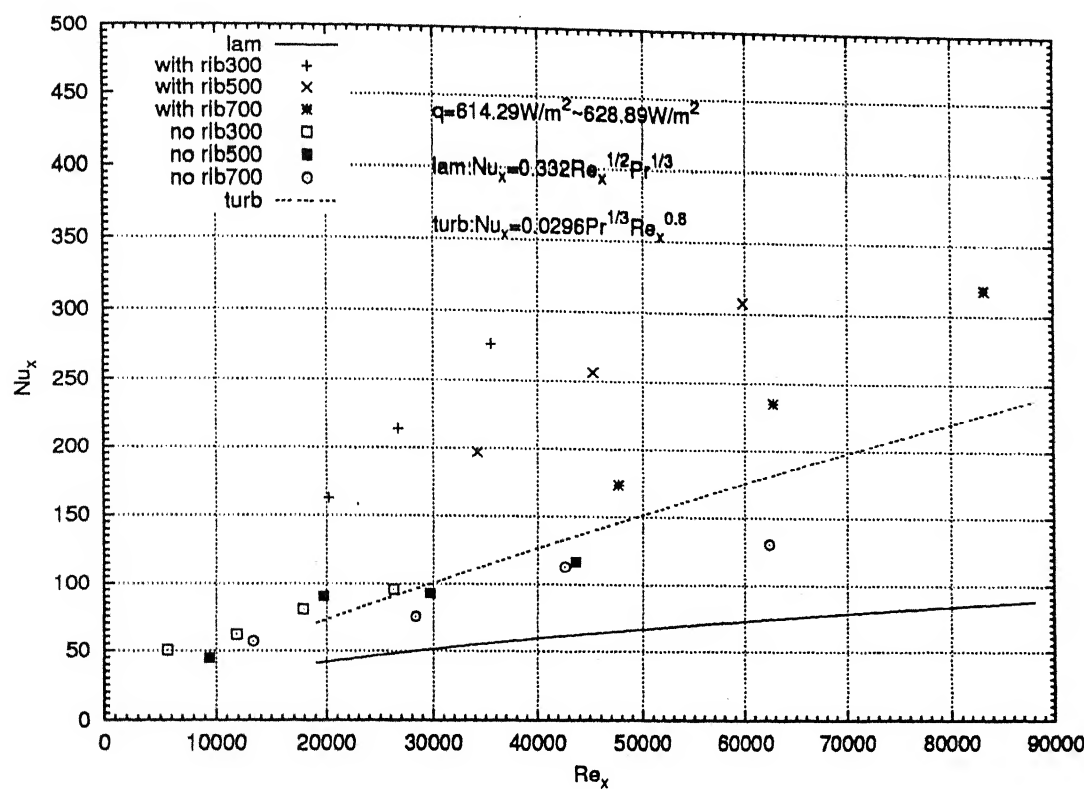


Figure 4.47: Comparison of local Nusselt number for flow over a flat surface with and without a rib

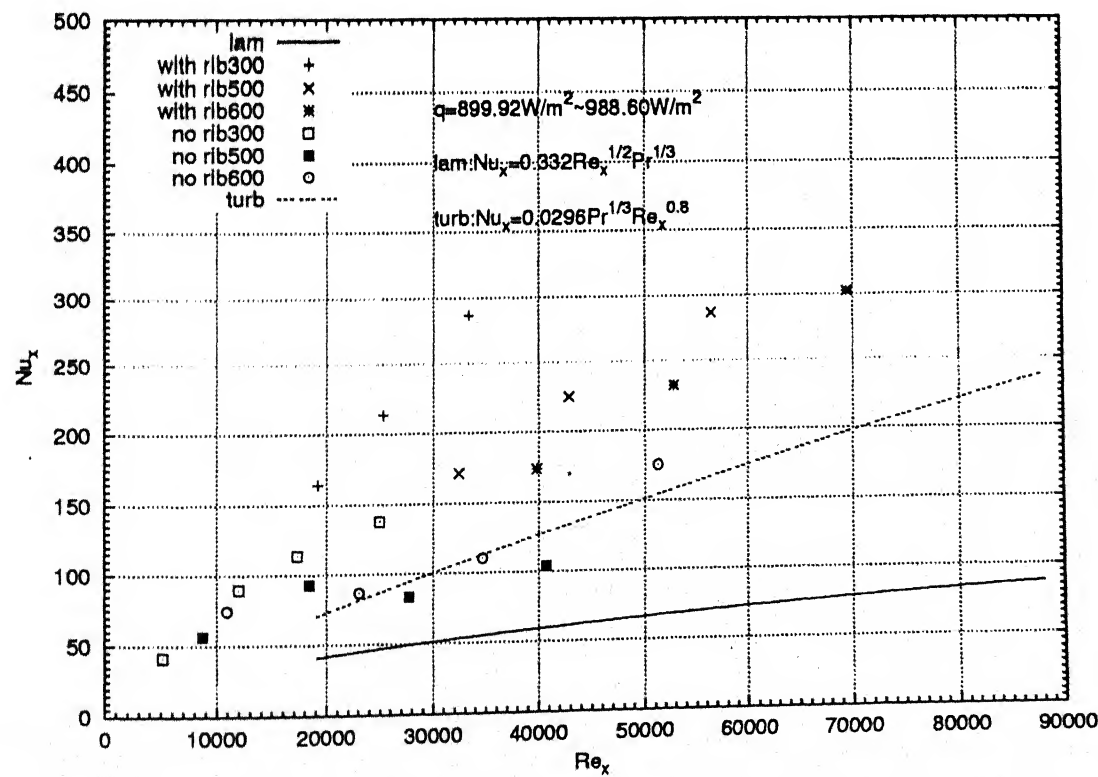


Figure 4.48: Comparison of local Nusselt number for flow over a flat surface with and without a rib

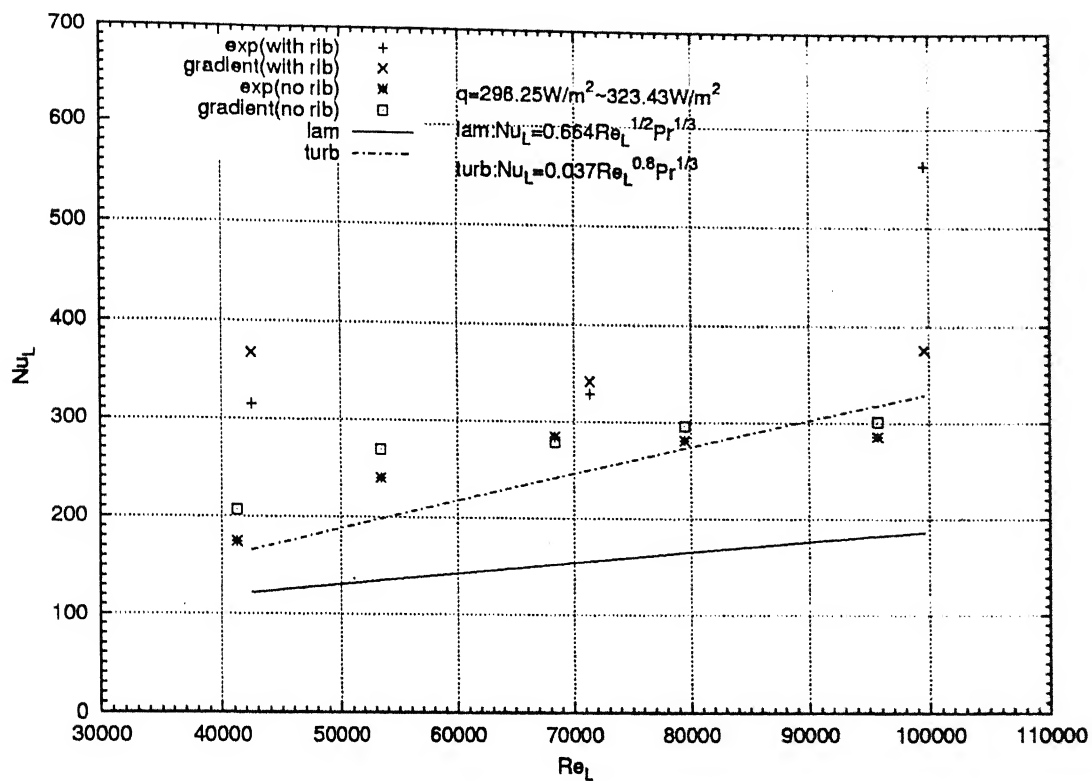


Figure 4.49: Comparison of Average Nusselt number for a flow over a flat surface with and without a rib

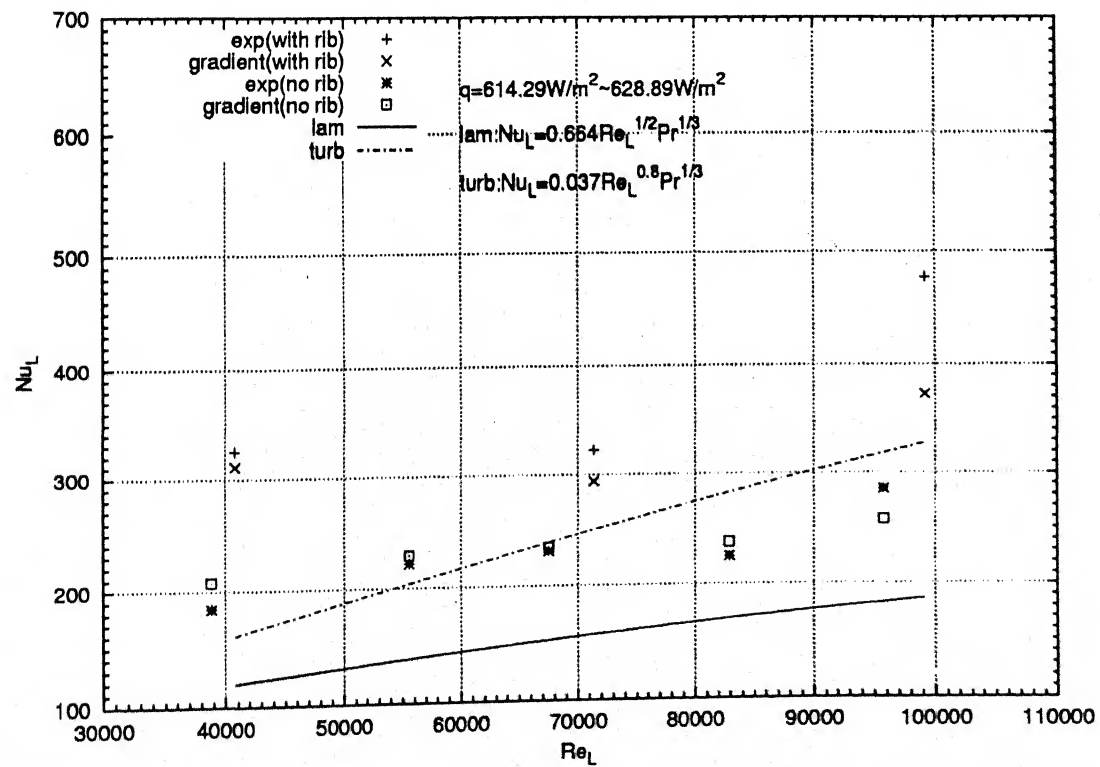


Figure 4.50: Comparison of Average Nusselt number for a flow over a flat surface with and without a rib

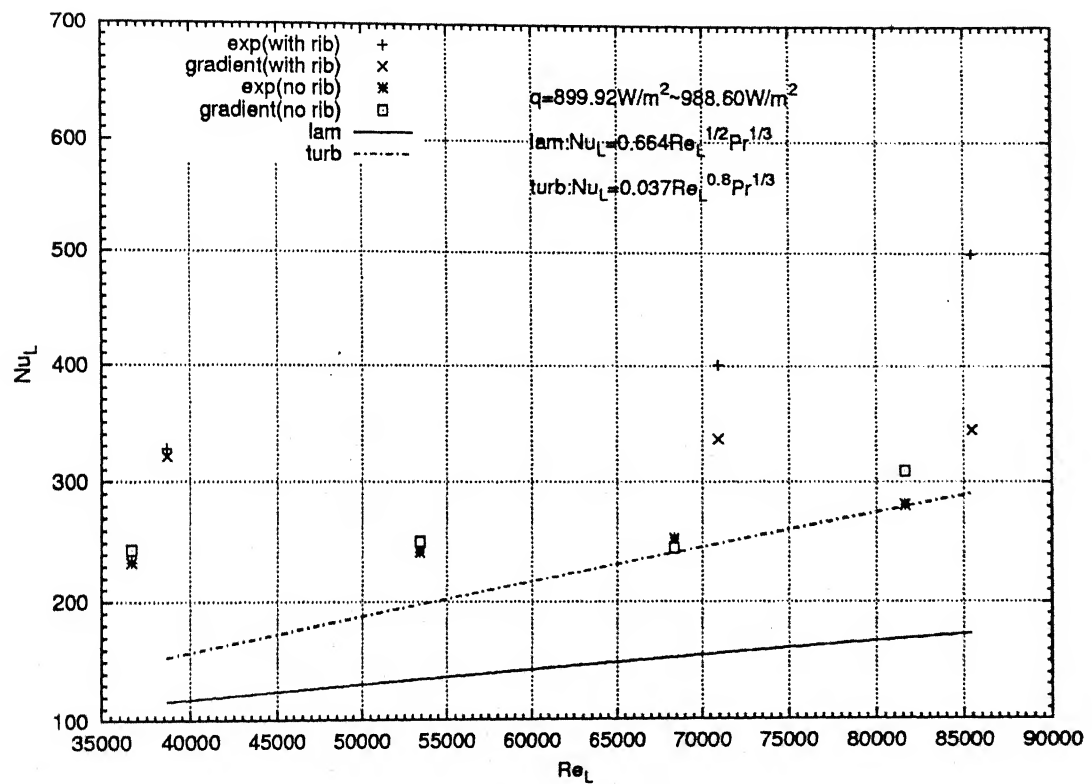


Figure 4.51: Comparison of Average Nusselt number for a flow over a flat surface with and without a rib

monotonically with an increase in the local Reynolds number. This is due to the disturbance created by the solid rib which enhances heat transfer downstream.

4.4.2 Average Heat Transfer Coefficient

Figures 4.49, 4.50 and 4.51 show a comparison of the average Nusselt number for smooth surface and ribbed surface. Both smooth and ribbed surfaces display an increase in Nusselt number with increasing Reynolds number. However, the rate of increase is slower for a ribbed surface than for smooth one. The figure clearly shows that the average Nusselt number for a ribbed surface is higher than that of a smooth surface. At low Reynolds numbers the average Nusselt number is very much higher than the smooth surface, but at higher Reynolds number this difference is smaller. For a smooth surface the average Nusselt number determined by both the energy method and the gradient method are in better agreement compared to the ribbed surface.

4.5 Visualization of surface temperatures using liquid crystals

The liquid crystal sheet produces a colour image in response to the temperature distribution. The colour values can be uniquely mapped into a hue-space. The calibration process establishes the relationship between the hue and the local temperature. The shape of the calibration curve is shown in Figure 4.52. It is well-defined in the range between 35°C to 42°C. Scattered readings can be seen in between 34°C to 35°C. A best curve was fitted through all the points and the analytical function was used for data reduction transient and steady state experiments. Figure 4.53 shows a relationship between the R, G, B and the local temperature.

4.5.1 Transient test experiment analysis

The colour images of the transient test experiment conducted at 300 rpm are shown in Figure 4.54. The corresponding temperature contours are shown in

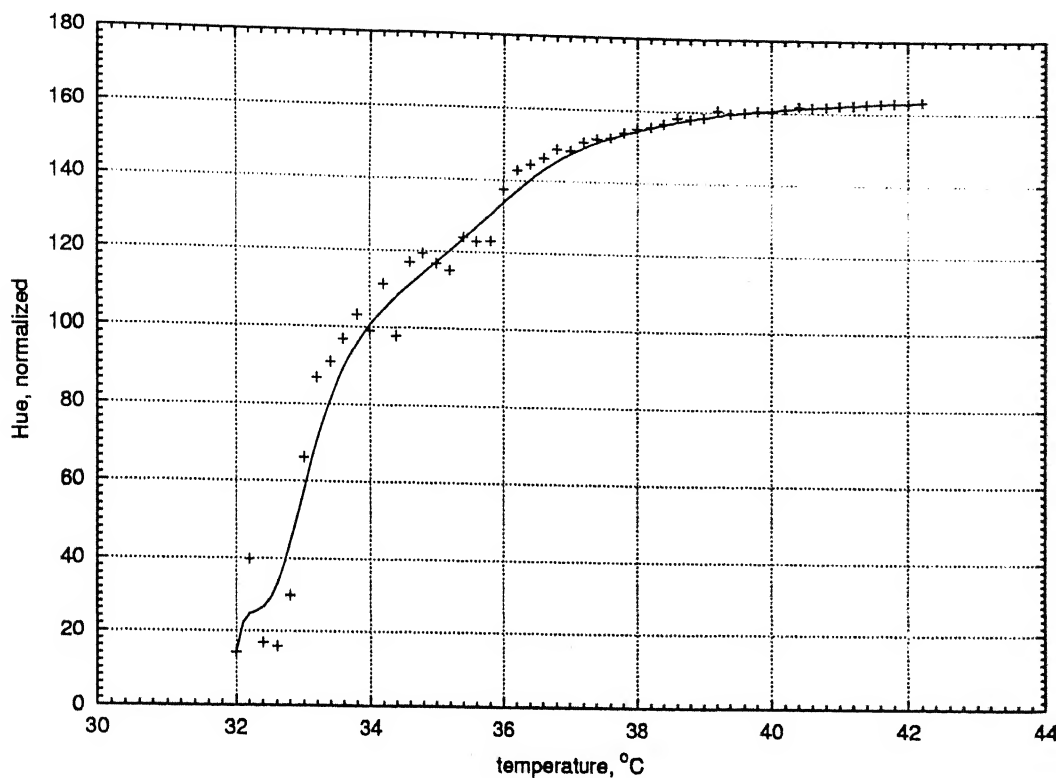


Figure 4.52: Calibration curve showing the relationship between the displayed hue and surface temperature.

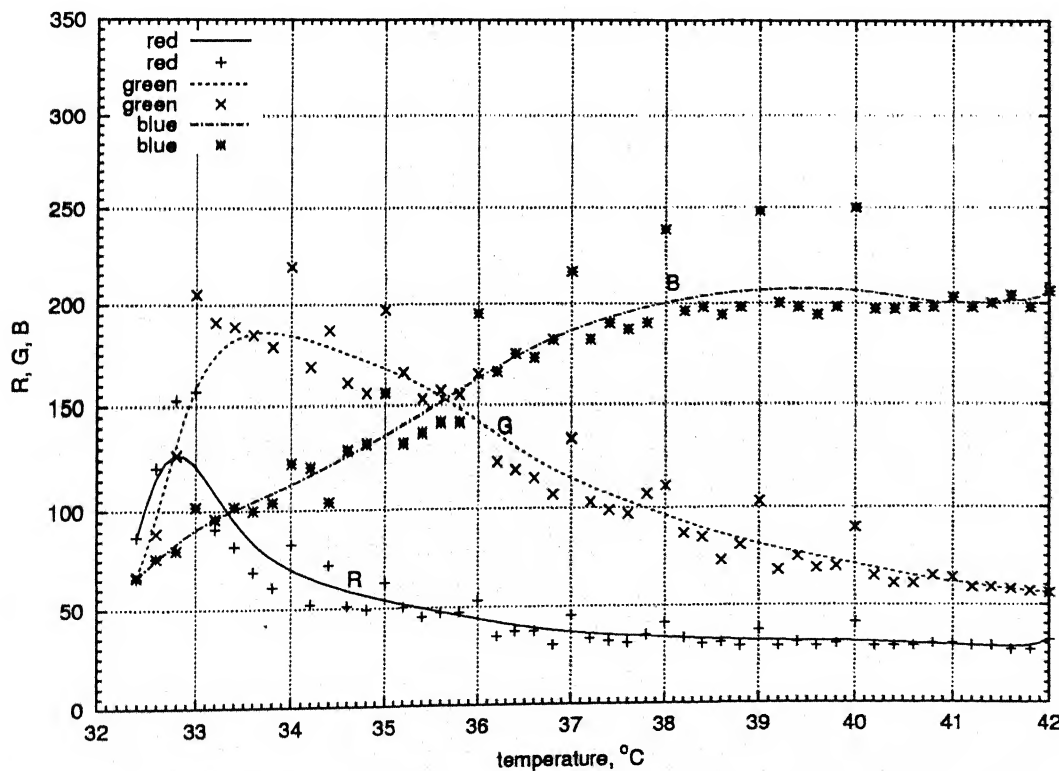


Figure 4.53: Calibration curve showing the relationship between the displayed R, G, B and surface temperature.

Figure 4.55. The initial plate temperature was 43°C . Figure 4.55(a) shows the temperature upstream of the rib to be in the range of 42.5°C to 43°C . The temperature downstream of the rib is in the range of 41.5°C to 42.5°C . Near to the rib the temperature is low due to fin effect. Figure 4.55(b) shows the temperature upstream of the rib to be in the range 40°C to 40.4°C . The temperature range beyond rib is in the range 39.6°C to 40.4°C . The temperature near the rib is 39.2°C . Figure 4.55(c) shows that the temperature is almost constant throughout the plate except that at some points, before the rib a slightly lower temperature . This is due to the small recirculating motion of the air ahead of the rib. Figure 4.55(d) also shows that the plate is at a constant temperature except at a few points before the rib. Figure 4.55(e) shows the temperature after the rib is almost constant at 34°C . The temperature before the rib is in the range of 34°C to 33.6°C . Figure 4.55(f) shows that there is 0.1°C temperature difference before and after the rib, the average temperature being rib 33.1°C . Thus, the plate has cooled to nearly constant temperature in 16 minutes.

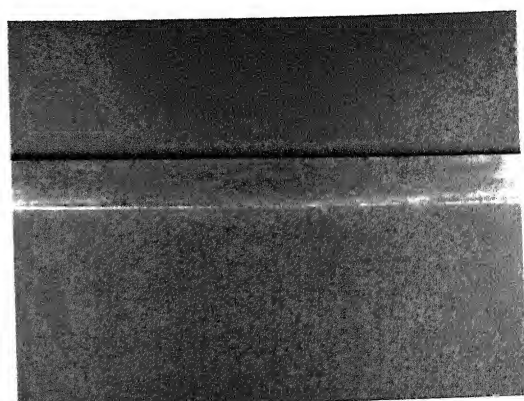
Similar colour images of transient test experiment at 500 rpm is shown in Figure 4.56. The corresponding temperature contours are shown in Figure 4.57. Since the fluid velocity is higher, the cooling rate is also higher and images are different from Figure 4.54. Figure 4.56(a) shows the first image of the experiment. Figure 4.57(a) shows the corresponding temperature contour. The temperature ahead of the rib is around 41.0°C . After the rib the temperature is about 40.5°C . Figure 4.56(b) shows the image after four minutes of cooling of the plate and Figure 4.56(b) show the temperature contour of that image. The temperature level before the rib is 37.6°C and after the rib is 37.5°C . Similarly Figure 4.56(c) and Figure 4.56(d) show the image after four and six minutes of cooling the plate respectively. Figures 4.57(c) and 4.57(d) show the corresponding temperature contours. Once again the temperature level after rib is less than that upstream of the rib. Figure 4.56(e) shows the image after eight minute of cooling of the plate. Figure 5.57(e) shows the corresponding temperature contours. It shows that the temperature after the rib is 32.7°C and temperature ahead of rib is in the range of 32.7°C to 32.75°C . Figure 4.56(f) shows the liquid crystal image after ten minute of cooling of the plate. Since the plate has cooled to a temperature less than 31°C , the thermal field is outside the range of liquid crystal and it becomes black.

4.5.2 Steady state Experiment

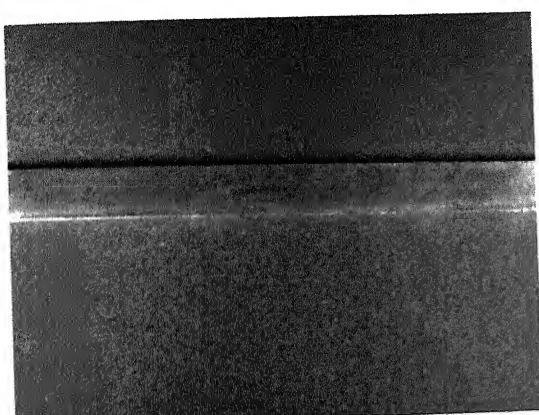
The steady state experiment has been performed with three different power levels namely 272 W/m^2 , 389.82 W/m^2 , 465.52 W/m^2 and one speed of the blower namely 500 rpm. The images were captured after the surface had reached steady state. Figure 4.58 shows the images of the liquid crystal sheet after attaining steady state. Figure 4.59 shows the temperature contour of the corresponding images. Figure 4.58(a) is the image recorded at a flux of 272 W/m^2 and 500 rpm after steady state. Figure 4.59(a) shows the temperature contour of this image. The temperature of the plate after the rib is in the range 33.1°C to 33.0°C and temperature ahead of the rib is 33.2°C . The temperature over many regions are constant throughout. Figure 4.58(b) is the image of the liquid crystal at a flux of 389.82 W/m^2 and 500 rpm. Figure 4.59(b) is the temperature contour of this image. The temperature of the plate ahead of the rib is 34.8°C and beyond rib it is in the range 34.6°C to 34.8°C . The temperature data is not as much scattered as in the transient test. Figure 4.58(c) is the image of the liquid crystal at a heat flux of 465.52 W/m^2 and 500 rpm. Figure 4.59(c) shows the temperature contours for this image. The contours show the temperature before and after the rib to be nearly constant. Some portions after the rib are at a slightly higher temperature, the difference being 0.2°C . Except for these minor differences, in all the three experiments the temperature distribution is almost uniform over the surface.



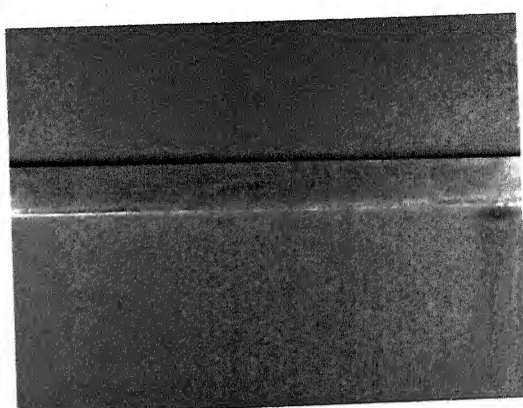
(a) 13:00 pm



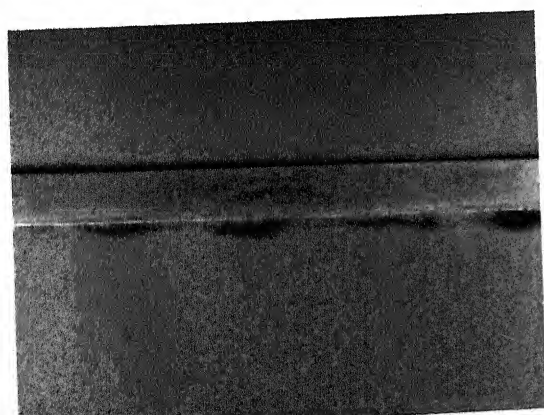
(b) 13:06 pm



(c) 13:10 pm



(d) 13:12 pm



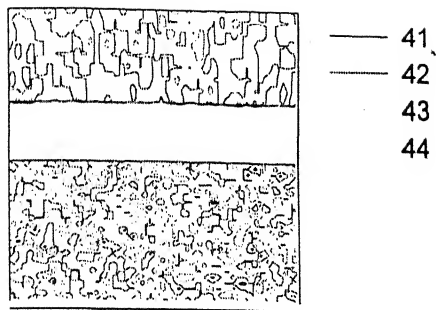
(e) 13:14 pm



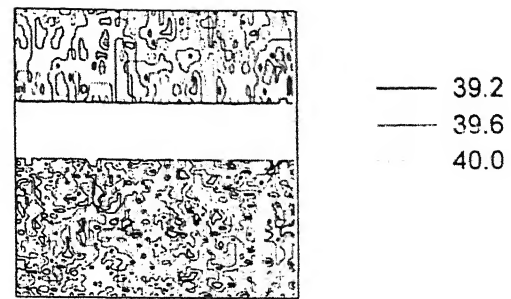
(f) 13:16 pm

Figure 4.54: LIQUID CRYSTAL IMAGES SHOWING THE COLOR CHANGES DURING COOLING OF PLATE AT 300 rpm IN THE UPSTREAM AND DOWNSTREAM OF RIB DURING THE TRANSIENT EXPERIMENT. FLOW DIRECTION IS FROM THE BOTTOM TO THE TOP.

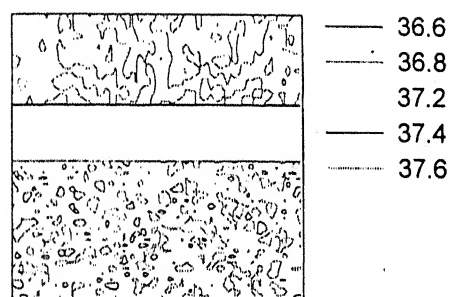
(a)



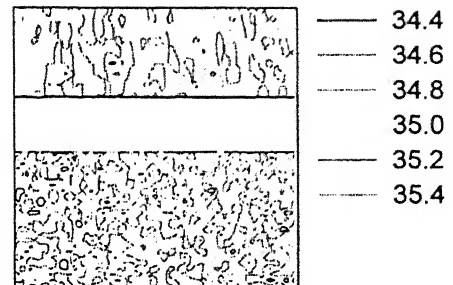
(b)



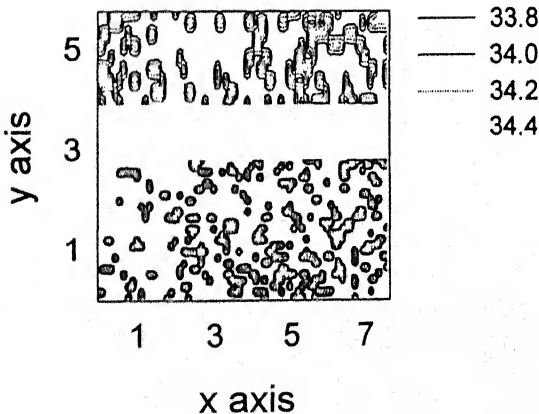
(c)



(d)



(e)



(f)

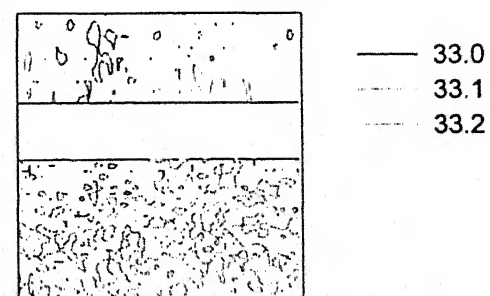
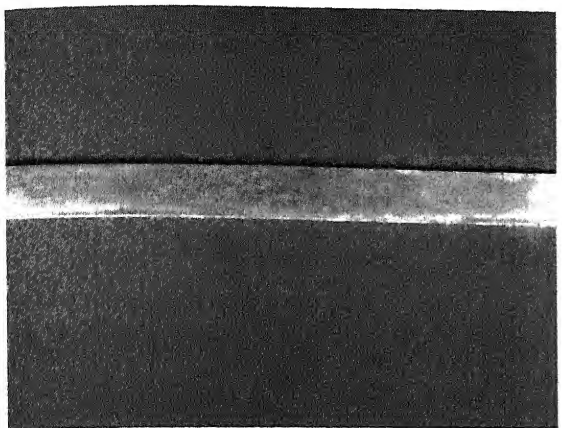
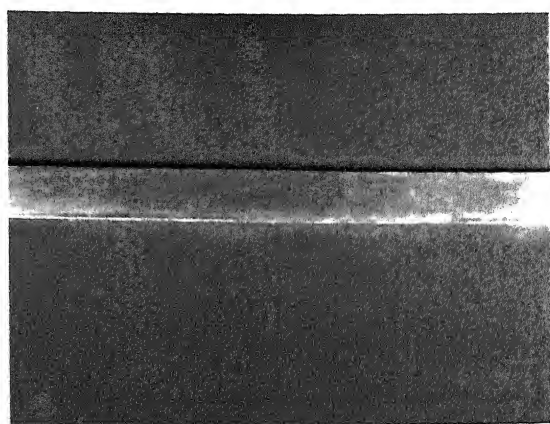


Figure 4.55: Transient temperature contours at 300rpm:

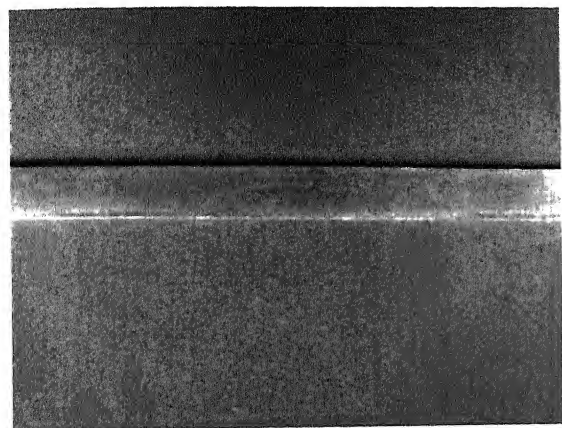
- (a) Initial, (b) After two minutes, (c) four minutes,
- (d) six minutes, (e) eight minutes, (f) ten minutes of cooling.



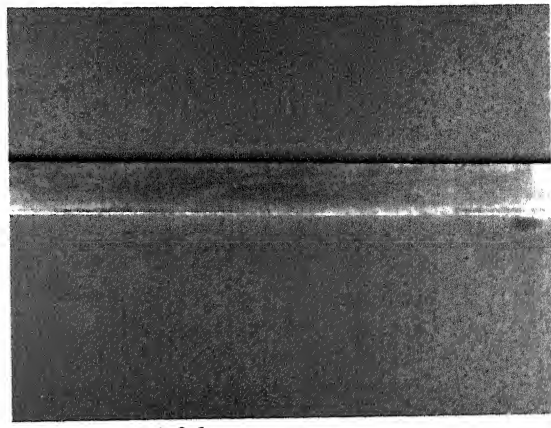
(a) 14:00 pm



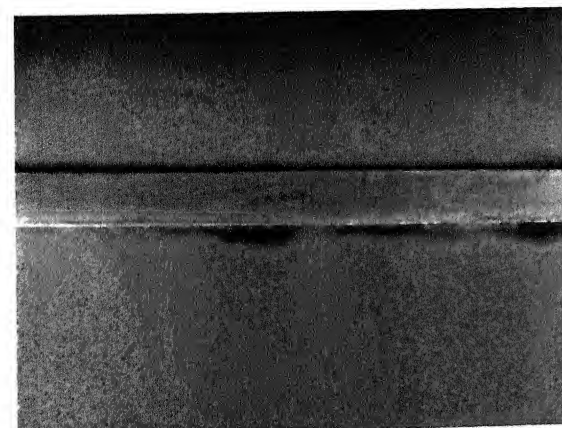
(b) 14:02 pm



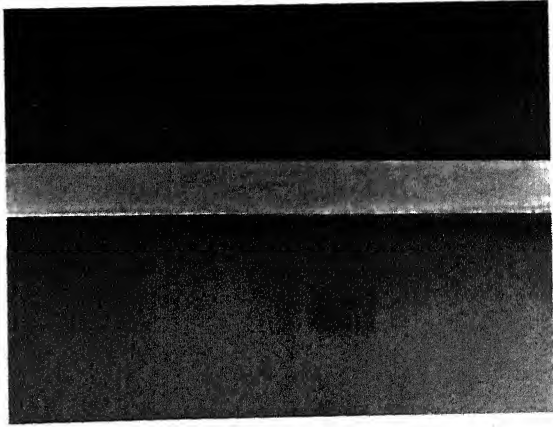
(c) 14:04 pm



(d) 14:06 pm



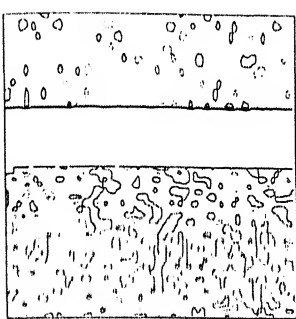
(e) 14:08 pm



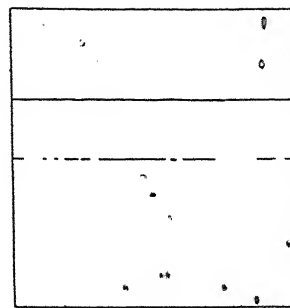
(f) 14:10 pm

Figure 4.56: LIQUID CRYSTAL IMAGES SHOWING THE COLOR CHANGES DURING COOLING OF PLATE FROM 41 °C AT 500 rpm IN THE UPSTREAM AND DOWNSTREAM OF RIB DURING THE TRANSIENT EXPERIMENT AT 2min INTERVALS. FLOW DIRECTION FROM THE BOTTOM TO THE TOP

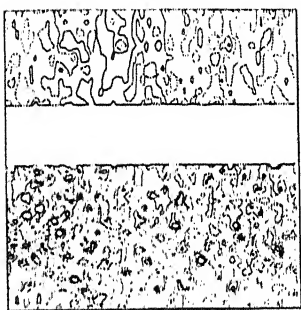
(a)



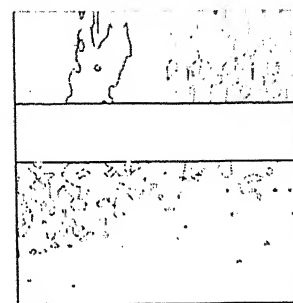
(b)



(c)



(d)



(e)

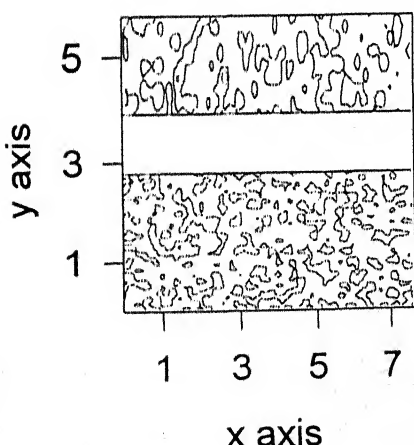
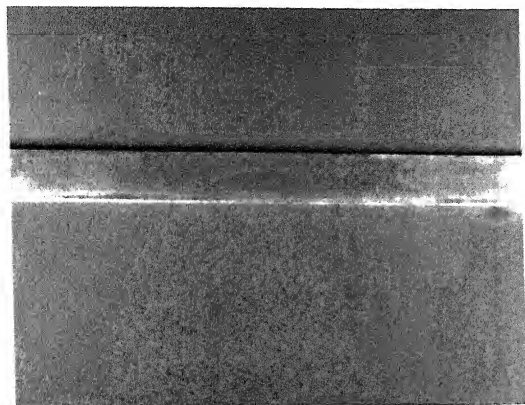
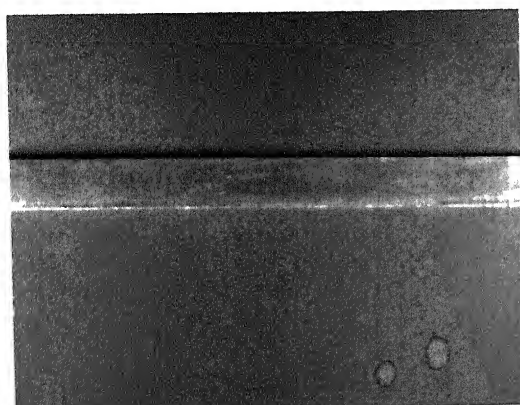


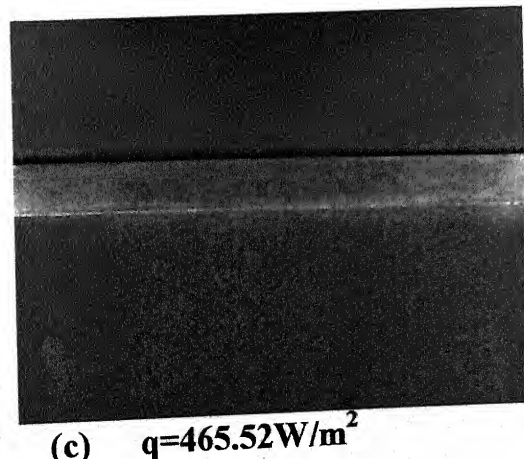
Figure 4.57: Transient temperature contours at 500rpm
 (a) Initial,
 (b) After six minutes, (c) eight minutes, (d) ten minutes,
 (e) twelve minutes of cooling



(a) $q=272\text{W/m}^2$



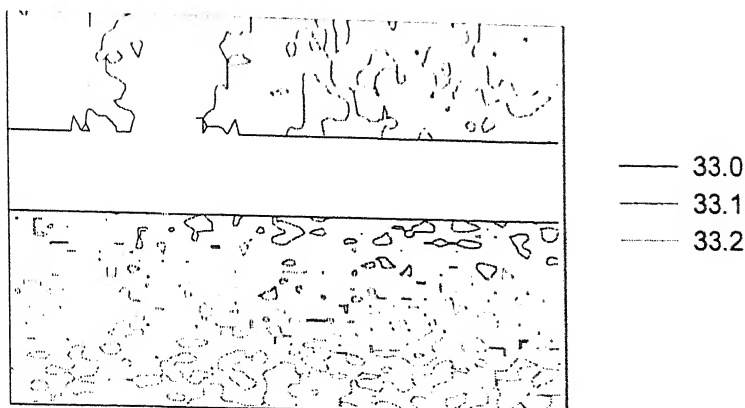
(b) $q=389.82\text{W/m}^2$



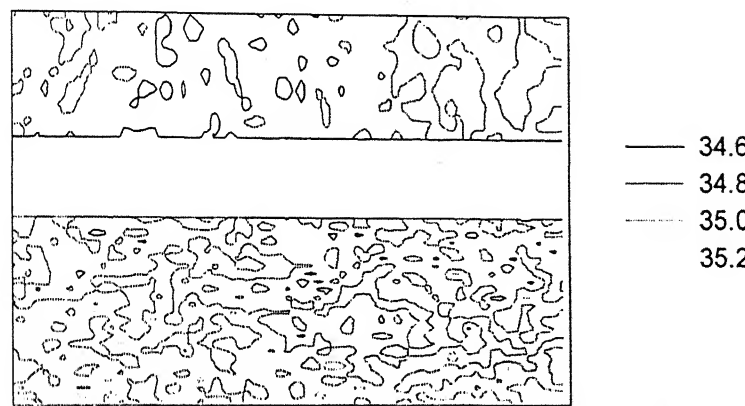
(c) $q=465.52\text{W/m}^2$

Figure 4.58:LIQUID CRYSTAL IMAGES SHOWING THE COLOR CHANGESAT DIFFERENT HEAT FLUX AT 500 rpm IN THE UPSTREAM AND DOWNSTREAM OF RIB. FLOW DIRECTION FROM THE BOTTOM TO THE TOP

(a)



(b)



(c)

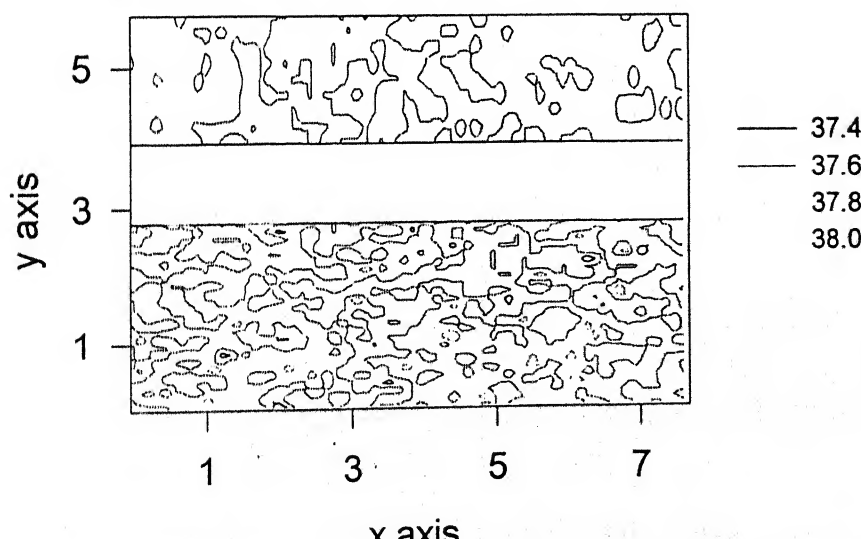


Figure 4.59: Steady state Temperature contours: (a) $q = 272 \text{ W/m}^2$ and $\text{rpm} = 500$
 (b) $q = 389.82 \text{ W/m}^2$ and $\text{rpm} = 500$, (c) $q = 465.52 \text{ W/m}^2$ and $\text{rpm} = 500$

Chapter 5

Conclusions and Scope for Future Work

5.1 Conclusions

Fluid flow and heat transfer characteristics of a flat surface and the influence a solid rib on it were investigated experimentally. The experiments were performed with different power inputs and Reynolds numbers in the range 10^3 - 10^5 . Liquid crystal thermography experiments have been performed to examine the changes of colour and hence the temperature distribution before and after the rib. The following conclusions have been drawn in the present work:

1. The flow was seen to be laminar for a smooth surface and turbulent for the ribbed surface over the range of Reynolds numbers studied. The heat transfer regime for both the smooth and the ribbed surfaces was turbulent. The reason for the heat transfer data of a smooth surface following the turbulent flow correlation could be the mild unsteadiness in the test cell arising from imperfections in the inflow section. These were perhaps averaged by the pitot static tube during velocity measurement, but the fluctuations led to a significant influence on heat transfer.
2. The local Nusselt number, average Nusselt number and skin friction coefficient for the ribbed surface were higher than that of a smooth surface.
3. The temperature distribution over the whole plate during transient state

test and steady state test were clearly brought out by the liquid crystals. The images showed up even minor temperature differences of 0.2°C and upto 3°C between various points of the plate. The temperatures after the rib were less than that of before the rib during the transient cooling phase of the plate. This can be explained in terms of the eddies formed by flow separation from the corners of the rib.

5.2 Scope for future work

1. Experimental study with different aspect ratios of the rib should be carried out to investigate heat transfer augmentation.
2. Experiments should be conducted with a higher range of Reynolds numbers to investigate effect of boundary layer turbulence on heat transfer enhancement.
3. Experimental study with a periodic rib array needs to be carried out to investigate the overall heat transfer enhancement.
4. In a solid rib a hot spot develops due to no flow condition just after the rib. To obviate the hot spot, the experiments should be carried out with perforated ribs.
5. Liquid crystal thermography can also be used to visualize the flow field.

Bibliography

- [1] Acharya, S., Dutta, S. Myrum, T.A. and Baker, R.S (1993) Periodically developed flow and heat transfer in a ribbed duct, *Int.J.Heat Mass Transfer*, 36, pp 2069-2082.
- [2] Boyle, R.J (1984) Heat transfer in serpentine passages with turbulence promoters, *ASME paper No. 84-HT-24*.
- [3] Burggraf, F. (1970) Experimental heat transfer and pressure drop with two dimensional turbulence promoters applied to two opposite wall of a square tube, *Augmentation of convective heat and mass transfer*, A.E Berbles and R.L webb, eds, ASME, pp 70-79.
- [4] Chandra, P.R., Han, J.C. and Lau, S.C (1988) Effect of rib angle on local heat/mass transfer in a two-pass rib-roughened channel, *ASME J Turbomachinery*, 110, pp 233-241.
- [5] Chyu, M.K (1991) Regional heat transfer in two-pass and three-pass passages with 180-deg sharp turns, *ASME J Heat Transfer*, 113, pp 63-70.
- [6] Ekkad, S.V. and Han, J.C (1997) detailed heat transfer distribution in two-pass square channels with rib turbulators, *Int.J.Heat Mass Transfer*, 40, pp 2525-2537.
- [7] Han, J.C (1984) Heat transfer and friction in channels with two opposite rib-roughened walls, *ASME J Heat Transfer*, 106, pp 774-781.
- [8] Han, J.C, Park, J.S and Lei, C.K. (1985) Heat Transfer enhancement in channels with turbulence promoters, *ASME J Engineering for Turbines and Power*, 107, pp 628-635.

- [9] Han, J.C. (1988) Heat transfer and friction characteristics in rectangular channels with rib turbulators, *Int.J.Heat Mass Transfer*, 110, pp 321-328.
- [10] Han, J.C., Zhang, Y.M. and Lee, C.P. (1991) Augmented heat transfer in square channels with parallel, crossed, and V-shaped angled ribs, *Int.J.Heat Mass Transfer*, 113, pp 590-596.
- [11] Holman, J.P (1997), Heat Transfer, McGraw-Hill, New York.
- [12] Hung, Y.H. and Lin, H.H. (1992) An effective installation of turbulence promoters for heat transfer augmentation in a vertical rib-heated channel, *Int.J.Heat Mass Transfer*, 35, pp 29-42.
- [13] Hwang, J.J. and Liou, T.M. (1994) Augmentation heat transfer in a rectangular with permeable ribs mounted on the wall, *Int.J.Heat Transfer*, 116, pp 912-920.
- [14] Hwang, J.J. and Liou, T.M. (1997) Heat transfer augmentation in a rectangular with slit rib turbulators on two opposite walls. *ASME J Turbomachinery*, 119, pp 617-623.
- [15] Hwang, J.J. (1998) Heat transfer and friction characteristics comparison in rectangular ducts with slit rib turbulators on one wall, *Int.J.Heat Transfer*, 120, pp 709-716.
- [16] Incropera, F.P., Dewitt, D.P. (1998), FUNDAMENTALS OF HEAT AND MASS TRANSFER, John Wiley and Sons.
- [17] Kays, W.M., Crawford, M.E. (1993), Convective Heat and Mass Transfer, McGraw-Hill, New York.
- [18] Kukreja, R.T. and Lau, S.C. (1998) Distributions of local heat transfer coefficient on surfaces with solid and perforated ribs, *J. Enhanced Heat Transfer*, 5/1, pp 9-21.
- [19] Mochizuki, S., Murata, A., Shibata, R. and Yang, W.J. (1999) Detailed measurement of local heat transfer coefficients in turbulent flow through smooth and rib-roughened serpentine passages with a 180° sharp end, *Int.J.Heat Mass Transfer*, 42, pp 1925-1934.

- [20] Schlichting, H.: "Boundary Layer Theory", 7th ed., McGraw-Hill Book company, New York, 1979.
- [21] Solntsev, V.P., Luzhanskii, B.E. and Kryukov, V.N. (1993a) An investigation of heat transfer in the turbulent separation zones in the vicinity of sudden steps, *Heat Transfer - Soviet Reaseach*, 5/2, pp 122-128.
- [22] Taslim, M.E., Li, T. and Kercher, D.M. (1996) Experimental heat transfer and friction in channels roughened with angled, V-shaped and discrete ribs on two opposite walls, *ASME J Turbomachinery*, 118, pp 20-28.
- [23] White, F.M., "Viscous Fluid Flow", McGraw-Hill Book company, New York, 1974.
- [24] Zhang, Y.M., Gu, W.Z. and Han, J.C (1994) Heat transfer and friction in a rectangular channels with ribbed-grooved walls, *ASME J Heat Transfer*, 116, pp 58-64.

Appendix A

Experimental Study of Natural Convection From Vertical and Horizontal Surfaces

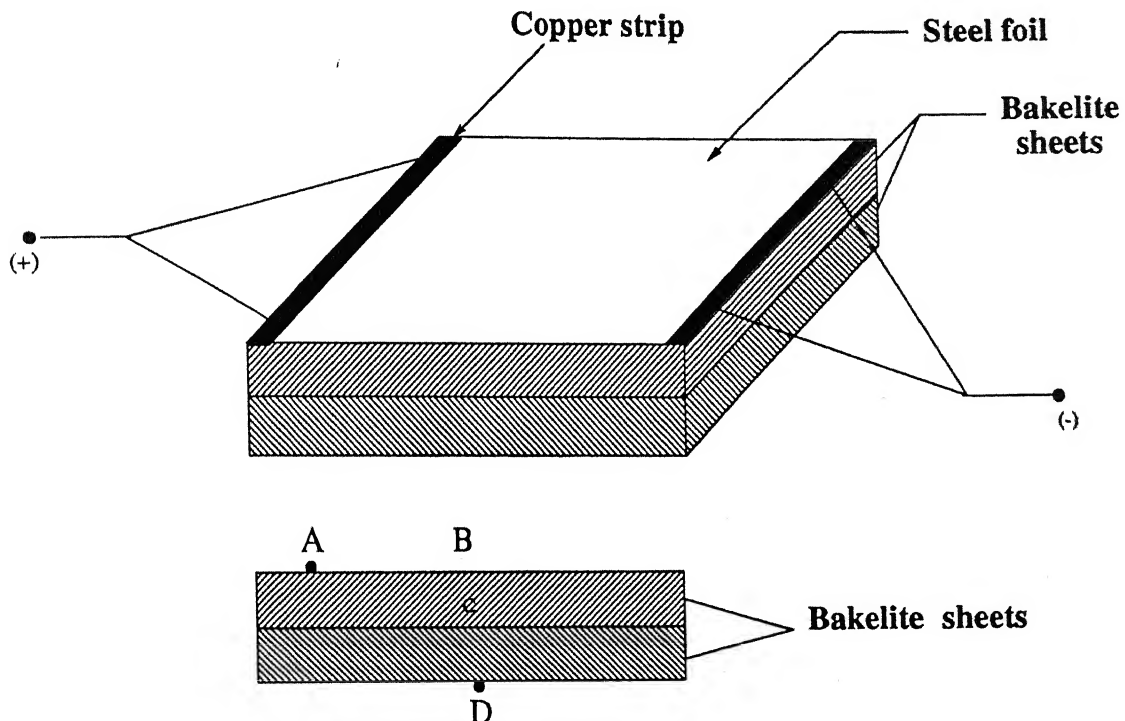
When a surface such as an aluminium plate is heated electrically using resistance strips, part of the thermal energy is transferred to the opposite side of the surface. The heated plate also losses energy by radiation. It is thus no longer correct to calculate the total convection heat transfer from the surface to the fluid as the electrical power input to the strip heater. Instead, one must calculate:

$$Q_{conv} = V \times I - Q_{cond} - Q_{rad}$$

The second and the third term on the right side are termed losses; they can be quite significant in experiments and must be estimated with care.

To gain experience with loss calculations, natural convection experiments were carried out with horizontal and vertical heated surfaces. The experimental arrangement is shown in Figure A.1. The design parameters of the apparatus used are summarized below:

Length of the Plate	=	0.087 m
Height or width of the Plate	=	0.06 m
Lower side area (A)	=	0.00522 m ²
Thickness of bakelite (t)	=	0.013 m
Conductivity of bakelite (k_b)	=	0.23 W/m. $^{\circ}$ C
Emissivity (ϵ) of stainless steel foil	=	0.1
Stefan-Boltzmann constant (σ)	=	5.67×10^{-8}



A, B, C and D are thermocouple positions

Figure A.1: Heating section in natural convection

The following experimental correlations have been used for comparison (Gebhart, B., 1988):

(a) Vertical Plate (Uniform wall temperature)

$$Nu^{\frac{1}{2}} = 0.825 + \frac{0.387 Ra^{\frac{1}{6}}}{(1 + (\frac{0.492}{Pr})^{\frac{9}{16}})^{\frac{8}{27}}} \quad (A.1)$$

where

$$\text{Rayleigh number } Ra = \frac{g\beta(T_w - T_\infty)H^3}{\nu^2} Pr$$

$$\text{Prandtl number } Pr = \frac{\mu C_p}{k}$$

all properties being evaluated at the average fluid temperature.
 A comparison between the experimental Nusselt number and the Nusselt number calculated from uniform wall temperature correlation for a vertical plate is shown in Table A.1.

Table A.1: Comparison between experimental Nusselt number and Nusselt number calculated from uniform wall temperature for vertical plate.

Table A.2: Comparison between experimental Nusselt number and Nusselt number calculated from uniform heat flux for vertical plate.

Voltage (Volt)	Current (Amp)	Temperature, °C				$V \times I$ (Watt)	Q_{cond} (Watt)	Q_{rad} (Watt)	Q_{net} (Watt)	h W/m ² .°C	Nu	Nu (Eq. A.2)
V	I	T_a	T_b	T_c	T_d	T_∞					Ra	Nu
0.168	6.8	37.7	35.8	31.5	28	22.3	1.2648	0.325	0.101	0.838	10.41	23.6
0.196	7.0	41	38.5	35.5	30	22.3	1.37	0.125	0.511	0.734	7.52	16.96
0.243	9.7	52	50	42	33.7	22.3	2.35	0.21	0.77	1.37	8.86	19.67

(b) Vertical Plate (Uniform heat flux)

$$\text{Nu}^{\frac{1}{2}} = 0.825 + \frac{0.387 \text{Ra}^{\frac{1}{6}}}{(1 + (\frac{0.437}{\text{Pr}})^{\frac{9}{16}})^{\frac{8}{27}}} \quad (\text{A.2})$$

where

$$\begin{aligned} \text{Modified Grashoff number } \text{Gr}^* &= \frac{g\beta q'' x^4}{k\nu^2} \\ \text{Grashoff number } \text{Gr} &= \frac{\text{Gr}^*}{\text{Nu}} \\ \text{Rayleigh number } \text{Ra} &= \text{Gr}^* \times \text{Ra} \end{aligned}$$

A comparison between the experimental Nusselt number and the Nusselt number calculated from uniform heat flux correlation for a vertical plate is shown in Table A.2.

(c) Horizontal Plate (Uniform wall temperature)

$$\text{Nu} = 0.54 \text{Ra}^{\frac{1}{4}} \quad (\text{A.3})$$

where

$$\begin{aligned} \text{Prandtl number } \text{Pr} &= \frac{\mu C_p}{k} \\ \text{Characteristic length } L &= \frac{A}{P} \\ \text{Grashoff number } \text{Gr} &= \frac{g\beta(T_a - T_\infty)L^3}{\nu^2} \\ \text{Rayleigh number } \text{Ra} &= \text{Gr} \times \text{Pr} \end{aligned}$$

A comparison between the experimental Nusselt number and the Nusselt number calculated from uniform wall temperature correlation for a horizontal plate is shown in Table A.3.

(d) Horizontal Plate (Uniform wall heat flux)

$$\text{Nu} = 0.13(\text{Ra})^{\frac{1}{3}} \quad (\text{A.4})$$

where, the properties of air are determined at $T_f = T_a - 0.25(T_a - T_\infty)$

$$\text{Rayleigh number } \text{Ra} = \frac{g\beta(T_a - T_\infty)L^3}{\nu^2} \text{Pr}$$

A comparison between the experimental Nusselt number and the Nusselt number calculated from uniform wall heat flux correlation for a horizontal plate is shown in Table A.4.

Table A.3: Comparison between experimental Nusselt number and Nusselt number calculated from uniform wall temperature for horizontal plate.

Voltage (Volt)	Current (Amp)	Temperature, °C						Q_{cond} (Watt)	Q_{rad} (Watt)	Q_{net} (Watt)	h W/m²°C	Nu	Nu (Eq. A.3)	
		V	I	T_a	T_b	T_c	T_d	T_∞						
0.215	8.92	47	52	39.8	30	21.5	1.9122	0.2151	0.9122	0.7849	4.96	3.2	13815	5.85
0.232	9.8	54.25	53	44.75	32.7	20	2.2736	0.2426	1.1216	0.9094	5.086	3.26	15427	6.01
0.243	10.01	54.25	54.25	44.75	32.7	20	2.432	0.2426	1.1216	1.0678	5.97	3.83	15427	6.01
0.296	12	70	65	52	37.3	21.5	3.55	0.374	1.368	1.808	7.14	4.43	19240	6.36
0.321	13.2	74	71	56.8	39.5	21.5	4.237	0.4129	1.61	2.214	8.07	4.97	20234	6.44

Table A.4: Comparison between experimental Nusselt number and Nusselt number calculated from uniform heat flux for horizontal plate.

A 134278

A 134278
Data Slip

Date Slip

The book is to be returned on
the date last stamped.



A134278